Exploring Nanoscale Surfaces and Interfaces

by

JAMES M. HELT

A dissertation submitted to the Graduate Faculty in Chemistry in partial fulfillment of the requirements for the degree of Doctor of Philosophy, The City University of New York

2005

UMI Number: 3287110

UMI Microform 3287110

Copyright 2008 by ProQuest Information and Learning Company.
All rights reserved. This microform edition is protected against
unauthorized copying under Title 17, United States Code.

ProQuest Information and Learning Company
300 North Zeeb Road
P.O. Box 1346
Ann Arbor, MI 48106-1346

This manuscript has been read and accepted for the Graduate Faculty in Chemistry in satisfaction of the dissertation requirement for the degree of Doctor of Philosophy.

7/18/2005
Date

Dr. James D. Batteas
Chair of Examining Committee

7/18/2005
Date

Dr. Gerald Koeppl
Executive Officer

Dr. Charles M. Drain

Dr. Bhanu P. S. Chauhan

Dr. George Flynn

Supervisory Committee

THE CITY UNIVERSITY OF NEW YORK

Abstract

EXPLORING NANOSCALE SURFACES AND INTERFACES

by

JAMES M. HELT

Adviser: Professor James D. Batteas

The atomic force microscope (AFM) offers a definitive approach for investigating the fundamental interactions of contacting surfaces in relative motion. AFM nanotribology investigations of muscovite mica wear under aqueous environments is discussed. Defect nucleation on the atomic scale has been directly observed and is found to present itself initially as surface charging due to stress-induced tribochemical bond scission as OH^- breaks open the terminal surface bonds. As surface bonds are continually cleaved, an ensemble of defects contribute to the observed native crystal lattice reconstruction from a 5.2 Å to ~3 Å periodicity. Following lattice restructuring, displacement of mica surface materials ensues, yielding wear scars ranging from ~ 2 - 10 Å in depth. This work is the first *in situ* demonstration of the tip-mediated tribochemical lattice reconstruction of mica with atomic scale resolution.

A new AFM experimental analysis methodology is also outlined that corrects for a common systematic error in AFM nanotribology studies and provides a more accurate account of an AFM tips scan history during wear trials. Comparison of the contact radius to the line step indicates that overlap of successive scans will result unless the *contact radius* - *line step* ratio (*CRLS*) is less than ½. If this relationship is not considered then the contact history associated with a single scan is not equivalent at different loads owing

to the scaling of contact radius with load. The *CRLS* model is derived and presented in conjunction with empirical wear tests on mica to evaluate the effects of scan overlap. *CRLS* predictions and empirical tests demonstrate that scan overlap pervades nanoscale wear trials even under low loads and can have deleterious effects on evaluating a materials nanotribological behavior.

Also discussed are two soft lithography techniques which use interfacial surface energetics to control and direct diffusive transport for nanofabrication purposes. First, a chemo-mechanical patterning method is introduced that exploits interfacial forces and local contact stresses for the facile production of nanoscale metal structures on polymers. Lastly, a rapid, reagent free soft lithography technique for the fabrication of self-aligned nanometer scale polymer-metal-polymer (PMP) multilayer structures on ceramic surfaces will also be described.

Thesis Overview

The area of nanotribology has advanced rapidly since the introduction of scanned probe microscopies (SPM) for surface characterization. The ability to probe the details of surface structure on an atomic/molecular scale affords a definitive approach for understanding surface contacts and the fundamental mechanisms of friction, adhesion and wear acting at such interfaces. This field has illustrated nontrivial deviations in the behavior of materials between nanoscale contacts and their mesoscale counterparts. Such developments are becoming ever more important as the contacting features in devices, e.g. microelectromechanical systems (MEMS), reach scales where local friction and adhesive forces can dictate the performance and viability of a device. The first chapter introduces some of SPM techniques employed to investigate the fundamental mechanisms of wear phenomena, as well as, an overview of the model substrate, muscovite mica.

In the second chapter, nanoscale atomic force microscopy (AFM) investigations of muscovite mica wear under aqueous environments will be discussed. Through concomitant acquisition of topography, friction and adhesion data under controlled pH conditions, defect nucleation on the atomic scale (*prior to gross wear*) may be directly observed. Nucleation is found to present itself initially as charging of the surface due to stress-induced tribochemical bond scission as OH^- breaks open the surface terminating Si-O-Si or Si-O-Al bonds. As the surface bonds are continually cleaved, an ensemble of defects (e.g. Si-OH/Al-OH and $Si\text{-}O^-$) contribute to a crystal lattice reconstruction (from ~5.2 Å to ~ 3 Å) as observed in AFM topographic and frictional force micrographs. Following lattice restructuring, displacement/abstraction of mica surface materials

ensues, yielding readily discernable wear scars ranging from ~ 2 - 10 Å in depth. This work is the first *in situ* demonstration of the direct, tip-mediated tribochemical lattice reconstruction of mica with atomic scale resolution, as well as, the first to explicitly follow the discrete progression from the nucleation to the nanoscale, gross wear regime. The solution studies found that the environmental OH^- concentration profoundly affects the efficacy of this sequence of events leading to wear and is illustrated by the *acceleration* or *inhibition* of wear with adjustment of pH under identical load and scan conditions.

Investigating the mechanism(s) of defect generation and growth on the nanometer length scales typically requires high resolution tools such as the atomic force microscope (AFM). In the third chapter, a new methodology is outlined that corrects for a common systematic error in AFM nanotribology studies and provides a more accurate account of an AFM tips scan history during wear trials. Generally, AFM wear trials are performed over an area defined by the length of the slow (L_{sscan}) and fast scan axes. The ratio of L_{sscan} to image resolution (*res*, lines per image) becomes an important experimental parameter in AFM wear trials as it defines the magnitude of the line step ($LS = L_{sscan}/res$), the distance the AFM tip steps along the slow scan axis. Comparing the contact radius (a) to the line step (LS) indicates that overlap of successive scans will result unless the *contact radius* - *line step* ratio (*CRLS*) is less than ½. If this relationship is not considered then the history, e.g. contact frequency, associated with a single scan is not equivalent at different loads owing to the scaling of contact radius with load ($a \propto F_z^{1/3}$). Here, we present a model in conjunction with empirical wear tests on muscovite mica to evaluate the effects of scan overlap. Using the Hertz contact mechanics definition of a, the *CRLS*

model shows that scan overlap pervades AFM wear trials even under low loads. Such findings indicate that the number of scans (N_{scans}) in an experiment underestimates the history conveyed to the surface by the tip, which therefore translates into an error in the recorded N_{scans}. AFM topography, frictional force (F_f) and force of adhesion (F_{adh}) measurements of native and worn mica under pH 5 conditions support this development. *CRLS* predictions are in excellent agreement with experiments in the mild wear regime, however, predictions are consistently underestimated for severe wear trials. The latter is to be expected since the inelastic contribution towards energy dissipation dominates the scan history within a wearing contact.

The studies on mica demonstrate that a mechanical stress coupled with a chemical catalyst can facilitate material degradation. In a similar way, Chapter 4 introduces a chemo-mechanical patterning method that exploits this type of behavior for the facile production of nanoscale metal structures on polymers. This approach allows for the design and patterning of a wide range of metallic structures on inexpensive polymer surfaces, affording the fabrication of nanoscaled platforms for use in the design of sensors, actuators, and disposable electronic and photonic devices. Numerous structures, from simple nanowires to multilayered metallic gratings, are demonstrated, with sizes ranging from microns to the nanoscale. The process involves molding a malleable metal film deposited on a rigid substrate such as mica, by the compression of a plastic polymer stamp with the desired pattern against the metal film. While under compression, an etchant is then used to modify the metal. Upon separation of the stamp from the support, micro- to nanoscaled metallic structures are found on the stamp and/or on the substrate. The sizes of the structures formed depend on the sizes of the features on the stamp but

can be fine-tuned by about 4-fold through variations in both pressure and duration of etching. Also, depending on the processing, multiple dimension metallic structures can be obtained simultaneously in a single stamping procedure. The metallic structures formed on the stamp can also be subsequently transferred to another surface allowing for the construction of multilayered materials such as band gap gratings or the application of electrical contacts. Using this approach, fabrication of both simple and complex micro- to nanoscaled structures can be accomplished by most any researcher as even the grating structure of commercial compact disks may be used as stamps, eliminating the requirement of expensive lithographic processes to form simple structures.

As in Chapter 4, Chapter 5 illustrates the use of surface energetics to control and direct diffusive transport for nanofabrication purposes. Here, a rapid soft lithography technique for the fabrication of micron to nanometer scale polymer-metal-polymer (PMP) multilayer structures on ceramic surfaces will be discussed. The technique exploits the high surface energy of metals to promote and direct the wetting of a thin, transferable metal layer by a thermoplastic polymer near the polymers glass transition (T_g) temperature. Disproportionate adhesion resulting from interfacial polymer diffusion and organization at the substrate-metal (*inter-layer* formation) and stamp-metal (*capping* layer formation) interfaces leads to transfer of the multilayer PMP structures to the substrate surface. Considering the thickness of the polymer *capping* ($1 = h = 50$ nm) and *inter-layer* ($4 = h = 11$ nm), it is anticipated that pattern transfer is enabled by finite size effects known to occur for ultra-thin polymer films. The versatility of the approach is further demonstrated with the ability to transfer PMP structures from *only* the *raised* stamp features (“single level” transfer), as well as, from *both* the *raised* and *recessed*

stamp features ("multi-level" transfer). Collectively, this method provides a simple benchtop route to numerous micro and nanoscale architectures on various substrates *without* the use of chemical reagents and therefore provides a economically and ecologically sound technique for nanoscale fabrication and integration.

This is

dedicated to my parents

Kathleen Helt and Donald Helt

"When a person has discovered the truth about something and has established it with great effort, then, on viewing his discoveries more carefully, he often realizes that what he has taken such pains to find might have been perceived with the greatest ease. For truth has the property that it is not so deeply concealed as many have thought…Yet it often happens that we do not see what is quite near at hand and clear. And we have a clear example of this right before us. For everything that was demonstrated and explained above so laboriously, is shown to us by Nature so openly and clearly that nothing could be plainer or more obvious."

Galileo, from *Galileo at Work: His Scientific Biography*, by Stillman Drake

Acknowledgements

This thesis is the culmination of research conducted under the direction of Dr. James Batteas, whom I began working under as an undergraduate researcher nearly 8 years ago. Without his guidance, expertise, fervor for the sport of science, and willingness to pursue and explore nature freely, this thesis would not have come to fruition. Thank you for the opportunity to be a part of these endeavors, all the support, advisement, and reassurance throughout this journey.

I would like to give special thanks to Dr. Charles Michael Drain for all his mentoring, patience, expertise and support. I could not have finished the final chapter without your faith in my “creations” and the open access to your research facilities. Thank you for keeping everything on track and in perspective during the seemingly endless last year.

I owe special thanks to my thesis committee members: Dr. James Batteas, Dr. Bhanu Chauhan, Dr. Charles Michael Drain and Dr. George Flynn of Columbia University. Without their expertise and annual review of my work, I would not have reached this point. Thank you for monitoring my progression and coming back after the first, very, very, very, long committee meeting…Thank you! ! !

There are a number of faculty members of the City University of New York who were integral to the completion of these studies. I would like to especially thank Dr. Daniel Akins for allowing me to be part of the IGERT program. Thank you for this great opportunity and the continued support that allowed me to fully focus on conducting and completing my Ph. D. work. I am indebted to Dr. William L’Amoreaux for his instruction on the scanning electron microscope and sputter coating system. Thank you

very much for giving me unparalleled access to this instrumentation. I could not have conducted or completed much of the work in this thesis (as well as undergraduate work) without your help. I wish to thank Dr. Bhanu Chauhan for allowing me to work in his group and providing me with lab space during my last year of study. I cannot thank you enough for giving me this workspace and am extremely grateful. I also wish to thank Dr. Ruth Stark and Dr. Chwen-Yang Shew for the effort that they put forth in reviewing and moderating my second level proposal. I would also like to thank Dr. Shew for his review and comments on the work in Chapter 3. Thank you for calming my nerves. I also would like to thank Dr. Nan-Loh Yang for the annual luncheon meetings and providing the good word that helped keep the spirit high when the occasional hurdles and setbacks arose. Keeping track of all the requirements that needed to be met along the way was greatly facilitated by Prof. Koeppl and Diane Adebowale. Thank you for your hard work.

I would also like to thank the following CUNY staff within the Chemistry department for their everyday assistance and efforts that kept everything moving along: James Saccardo, Soa Dang, Diane Paladino, Susan Chew, and Angela La Duca.

I also owe thanks to Dr. John Pojman of the University of Southern Mississippi for giving me the opportunity to be part of the Summer Undergraduate Research Program. This was an unbelievable experience and set the ball rolling for my pursuit of this degree. Thank you for introducing me to your work, your research group and a glimpse of all the good things chemistry has in store for us.

The continued love and support of my family and friends has truly enabled me to complete this expedition of curiosity and I thank you. I couldn’t have done this without Mom, Dad, Donny, Susy, Rachel, Colleen, Stacey, Grandma C., Grandma H. and

Grandpa. The expertise and workshop of my grandfather enabled the fabrication of many instruments and the “toaster oven” used in Chapter 5. This work would not have been possible otherwise and I send great thanks for all the lessons. Mike, thank you for all the refreshing discussions on science and nanotech at Starbucks. Doug and Joe, thank you for lending an ear for my woes and the good advice.

Lastly I would like to acknowledge support from National Science Foundation (IGERT DGE-9972892, and CHE-0135509); Research Corporation Research Innovation award (RI0072); the Israel-US Binational Science Foundation; American Chemical Society Petroleum Research Fund (34792-G5); and the PSC CUNY Research Awards Program (63335-0032, 64385-0033)

Table of Contents

List of Figures....xviii

List of Tables....xxii

List of Symbols and Definition of Terms....xxiii

Chapter 1 – Overview of Surfaces and Nanotribology

1.1 Introduction....1

1.2 Mica as a Model Substrate....2

1.3 Scanned Probe Methodologies....5

1.3.1 Atomic Force Microscopy: General Methodology....5

1.3.2 Contact Mode Topographic (Height) Measurements....6

1.3.3 Lateral Force (Friction and Shear) Measurements....7

1.4 Making Quantitative Measurements....8

1.4.1 Calibration of AFM Cantilevers....8

1.4.2 Probe Tip Characterization....10

1.4.3 Adhesion Measurements....12

1.4.4 What Is a Single AFM Scan?....14

1.5 Summary....16

Appendix 1.1 – Proximal Tip Shape Characterization....18

References....20

Chapter 2 – Atomic Scale Wear and Tip Mediated Defect Nucleation

2.1 Introduction....28

2.2 Experimental....31

2.3 Results and Discussion....34

2.4 Insights into the Atomic Scale Wear Behavior of Crystal Surface....47

2.5 Summary and Conclusions....50

Appendix 2.1 – Contact Radius and Pressure Calculation....52

References....53

Chapter 3 – Scanning Probe Nanotribology and the Contact Radius – Line Step Relationship

3.1 Introduction....57

3.2 Analysis Methodology....61

3.3 Experimental

3.3.1 CRLS Model Parameters....74

3.3.2 AFM Wear Studies Empirically Testing CRLS Analysis....74

3.4 Results and Discussion: Does Overlap Really Matter?

3.4.1 Modeling Overlap....77

3.4.2 Paired AFM Wear Studies....80

3.5 Summary and Conclusion....90

Appendix 3.1 – Derivation of Expressions for Scan Correction ($scan_{cor}$) Calculation....91

References....94

Chapter 4 – A Benchtop Method for the Fabrication and Patterning of Nanoscale Structures on Polymer

4.1 Introduction....97

4.2 Experimental....99

4.2.1 General Patterning Process..99

4.2.2 Fabrication of Polymer Stamps...100

4.2.3 Formation of Au Films...101

4.2.4 Evaluation of Load Dependencies on Pattern Formation.......................101

4.2.5 Micro-Nanostructure Characterization...102

4.3 Results and Discussion

4.3.1 The General Patterning Process..104

4.3.2 Patterning with Planar Stamps..105

4.3.3 Patterning with Saw-Tooth Stamp Structures.......................................111

4.3.4 Formation of Multilayered Structures...116

4.4 Summary...116

Appendix 4.1 – Radial Pressure Distribution for the Nonlinear Lens Compression Cell Geometry..118

References..120

Chapter 5 – Assembly of Ultra-Thin Polymer-Metal Multilayer Arrays

5.1 Introduction...124

5.2 T-STOMP General Fabrication Technique 126

5.3 What Enables Pattern Transfer?. 127

5.4 Exemplary Examples of T-STOMP Products...128

5.4.1 Imaging and Characterization..128

5.4.2 Polymer Stamp Fabrication..129

5.4.2.1 CD and DVD Stamps...129

5.4.2.2 Compression Molding Lexan® Polycarbonate Stamps...........129

5.4.3 Film Preparation and Patterning Procedure....130

5.4.4 Fabrication of Multi-layer Microstructures....131

5.4.5 Nanofabrication with CDs and DVDs....135

5.4.5.1 Single Level Transfer for PMP_I Fabrication....135

5.4.5.2 Multi-Level Transfer for PMP_{II} Fabrication....138

5.5 Summary and Conclusion....142

Appendix 5.1 – Pneumatic Press Specifications....143

References....145

List of Figures

Figure 1.1 Pictorial representation of the mica (001) cleavage plane........................3

Figure 1.2 Schematic of an atomic force microscope..6

Figure 1.3 Schematic of an acquired AFM friction loop..8

Figure 1.4 Schematic of an AFM force-distance spectroscopy measurement.........13

Figure A1.1 Characterization of a V-shaped Si_3N_4 cantilever...................................19

Figure 2.1 Pictorial representation and lattice resolved AFM topography image of the muscovite mica (001) basal plane..29

Figure 2.2 Plot of F_{adh} and W_{adh} versus pH for muscovite mica with a Si_3N_4 tip....33

Figure 2.3 Topographic and friction micrographs of mica's basal plane within the defect nucleation wear regime...35

Figure 2.4 Topographic, friction and W_{adh} measurements of mica's basal plane within the early stages of the defect nucleation wear regime................38

Figure 2.5 Topographic and friction micrographs of the tribochemical reconstruction of mica's basal plane from a 5.2Å to a ~ 3 Å lattice periodicity..39

Figure 2.6 Graphical representation of a proposed geometry of the 3 Å lattice periodicity observed during the tribochemical reconstruction of mica's (001) basal plane...41

Figure 2.7 Topography and frictional force images following the abstraction of the basal planes terminating SiO_3 and AlO_3 molecular fragments..............46

Figure 3.1 Pictorial representation, orthogonal to the (001) plane, illustrating the progressive deterioration of micas basal plane during tribochemical wear processes....59

Figure 3.2 Inverse relationship between and AFM images line step (*LS*) and image resolution (*res*) for several slow scan lengths (L_{sscan}) 62

Figure 3.3 Simulated AFM image scans depicting the cumulative pressure history resulting from the overlap of Hertz contacts under several loads....66

Figure 3.4 Geometry of overlapping contacts of radii a according to Hertz continuum mechanics....69

Figure 3.5 Definition of elements used in evaluating $scan_{cor}$ for overlap of sequential line traces....72

Figure 3.6 Projected slow scan length, L_{sscan}^{CRLS}, required to avoid line scan overlap for a silicon tip (R = 30nm) and a mica substrate....76

Figure 3.7 Projected truncating parameter n_i for the silicon-mica material pair....76

Figure 3.8 Numerical results for $scan_{cor}$ for a silicon-mica material pair for a range of applied loads (F_z) 79

Figure 3.9 Proposed general form of the overlap correction curve for all tip-substrate material combinations....79

Figure 3.10 AFM analysis of a wear trial (defect nucleation regime) *with* scan overlap. Trial is paired with experiment conducted in Figure 3.11....81

Figure 3.11 AFM analysis of a wear trial (defect nucleation regime) *without* scan overlap. Trial is paired with experiment conducted in Figure 3.10....83

Figure 3.12 AFM analysis of a wear trial (gross wear regime) *with* scan overlap. Trial is paired with experiment conducted in Figure 3.13......................85

Figure 3.13 AFM analysis of a wear trial (gross wear regime) *without* scan overlap. Trial is paired with experiment conducted in Figure 3.12......................87

Figure A.3.1 Graphical forms of eqs. (A3.4, A3.7 and A3.11) after first integration of eq. A3.1..93

Figure 4.1 Schematic of the (chemical) STOMP protocol for micro-nanostructure fabrication 102

Figure 4.2 Schematic and AFM topography image of plastic deformation of a Au film during compression with a polymer stamp..................................103

Figure 4.3 Schematic and SEM images illustrating the placement of the primary structures formed with a rectangular profile polymer stamp................106

Figure 4.4 Gold microstructure patterns formed using polymer stamps with cylindrical pillar and square cross-hatch structures.............................108

Figure 4.5 Schematic and SEM images illustrating the placement of the primary structures formed with a saw-tooth profile polymer stamp.................110

Figure 4.6 Schematic of the nonlinear compression configuration used to generate a radial pressure distribution during STOMP processing.......................112

Figure 4.7 SEM images of a polystyrene stamp with gold wires, whose widths vary radially from the contact center, on the polymer stamp ridges............114

Figure 4.8 Schematic and SEM images illustrating cold-welding transfer of embedded Au wires for generating multilayer architectures...............115

Figure A4.1 Estimated radial pressure distribution for the non-linear, lens compression cell configuration....119

Figure 5.1 Schematic of T-STOMP processing with a bi-level, planar polymer stamp coated with a thin Au film....125

Figure 5.2 Schematic depicting the diffusion path of polymer stamp materials into the gold-film-substrate during T-STOMP processing....127

Figure 5.3 Graph of a typical temperature program used during T-STOMP processing....130

Figure 5.4 PMP_I tri-layer (PC/Au/PC) microstructures fabricated on mica using a compression molded Lexan® PC stamp coated with 10nm of Au....132

Figure 5.5 PMP_I tri-layer (PC/Au/PC) microstructures fabricated on mica using a bi-level polycarbonate compact disc (CD) stamp coated with 15 nm of Au....136

Figure 5.6 Various PMP_I tri-layer (PC/Au/PC) microstructures fabricated on mica using Au coated CD stamps....137

Figure 5.7 AFM topography images of PMP_{II} "multi-level" structures fabricated on mica using a DVD stamp coated with 15nm of Au....139

Figure 5.8 Images at the center of a PMP_{II} array fabricated on mica using a DVD PC stamp coated with 15nm of Au....141

Figure A5.1 The custom pneumatic press used for the thermal synthesis and transfer of materials to and from polymers (T-STOMP)....144

List of Tables

Table 2.1 Tribochemical properties of micas (001) crystal plane in solution...........34

Table 2.2 Threshold pressures for mica wear under solution conditions, and *ab initio* calculated activation energies (E_a) for various catalytic hydrolysis pathways 45

Table 2.3 Tribological properties of mica and halide crystals within defect nucleation regime...49

Table A3.1 Parameters and results from line scan overlap calculations.......................93

Table 4.1 Surface energies of the film, polymers and substrates employed in STOMP processing..105

Table A5.1 Specifications for Heated Pneumatic Press...143

List of Symbols and Definition of Terms

α	limit of integration for $scan_{cor}$ calculation
α	hydrophobic microchannel (only Chapter 4)
β	limit of integration for $scan_{cor}$ calculation
β	hydrophilic microchannel (only Chapter 4)
χ	limit of integration for $scan_{cor}$ calculation
a	Hertz contact radius
CRLS	contact radius-line step analysis
Δ_y	center-to-center distance along the slow scan axis for successive line traces as referenced to the first scan line ($n_0 = 0$)
E	Young's modulus
ε	Reduced Young's elastic modulus
E_a	activation energy
$f(x)$	second order polynomial (primes indicate first and second derivatives)
F_{adh}	force of adhesion
F_z	normal force
F_{ovlp}	normal force within a region of overlap
F_f	force of friction
γ	interfacial tension or surface energy
h	film thickness/height
k_{lever}	cantilevers lateral (torsional) force constant
$k_{contact}$	lateral contact stiffness
k_{total}	combined lateral stiffness of the cantilever and contact

k_{lever}^{normal} normal cantilever stiffness (spring constant)

K circle of curvature; tangent vector rate of change to the arc length rate of change

L length of a rectangular cantilever

LS line step; equal to the pitch of successive line traces along the slow scan axis

L_{sscan} length of the AFM slow scan axis

L_{sscan}^{CRLS} length of the AFM slow scan axis in the absence of line scan overlap

M_w weight average molecular mass

m_i shifted scan overlap truncating parameter ($m_i = n_i$ -1)

n_i scan overlap truncating parameter

v Poisson ratio

N_{scans}^{Exp} experimental number of AFM image scans

$N_{scans}^{correct}$ experimental number of AFM image scans corrected for line scan overlap

p_m Hertz mean tip-sample contact pressure

p_{max} Hertz maximum tip-sample contact pressure

$p^{history}$ cumulative (additive) pressure history due to line scan overlap

$p_{max}^{history}$ maximum cumulative (additive) pressure history attributed to line scan overlap

PMP T-STOMP fabricated polymer-metal-polymer multi-layer heterostructures

p_{thresh} Hertz threshold pressure for the generation of 2.2Å pits within a mica surface

$p(r)$ Hertz pressure distribution as a function of radial position from contact center

PC polycarbonate

PS polystyrene

r_s critical contact radius upon separation (within the JKR limit)

R_g polymer macromolecules unperturbed radius of gyration

R, R_{tip}	tip radius of curvature
$R_{surface}$	surface radius of curvature
R^*	reduced radius of curvature
res	image resolution
σ_y	yield modulus
t	thickness of a rectangular cantilever
T_g	polymer glass transition temperature
W_{adh}	work of adhesion
w	width of a rectangular cantilever

Chapter 1.

Overview of Surfaces and Nanotribology

1.1 Introduction

The area of nanotribology has advanced greatly in the past 19 years with the introduction of scanned probe microscopies[1,2] for the characterization of surface properties.[3-10] The ability to probe the details of structure, friction and adhesion on a local atomic/molecular scale affords a definitive approach for understanding the mechanisms of wear at the most fundamental level. Muscovite mica, a layered alumino-silicate in the form of $KAl_2(Si_3AlO_{10})(OH)_2$, has been a suitable standard for the investigation of the atomic scale relationship between friction,[11-27] adhesion[11,14,15,17,24,26,28-32] and wear[15-17,24,33,34] by atomic force microscopy[1] (AFM) due to the ability to readily generate large areas of atomically smooth surface. The rich solution chemistry of mica, attributed to the Brønsted acid sites (Si-O(H)-Al) within the basal (001) plane and its alternating sheet structure combine with the vast atomically flat surface areas created when cleaved to give a model substrate for examining a variety of phenomena. These include studies of double layer forces,[29,31,35-41] van der Waals forces,[39,42-44] ion binding and mobility,[36,45-47] monitoring the recoil tracks of alpha particles,[18,48] the characteristics of polymers at interfaces[39,49,50] and ordering of discrete water layers.[39,44,51]

As the area of nanotribology is quite vast,[6,52,53] an overview of the techniques employed to probe surface related phenomena will be discussed with a focus on the methods for direct observation of charge nucleation and defect formation, further limited

to scanned probe microscopy studies. We will first begin with a description of the structure and chemistry of the mica surface, which will be followed by an overview of the scanned probe methodologies employed in the investigation of nanotribological properties of mica surfaces. This includes the basic operating principles of the atomic force microscope (AFM), lateral force (or friction) measurements by AFM, as well as adhesion measurements. Moreover, as one wishes often to quantify such details we will also describe methodologies employed to calibrate the signals retrieved from such experiments.

1.2 Mica as A Model Substrate

The outermost mica surface typically exposes a hexagonally arrayed pattern of oxygen atoms, with a periodicity of 0.52 nm, Figure 1.1a. Mica is comprised of a layered alumino-silicate structure with a periodicity of 1.0 nm normal to the (001) crystal basal plane, Figure 1.1b, which is defined by a repeating boundary layer of K^+.[54,55] The K^+ ions electrostatically bind the sheets together and act to neutralize the net negative charge associated with the partial substitution of Si with Al (on average one out of every four). It is at these boundaries that cleavage is preferred and is where shearing of the layers most readily occurs. Under aqueous conditions of low electrolyte concentrations, the outermost K^+ layers are solvated and exchanged with H^+.[20,31,35-37,45,47] This ready displacement has hindered direct imaging of the K^+ terminated mica surface in solution. The surface of mica may also be readily functionalized by a range of chemistries. Some of the most popular involve the organization of self-assembled monolayers of triethoxy- or trichloro- derivitized alkylsilanes, which can form densely packed structures on

mica.[21,56-66] This provides a means of investigating lubricant layers as protective barriers for the minimization of friction and wear.

To date, the majority of surface wear studies have focused on the evaluation of surface structure before and after wear,[16,34,67-72] thus missing the key stage of the nucleation of defects that ultimately results in the gross structural changes observed. While some studies have investigated the time evolution of wear using scanned probes,[15,17,73-78] the different approaches presented can make it difficult to compare experiments from different labs and a more standardized approach is required. This is in part due to the typically large contact area between the AFM tip and the surface being worn, which frequently exceeds the area density of defects nucleated. Thus, an averaging over the contact renders the low population of defects "invisible" to the probe tip until gross wear has occurred.

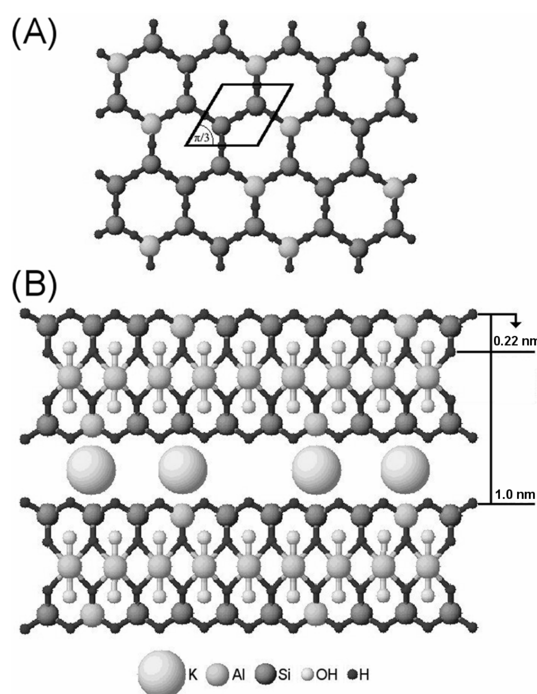

Figure 1.1 a) Pictorial representation of the mica(001) cleavage plane showing the 0.52 nm lattice periodicity. b) Repeating layered structure of mica along the c-axis with interlayer distances referenced to the basal plane.

Investigations of the wear of oxide surfaces such as mica and silica have unique difficulties when probing wear at the atomic level, and are associated with the chemical complexity of the surfaces, especially in the presence of water[72,79-88] where the surface charge density is highly pH dependent.[67,80-82,89,90] A recent demonstration by Maw *et al.* illustrates the incongruous wear behavior that exists for ceramics in aqueous solution (pH = 7).[33] Specifically, they found that a Si_3N_4 tip exhibited pronounced wear after being rastered against a quartz substrate for 25 scans at ~120 nN of force. However, under similar conditions the Si_3N_4 tip exhibited little wear when the surface was mica. Here the disparity has been attributed to the relevant population of silanol (Si-OH) groups that can form bonds between the tip and substrate, which facilitates removal of tip materials. As the basal plane of mica possesses a Brønsted acid site, due to the 1 in 4 substitution of Si for Al, it is expected that the ionization potential of the surface is largely controlled by this site (at least at lower pH's) and therefore the chemically active $Si\text{-}O^-$ or M-OH should be in minute quantities.[41,47,66,91] Since the isoelectric point (IEP) of quartz is between pH 2-3, it is apparent that at pH 7 a significant number of $Si\text{-}O^-$ and Si-OH groups are available for condensation at the tip - quartz contact.[79] The influence of such tribochemically active species in initiating surface degradation is evident and illustrates the necessity to account for this when choosing material pairs for a given application, i.e. the chemistries should be complementary. This certainly applies to device applications such as microelectromechanical systems (MEMS) where interfacial chemical forces can readily dominate the moving contacts within the device.[71,92-97]

The organization of the water molecules[39,44,51] and counter ions[20] immediately at the oxide surface may also impact the evolution of surface defects. Studies of the

influence of water on the wear of oxide surfaces show a critical dependence on the amount of water present[15] and in the case of solvation of the surface, the local pH of the surrounding water environment. Much of the wear processes present at oxides can be attributed to the catalytic activity of water (more appropriately the OH^- ion) on the metal-oxygen and silicon-oxygen bonds present on such surfaces, the details of which have been investigated for many years.

1.3 Scanned Probe Methodologies

1.3.1 Atomic Force Microscopy: General Methodology

In atomic force microscopy, a sharp tip with a radius of curvature ranging between 10 – 100 nm is scanned over a surface using a piezoelectric translator to control the position of the tip relative to the sample. The forces acting between the tip and sample (these can be van der Waals, electrostatic, or magnetic in nature) act to attract or repel the tip to or from the surface, which in turn alters the bending of the lever to which the tip is attached. In most conventional AFMs, lever deflections are detected by reflecting a laser beam off the back of the cantilever onto a quadrant photodiode. The photodiode signals are split to allow detection of the normal or torsional motions of the cantilever-tip assembly (Figure 1.2). These motions can in turn (when appropriately calibrated, as discussed later) be translated into the normal (F_z) and lateral frictional forces (F_f) acting between the tip and surface. The AFM can be operated in several imaging modes, including contact, non-contact/tapping, amplitude and phase modulated force or frictional force imaging. For nanotribological studies, contact and frictional force imaging modes are the most frequently employed.

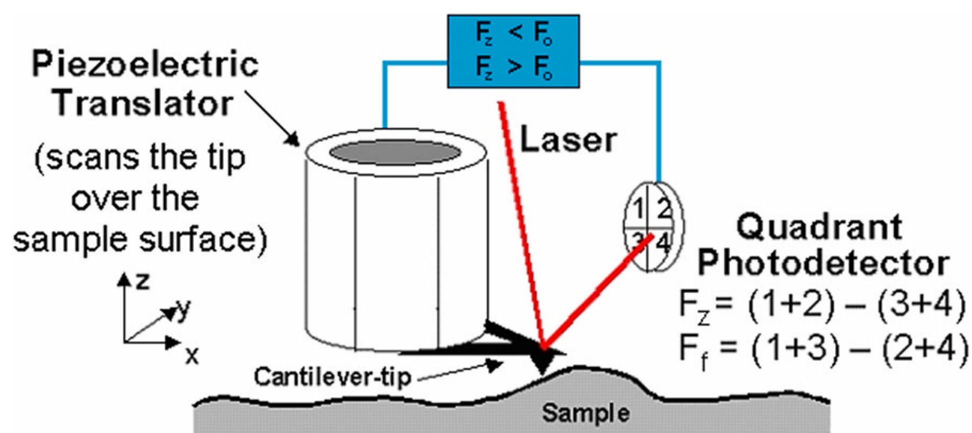

Figure 1.2 Schematic of an atomic force microscope. In this configuration the tip is scanned over a fixed sample. The cantilever-tip assembly is mounted on a piezoelectric translator, which controls the tip position over the surface. In contact mode, the tip is pressed against the surface until a fixed set-point force is reached (F_o). The deflection of the lever is detected by a quadrant photodiode from which the normal force (F_z) and torsional (frictional) force (F_f) may be measured. As the tip is scanned over the surface a feedback loop raises and lowers the tip depending on whether the normal force is larger than or less than the set point force to maintain a constant force.

1.3.2 Contact Mode Topography (Height) Measurements

In contact mode the tip is brought into contact with the surface until the lever experiences a fixed amount of deflection. Assuming that this amount of deflection stays within a linear limit, then a Hooke's law response can be assumed. If the lever spring constant is known (see below) then the amount of deflection can be converted into the force applied between the tip and surface. During imaging, a feedback loop is then used to maintain a fixed amount of lever deflection (constant normal force) by repeatedly moving the piezoelectric translators up and/or down, hence following the topography (normal force) of the surface. The lateral force (cantilever torsion) signals are concomitantly acquired with the topographic images allowing for correlations to be drawn between the two. The lateral force signal is an excellent indicator of changes in local chemistry even when obvious topographic differences are not present. For example, the spatial organization of films consisting of both hydrophobic and hydrophilic end-

groups, which have the same thickness and appear uniform in topography, are readily distinguished in lateral force images.[98]

1.3.3 Lateral Force (Friction And Shear) Measurements

While qualitative lateral force, or frictional response, can be readily obtained by AFM, quantifying frictional forces can be a daunting task. This is due to the difficulties associated with calibration of the lateral spring constants for AFM cantilevers (see below). Here we briefly discuss the type of information, which may be obtained from lateral force or shear force measurements. In lateral force measurements, friction is assessed using a friction loop. The friction loop is generated from the forward and reverse scans plotting the lateral force data vs. distance (Figure 1.3). Initially the tip sticks to the surface and the torsional force on the lever increases without the sliding motion of the tip. Once the static friction has been overcome, then the tip will begin to slide over the surface and the sliding friction may be determined (Figure 1.3). The shear modulus of the surface may also be measured using this same basic approach.[99] In order to evaluate the shear modulus, the tip is oscillated in the scan direction and the slope of the friction force (F_f) vs. distance signal is measured prior to sliding, i.e. within the static friction limit. This slope value contains the combined stiffness of the tip-sample contact (Eq. 1.1) from which the shear modulus of the surface may be determined.

$$\frac{dF_f}{dx} = k_{total} = \left(\frac{1}{k_{lever}} + \frac{1}{k_{contact}} \right)^{-1} \tag{1.1}$$

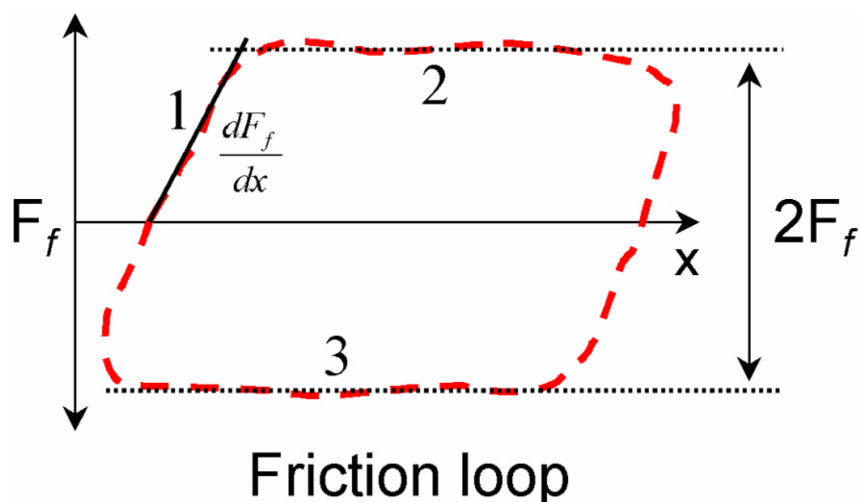

Figure 1.3 Schematic of an AFM friction loop. Initially the tip sticks to the surface (1) until the static friction between the tip and surface is overcome. The tip then enters a sliding friction regime (2). As the scan is reversed, the signal in the photodetector become negative (3) and a reverse trace is produced. The "frictional" force is the average of the forward and reverse friction traces. The stiffness of the contact may be deduced from the slope of the friction loop (dF_f/dx) prior to sliding.

A significant advantage of this measurement is that the details of the tip size ultimately falls out of the calculation, removing a potential source of error from the measurement. The reader is directed to the literature for a complete description of lateral stiffness measurements.[99]

1.4 Making Quantitative Measurements

1.4.1 Calibration of AFM Cantilevers

AFM cantilevers can be purchased from numerous sources and most frequently come as V-shaped or rectangular springboard shaped levers. The levers are generally made from silicon and silicon nitride. Coatings are often applied to enhance the reflectivity of the laser beam. The reflective coating, however, can add strain to the levers when used in vacuum due to heating. The average lever spring constants provided

by the manufacturer are often inaccurate and quantitative measurements should not be based on these values. Therefore each lever should be independently calibrated, preferably via an *in situ* methodology.

The determination of lever force constants is less demanding for a rectangular cantilever beam,[100] but it still requires non-trivial details of the lever's dimensions and physical constants, e.g. modulus and Poisson ratio. These details become more difficult to define for metal-coated levers, as the coating can significantly modify the lever's elastic properties. For a rectangular beam of length L, width w, thickness t, Young's modulus E, the cantilevers stiffness k_{lever}^{normal} is given by:

$$k_{lever}^{normal} = \frac{Ewt^3}{4L^3} . \tag{1.2}$$

Errors inherent to the determination of the spring constant come from difficulties in accurately measuring (by scanning electron microscopy, SEM) the thickness of the lever. Also, for chemical vapor deposited silicon nitride levers, variations in E can also occur. If a bulk value for E is used, the thickness can be determined by measuring the resonance frequency of the cantilever.[101] However, this method only works for uncoated monolithic cantilevers.[102] The formulae for the spring constants for V-shaped levers are much more complicated.[103] Uncoated, single crystal silicon cantilevers are perhaps the best choice for which the force constant can be readily determined by finite element models, Eq. (1.2), and the resonance frequency.[104]

A range of methods for the calibration of the normal[101-116] and torsional (lateral) force constants[103,107,112,117,118] of AFM cantilevers have been described. A recent method

proposed by Sader *et al.* appears to be reliable and simple to perform for rectangular levers.[109] It relies on measuring the resonance frequency and the quality factor of the cantilever in air. Use of the hydrodynamic function relates the damping of the lever resonance by air to the quality factor, and the dependence of E and t are eliminated from the resulting formula for the force constant.

1.4.2 Probe Tip Characterization

A problem of quite a different nature is an accurate measurement of the AFM tip shape and composition. With respect to tip geometry, continuum mechanics requires *a priori* knowledge of the probe shape, mechanical properties, and physical dimensions in order for the models to be employed.[119,120] Carpick *et al.* have illustrated this point rather succinctly in an instructive set of experiments with non-parabolic Pt tips on a mica substrate in UHV.[13]

There are several *in-situ* methods to characterize the tip shape, where an AFM topographic image is employed in order to deconvolute the tip and sample geometry.[121-123] Separation of the tip and sample contributions by contact imaging of known, or at least sharp, sample features allows determination of tip shape.[106,107,122,124-133] With this method, the proximal tip shape and radius of curvature (R) can be determined by imaging and analyzing topographic profiles of a $SrTiO_3$(305) single crystal.[124] Briefly, by fitting the topography line traces across the $SrTiO_3$ (100)/(001) steps with a second order polynomial, the tip radius of curvature (R) can be extracted by solving for the circle of curvature (K) at the asperity apex. The circle of curvature (K) can be evaluated for any point on a function ($f(x)$) which describes the proximal tip shape. Once K has been

evaluated, then the tip radius of curvature (R) is simply equal to the inverse of the circle of curvature ($R = 1/K$). Further information on tip shape characterization with this method can be found in Appendix 1.1.

Ex-situ tip imaging by electron microscopy has also been performed.[105] Some of these measurements have revealed that a number of microfabricated cantilevers possess double tips and other unsuitable tip structures.[124,127,132] This demonstrates the importance of tip characterization in nanotribological measurements. Thin film coatings applied to the microfabricated levers can provide robust, smooth and even conductive coatings.[134,135] Further work in this direction would be useful, so as to provide a wider array of dependable tip structures and materials. In fact, a recent demonstration of injected molded, polymer AFM cantilevers is an interesting departure from the conventional tip fabrication methods.[136]

Detailed control of tip chemistry is still a difficulty of scan probe studies with commonly employed tips (e.g silicon nitride) possessing a variable stoichiometry.[90,114,137] Coating with inert metals (such as Au or Pt) or functionalization with alkylsilanes or alkanethiols is often useful, however one must be aware of the "chemical" compatibility and how this can translate into "anomalous" wear behavior.[33] The chemical composition of the tip is equally important, but is also challenging to determine or control. Xiao and co-workers have shown that the AFM tip is readily chemically modified when scanned in contact with various materials,[26] even tips that have been coated with self-assembled monolayers in order to control their chemistry. They recommend "running in" the tip with a standard sample to give reproducible results. The stresses that take place in a nano-

contact can be very large (>1 GPa ~ 145,038 psi) and so modification of both the chemistry and structure of the tip is an important consideration.

1.4.3 Adhesion Measurements

When quantifying adhesion and interfacial energies from AFM measurements, often the contact mechanics model developed by Johnson, Kendall and Roberts (JKR)[120,138] is employed to analyze adhesion data from force-distance spectroscopy. Determination of the most appropriate continuum mechanics model to use, however, requires consideration of the range of forces and the materials operative at the contact. The JKR model is often applied to highly adhesive, compliant contacts, while the Derjaguin-Müller-Toporov (DMT) model relates to stiff, weakly adhering contacts.[119,139] A significant effort has been put forth to identify which model is most appropriate and therefore best describes the contact for a given material pair. The reader is directed to the references for the complete treatments of this topic.[138-141] The application of such models to AFM force of adhesion measurements (F_{adh}) enables the number of interacting species (and consequently the average 'unit' interaction force or energy) to be derived from the estimated contact area and the average molecular packing density. Figure 1.4 depicts the sequence of events that occurs during acquisition of F_{adh} measurements. Using the JKR model the F_{adh} (AFM pull-off force) is related to the work of adhesion, W_{adh}, and the reduced radius, $R^* = (1/R_{\text{tip}} + 1/R_{\text{surface}})^{-1}$, of the tip-surface contact:

$$F_{adh} = \frac{3}{2}\pi R^* W_{adh}. \quad (1.3)$$

The work of adhesion, a formalism of Dupré from 1869, is a combination of the tip-surface (γ_{ts}), tip-solvent (γ_{tl}) and surface-solvent (γ_{sl}) interfacial energies ($W_{adh} = \gamma_{sl} + \gamma_{tl} - \gamma_{ts}$). For tip-surface combinations that have the same chemical composition, the surface energy may be estimated directly from the adhesion measurement ($W_{adh} = 2\gamma_{sl}$) since $\gamma_{sl} = \gamma_{tl}$ with $\gamma_{ts} = 0$. Furthermore, the effective contact radius at separation, r_s, from the JKR model is given as:

$$r_s = \left(\frac{3\pi W_{adh} R^{*2}}{2\varepsilon} \right)^{\frac{1}{3}} \tag{1.4}$$

where ε is the reduced elastic moduli of the tip and surface. Using the contact area at separation and the assumed packing density of the molecules at the surfaces in contact, an estimate of the adhesion force or interaction energy on a per molecule basis can be made.

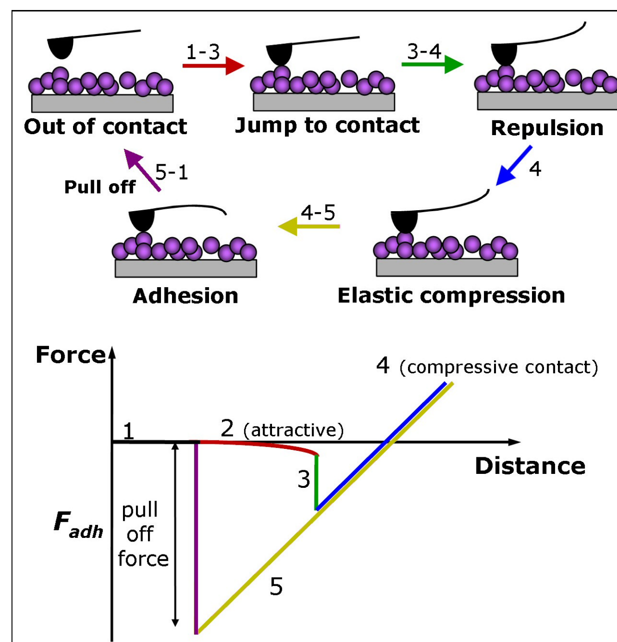

Figure 1.4 Schematic of AFM force-distance spectroscopy and the events leading to measurement of the force of adhesion (F_{adh}). (1) Initially the tip is out of contact. (2) Upon approaching the surface the tip jumps into contact and (3-4) makes physical, compressive contact with the surface. (5-1) During retraction of the cantilever-tip assembly from the surface, a non-zero adhesive interaction acting between the tip and substrate requires the pull off force (F_{adh}) to be overcome in order to separate the tip from the surface.

The accuracy of the interfacial energies and per molecule values obtained with this approach must be carefully evaluated, as several sources of error exist in the various elements of the calculation. These include imprecise knowledge of the contact, including the tip radius, packing densities of molecular monolayers on modified surfaces, as well as unknown elastic properties of the contact. Such properties are typically assumed to be dominated by those of the underlying substrate, and the bulk values of the surface and/or tip materials (Au, Si, mica, Si_3N_4, SiO_2) are often employed in these calculations.[60-62,142] Moreover, as mentioned above, if the molecular packing densities of the monolayers being evaluated are not known (as is frequently the case with a typical AFM tip), then estimations must be employed.

1.4.4 What Is A Single AFM Scan?

Although this seems to be a simple question, there is in fact ambiguity in the definition of a single AFM image scan. Unlike the intense effort put forth to calibrate the AFM cantilevers physical properties, this aspect of AFM nanotribology studies was not addressed until the work described in Chapter 3. With atomic force microscopy tips, acting as single asperities, proving indispensable in mediating the transition of a substrate surface from its native to a modified "defective" state,[15,74-78,143-145] it is desirable to assure consistent frequency (number of scan cycles) versus load dependent wear trials. A quick appraisal of the typical experimental parameters used when conducting nanoscale AFM wear studies immediately brings to light a significant oversight related to the contact diameter and the dimensions of the AFM scan area. This oversight has the potential to inhibit unification of nanoscale empirical evidence, pertaining to the intimate details of

defect nucleation, with a materials micro and macroscopic wear behavior. In order to properly aid the current effort of wear map modeling on the micro and macroscopic scales,[52,146] situations with multiple asperity contacts and a multitude of wear mechanisms operating in concert, the accuracy of AFM wear studies must be assured. To ease comparison of data compiled from numerous research facilities within the field, a guideline outlining the optimal experimental protocol to *condition* AFM data sets is therefore necessary. As discussed in Chapter 3, a straightforward model has been developed to realize this benchmark for AFM experimental studies by eliminating the overlap of sequential line traces during wear trials. Numerical simulations and empirical tests evaluating a materials nanotribological behavior clearly indicate that scan overlap can indeed compromise nanoscale scanned probe studies. The model proposed in Chapter 3 establishes the relevant relationships between the AFM scanning parameters and the finite dimension of the tip-surface contact to:

i. Standardize the requirements to perform a single AFM image scan over all applied loads and all (excluding raster rate) scanning parameter combinations;

ii. quantify the additional scan history that line-scan overlap imparts to a surface;

iii. predict the impact of line scan overlap on the propagation of tip mediated defects;

iv. eliminate the systematic error in reported scan history (experimental number of scans, N_{scans}^{Exp}) for wear trials performed with line-scan overlap; and

v. establish a general expression that enables previously determined activation parameters for defect nucleation from load (F_z) and frequency (N^{Exp}_{scans}) dependent studies to be reevaluated.

This analysis can improve upon the recent developments in modeling tip mediated surface phenomena. In particular the tip activated dissolution of calcite and brushite by Dickinson *et al.* has given impressive results and holds promise for evaluating other "model" systems such as mica.[75-78] Salmeron and Kopta have recently employed a model, similar to the one used by Dickinson *et al.*, in their studies of tip induced mica surface degradation under low vacuum with variable humidity.[15] In this work the objective was to evaluate the critical defect density necessary for the onset of gross surface degradation (abstraction of the surface terminating SiO_3 molecular fragments). The progressive layer removal illustrated the fidelity of inducing defects, however, linear regression analysis obtained a collected physical constant (B_0) that was appreciably higher than anticipated. Although the source of this deviation is presently unknown, it does appear that our model of scan overlap could reduce this error and therefore improve the fitted results.

1.5 Summary

In this chapter we have described the basic methods of how scanning probe microscopy experiments are conducted and how calibration of the cantilevers force constant and tip shape can be achieved for quantitative AFM studies. The area of nanotribology of oxides and the probing of defect nucleation at the atomic level by AFM is just beginning. Continuing developments in AFM technology and standardized

experimental protocols are refining our present understanding of tribochemically and mechanically enhanced wear processes.

Appendix 1.1 - Proximal Tip Shape Characterization

Imaging the reconstructed $SrTiO_3$ (305) single crystal effectively images the profile of the AFM tip due to the atomically sharp $SrTiO_3$ (100)/(100) facets present on the surface (Figure A1.1). The AFM tip profile (i.e. radius of curvature) can therefore be extracted by fitting the topographic line traces with a differentiable function $f(x)$. Typically the function is a second order polynomial, $f(x) = a + bx + cx^2$, and commercial curve fitting software (e.g. Excel) provides least squares analysis. After the respective coefficients are obtained, we can then find the circle of curvature (K) of the function $f(x)$ at any given point on the curve. By definition the circle of curvature K, is the rate of change of the tangent vector to the arc length rate of change:

$$K = \frac{|f(x)''|}{\left[1 + (f(x)')^2\right]^{3/2}} . \qquad \text{(A1.1)}$$

The tip radius of curvature (R) can then be obtained through the inverse relationship of R with K:

$$R = 1/K \qquad \text{(A1.2)}$$

Since we are interested in the radius of curvature of the tip at its apex, where $f(x)'$ for the second order polynomial equals 0, than eq. (A1.1 and A1.2) can be combined and simplified:

$$R = 1/|f(x)''| . \qquad \text{(A1.3)}$$

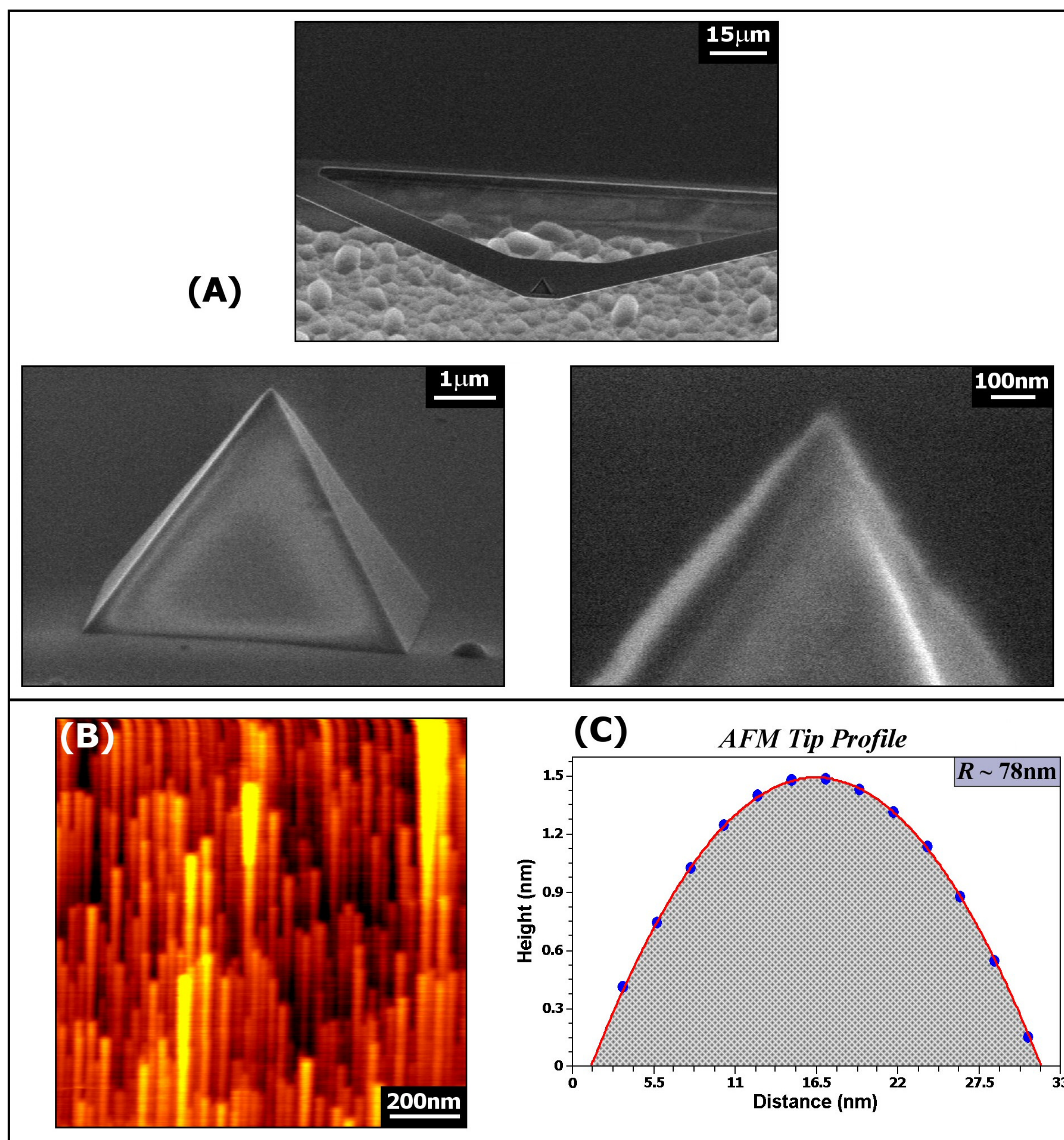

Figure A1.1 a) Low and high resolution scanning electron microscope (SEM) images of a Si_3N_4, V-shaped AFM tip-cantilever assembly. b) AFM topographic micrograph of the reconstructed $SrTiO_3$ (305) single crystal. c) Topography cursor profile of a single $SrTiO_3$ (305) from the topography image (b). The profile was used to calculate the AFM tip's radius of curvature (R), where curve fitting procedures find an $R \sim 78$ nm.

Chapter 1 References

(1) Binnig, G.; Quate, C. F.; Gerber, C. *Phys. Rev. Lett.* **1986**, *56*, 930.

(2) Binnig, G.; Gerber, C.; Stoll, E.; Albrecht, T. R.; Quate, C. F. *Europhys. Lett.* **1987**, *3*, 1281.

(3) Mate, C. M.; McClelland, G. M.; Erlandsson, R.; Chiang, S. *Phys. Rev. Lett.* **1987**, *59*, 1942.

(4) Burnham, N. A.; Colton, R. J. *Journal of Vacuum Science & Technology A - Vacuum Surfaces and Films* **1989**, *7*, 2906.

(5) Nyffenegger, R. M.; Penner, R. M. *Chem. Rev.* **1997**, *97*, 1195.

(6) Carpick, R. W.; Salmeron, M. *Chem. Rev.* **1997**, *97*, 1163.

(7) Bhushan, B.; Israelachvili, J. N.; Landman, U. *Nature* **1995**, *374*, 607.

(8) Landman, U.; Luedtke, W. D.; Burnham, N. A.; Colton, R. J. *Science* **1990**, *248*, 454.

(9) Dedkov, G. V. *Physica Status Solidi A - Applied Research* **2000**, *179*, 3.

(10) Singer, I. L. *Journal of Vacuum Science & Technology A - Vacuum Surfaces and Films* **1994**, *12*, 2605.

(11) Tang, H.; Joachim, C.; Devillers, J. *J. Vac. Sci. Technol., B* **1994**, *12*, 2179.

(12) Erlandsson, R.; Hadziioannou, G.; Mate, C. M.; McClelland, G. M.; Chiang, S. *J. Chem. Phys.* **1988**, *89*, 5190.

(13) Carpick, R. W.; Agrait, N.; Ogletree, D. F.; Salmeron, M. *J. Vac. Sci. Technol., B* **1996**, *14*, 1289.

(14) Carpick, R. W.; Agrait, N.; Ogletree, D. F.; Salmeron, M. *Langmuir* **1996**, *12*, 3334.

(15) Kopta, S.; Salmeron, M. *J. Chem. Phys.* **2000**, *113*, 8249.

(16) Miyake, S. *Appl. Phys. Lett.* **1994**, *65*, 980.

(17) Hu, J.; Xiao, X. D.; Ogletree, D. F.; Salmeron, M. *Surf. Sci.* **1995**, *327*, 358.

(18) Hagen, T.; Grafstrom, S.; Ackermann, J.; Neumann, R.; Trautmann, C.; Vetter, J.; Angert, N. *J. Vac. Sci. Technol., B* **1994**, *12*, 1555.

(19) Qian, L. M.; Luo, J. B.; Wen, S. W.; Xiao, X. D. *Chin. Sci. Bull.* **2001**, *46*, 349.

(20) Xu, L.; Salmeron, M. *Langmuir* **1998**, *14*, 2187.

(21) Wei, Z. Q.; Wang, C.; Bai, C. L. *Langmuir* **2001**, *17*, 3945.

(22) Hoshi, Y.; Kawagishi, T.; Kawakatsu, H. *Jpn. J. Appl. Phys., Part 1* **2000**, *39*, 3804.

(23) Piner, R. D.; Mirkin, C. A. *Langmuir* **1997**, *13*, 6864.

(24) Schwarz, U. D.; Zworner, O.; Koster, P.; Wiesendanger, P. *Phys. Rev. B: Condens. Matter* **1997**, *56*, 6997.

(25) Tsujimichi, K.; Tamura, H.; Hirotani, A.; Kubo, M.; Komiyama, M.; Miyamoto, A. *J. Phys. Chem., Part B* **1997**, *101*, 4260.

(26) Qian, L. M.; Xiao, X. D.; Wen, S. Z. *Langmuir* **2000**, *16*, 662.

(27) Gyalog, T.; Bammerlin, M.; Luthi, R.; Meyer, E.; Thomas, H. *Europhys. Lett.* **1995**, *31*, 269.

(28) Christenson, H. K. *J. Phys. Chem.* **1993**, *97*, 12034.

(29) Teschke, O.; de Souza, E. F. *Appl. Phys. Lett.* **1999**, *74*, 1755.

(30) Knarr, R. F.; Quon, R. A.; Vanderlick, T. K. *Langmuir* **1998**, *14*, 6414.

(31) Vakarelski, I. U.; Ishimura, K.; Higashitani, K. *J. Colloid Interface Sci.* **2000**, *227*, 111.

(32) Weisenhorn, A. L.; Maivald, P.; Butt, H. J.; Hansma, P. K. *Phys. Rev. B: Condens. Matter* **1992**, *45*, 11226.

(33) Maw, W.; Stevens, F.; Langford, S. C.; Dickinson, J. T. *J. Appl. Phys.* **2002**, *92*, 5103.

(34) Liu, E.; Blanpain, B.; Celis, J. P.; Roos, J. R. *J. Appl. Phys.* **1998**, *84*, 4859.

(35) Pashley, R. M. *J. Colloid Interface Sci.* **1981**, *83*, 531.

(36) Raviv, U.; Laurat, P.; Klein, J. *J. Chem. Phys.* **2002**, *116*, 5167.

(37) Kjellander, R.; Marcelja, S.; Pashley, R. M.; Quirk, J. P. *J. Chem. Phys.* **1990**, *92*, 4399.

(38) Teschke, O.; Ceotto, G.; de Souza, E. F. *Phys. Chem. Chem. Phys.* **2001**, *3*, 3761.

(39) Israelachvili, J. N. *Intermolecular and Surfaces Forces*, 2nd ed.; Academic Press: New York, 1992.

(40) Basu, S.; Sharma, M. M. *J. Colloid Interface Sci.* **1996**, *181*, 443.

(41) Toikka, G.; Hayes, R. A. *J. Colloid Interface Sci.* **1997**, *191*, 102.

(42) Tabor, D.; Winterton, R. H. S. *Proceedings of the Royal Society of London Series a-Mathematical Physical and Engineering Sciences* **1969**, *312*, 435.

(43) Hutter, J. L.; Bechhoefer, J. *J. Vac. Sci. Technol., B* **1994**, *12*, 2251.

(44) Pashley, R. M.; Israelachvili, J. N. *J. Colloid Interface Sci.* **1984**, *101*, 511.

(45) Xu, L.; Salmeron, M. *Langmuir* **1998**, *14*, 5841.

(46) Purton, J. A.; Allan, N. L.; Blundy, J. D. *J. Mater. Chem.* **1997**, *7*, 1947.

(47) Nishimura, S.; Biggs, S.; Scales, P. J.; Healy, T. W.; Tsunematsu, K.; Tateyama, T. *Langmuir* **1994**, *10*, 4554.

(48) Snowdenifft, D.; Price, P. B.; Nagahara, L. A.; Fujishima, A. *Phys. Rev. Lett.* **1993**, *70*, 2348.

(49) Terashima, H. *Phys. Chem. Chem. Phys.* **2000**, *2*, 5252.

(50) Heuberger, M.; Luengo, G.; Israelachvili, J. N. *J. Phys. Chem., Part B* **1999**, *103*, 10127.

(51) Cantrell, W.; Ewing, G. E. *J. Phys. Chem., Part B* **2001**, *105*, 5434.

(52) *Modern Tribology Handbook*; 1st ed.; Bhushan, B., Ed.; CRC Press: Boca Raton, 2001; Vol. 1, pp 1460.

(53) *Nanotribology: Critical Assessment and Research Needs*; Hsu, S. M.; Ying, Z. C., Eds.; Kluwer Academic: Boston, 2003.

(54) Deer, W. A.; Howie, R. A.; Zussman, J. Rock-Forming Minerals. In *Sheet Silicates*; Longmans, Green and Co.: London, 1962; Vol. 3.

(55) Wyckoff, R. W. G. *Crystal Structures*; Interscience: New York, 1971.

(56) Woodward, J. T.; Ulman, A.; Schwartz, D. K. *Langmuir* **1996**, *12*, 3626.

(57) Eastman, T.; Zhu, D. M. *Langmuir* **1996**, *12*, 2859.

(58) Demirel, A. L.; Granick, S. *J. Chem. Phys.* **1998**, *109*, 6889.

(59) Barthel, E.; Roux, S. *Langmuir* **2000**, *16*, 8134.

(60) Wurger, A. *Phys. Rev. Lett.* **1999**, *83*, 1696.

(61) Kopta, S.; Barrena, E.; Ogleterre, D. F.; Charych, D. H.; Salmeron, M. *Phys. Rev. Lett.* **1999**, *83*, 1697.

(62) Barrena, E.; Kopta, S.; Ogletree, D. F.; Charych, D. H.; Salmeron, M. *Phys. Rev. Lett.* **1999**, *82*, 2880.

(63) Lio, A.; Charych, D. H.; Salmeron, M. *J. Phys. Chem., Part B* **1997**, *101*, 3800.

(64) Tian, F.; Xiao, X. D.; Loy, M. M. T.; Wang, C.; Bai, C. L. *Langmuir* **1999**, *15*, 244.

(65) Chen, Y. L.; Helm, C. A.; Israelachvili, J. N. *Langmuir* **1991**, *7*, 2694.

(66) Sterthaus, R.; Wegner, G. *Langmuir* **2002**, *18*, 5414.

(67) Batteas, J. D.; Quan, X. H.; Weldon, M. K. *Tribol. Lett.* **1999**, *7*, 121.

(68) Miyake, S. *J. Vac. Sci. Technol., B* **2003**, *21*, 785.

(69) Prioli, R.; Reigada, D. C.; Freire, F. L. *J. Appl. Phys.* **2000**, *87*, 1118.

(70) Reigada, D. C.; Prioli, R.; Jacobsohn, L. G.; Freire, F. L. *Diam Relat Mater* **2000**, *9*, 489.

(71) Sundararajan, S.; Bhushan, B. *Wear* **1998**, *217*, 251.

(72) Prioli, R.; Reigada, D. C.; Freire, F. L. *J. Appl. Phys.* **2000**, *88*, 679.

(73) Adams, J. B.; Hector, L. G.; Siegel, D. J.; Yu, H. L.; Zhong, J. *Surf. Interface Anal.* **2001**, *31*, 619.

(74) DeVecchio, D.; Bhushan, B. *Rev. Sci. Instrum.* **1998**, *69*, 3618.

(75) Scudiero, L.; Langford, S. C.; Dickinson, J. T. *Tribol. Lett.* **1999**, *6*, 41.

(76) Dickinson, J. T.; Hariadi, R. F.; Langford, S. C. *Ceram. Trans.* **1999**, *102*, 213.

(77) Park, N. S.; Kim, M. W.; Langford, S. C.; Dickinson, J. T. *Langmuir* **1996**, *12*, 4599.

(78) Park, N. S.; Kim, M. W.; Langford, S. C.; Dickinson, J. T. *J. Appl. Phys.* **1996**, *80*, 2680.

(79) Iler, R. K. *The Chemistry of Silica*; Wiley- Interscience: New York, 1979.

(80) Schmitz, I.; Schreiner, M.; Friedbacher, G.; Grasserbauer, M. *Anal. Chem.* **1997**, *69*, 1012.

(81) Fischer, T. E.; Mullins, W. M. *J. Phys. Chem.* **1992**, *96*, 5690.

(82) Zirl, D. M.; Garofalini, S. H. *Phys. Chem. Glasses* **1989**, *30*, 155.

(83) Hunger, M.; Freude, D.; Pfeifer, H.; Schwieger, W. *Chem. Phys. Lett.* **1990**, *167*, 21.

(84) Koller, H.; Lobo, R. F.; Burkett, S. L.; Davis, M. E. *J. Phys. Chem.* **1995**, *99*, 12588.

(85) Ruiz, J. M.; McAdon, M. H.; Garces, J. M. *J. Phys. Chem., Part B* **1997**, *101*, 1733.

(86) Xu, H.; Van Deventer, J. S. J. *Comput. Chem.* **2000**, *24*, 391.

(87) Sokol, A. A.; Catlow, C. R. A.; Garces, J. M.; Kuperman, A. *J. Phys. Chem., Part B* **2002**, *106*, 6163.

(88) Katsuki, F.; Kamei, K.; Saguchi, A.; Takahashi, W.; Watanabe, J. *J. Electrochem. Soc.* **2000**, *147*, 2328.

(89) Pal, S.; Banerjee, S. *J. Phys. D: Appl. Phys.* **2001**, *34*, 253.

(90) Lin, X. Y.; Creuzet, F.; Arribart, H. *J. Phys. Chem.* **1993**, *97*, 7272.

(91) Zembala, M.; Adamczyk, Z.; Warszyski, P. *Colloids and Surfaces A - Physicochemical and Engineering Aspects* **2001**, *195*, 3.

(92) Sniegowski, J. J.; de Boer, M. P. *Annu. Rev. Mater. Sci.* **2000**, *30*, 299.

(93) Maboudian, R.; Ashurst, W. R.; Carraro, C. *Tribol. Lett.* **2002**, *12*, 95.

(94) Maboudian, R.; Carraro, C. *J. Adhes. Sci. Technol.* **2003**, *17*, 583.

(95) Malek, C. G. K.; Das, S. S. *J. Vac. Sci. Technol., B* **1998**, *16*, 3543.

(96) Miller, S. L.; Rodgers, M. S.; La Vigne, G.; Sniegowski, J. J.; Clews, P.; Tanner, D. M.; Peterson, K. A. *Microelectron. Reliab.* **1999**, *39*, 1229.

(97) Komvopoulos, K. *Wear* **1996**, *200*, 305.

(98) Frisbie, C. D.; Rozsnyai, L. F.; Noy, A.; Wrighton, M. S.; Lieber, C. M. *Science* **1994**, *265*, 2071.

(99) Carpick, R. W.; Ogletree, D. F.; Salmeron, M. *Appl. Phys. Lett.* **1997**, *70*, 1548.

(100) Timoshenko, S. P.; Goodier, J. N. *Theory of Elasticity*, 3rd ed.; McGraw-Hill: New York, 1987.

(101) Cleveland, J. P.; Manne, S.; Bocek, D.; Hansma, P. K. *Rev. Sci. Instrum.* **1993**, *64*, 403.

(102) Sader, J. E.; Larson, I.; Mulvaney, P.; White, L. R. *Rev. Sci. Instrum.* **1995**, *66*, 3789.

(103) Neumeister, J. M.; Ducker, W. A. *Rev. Sci. Instrum.* **1994**, *65*, 2527.

(104) Tortonese, M.; Kirk, M. *SPIE Proc. - Micromach. Imag.* **1997**, *3009*, 53.

(105) Albrecht, T. R.; Akamine, S.; Carver, T. E.; Quate, C. F. *Journal of Vacuum Science & Technology A - Vacuum Surfaces and Films* **1990**, *8*, 3386.

(106) Siedle, P.; Butt, H. J.; Bamberg, E.; Wang, D. N.; Kuhlbrandt, W.; Zach, J.; Haider, M. *Inst Phys Conf Ser* **1993**, *130*, 361.

(107) Ogletree, D. F.; Carpick, R. W.; Salmeron, M. *Rev. Sci. Instrum.* **1996**, *67*, 3298.

(108) Sader, J. E. *Rev. Sci. Instrum.* **1995**, *66*, 4583.

(109) Sader, J. E.; Chon, J. W. M.; Mulvaney, P. *Rev. Sci. Instrum.* **1999**, *70*, 3967.

(110) Senden, T. J.; Ducker, W. A. *Langmuir* **1994**, *10*, 1003.

(111) Torii, A.; Sasaki, M.; Hane, K.; Okuma, S. *Meas. Sci. Technol.* **1996**, *7*, 179.

(112) Hazel, J. L.; Tsukruk, V. V. *J. Tribol. - Trans. ASME* **1998**, *120*, 814.

(113) Hutter, J. L.; Bechhoefer, J. *Rev. Sci. Instrum.* **1993**, *64*, 1868.

(114) Walters, D. A.; Cleveland, J. P.; Thomson, N. H.; Hansma, P. K.; Wendman, M. A.; Gurley, G.; Elings, V. *Rev. Sci. Instrum.* **1996**, *67*, 3583.

(115) Miyatani, T.; Fujihira, M. *Jpn. J. Appl. Phys., Part 1* **1997**, *36*, 5280.

(116) Levy, R.; Maaloum, M. *Nanotechnology* **2002**, *13*, 33.

(117) Cain, R. G.; Biggs, S.; Page, N. W. *J. Colloid Interface Sci.* **2000**, *227*, 55.

(118) Green, C. P.; Sader, J. E. *J. Appl. Phys.* **2002**, *92*, 6262.

(119) Maugis, D. *Contact, Adhesion and Rupture of Elastic Solids*; Springer-Verlag: Berlin, 2000; Vol. 130.

(120) Johnson, K. L. *Contact Mechanics*; Cambridge University Press: Cambridge, 1987.

(121) Villarrubia, J. S. *Surf. Sci.* **1994**, *321*, 287.

(122) Westra, K. L.; Mitchell, A. W.; Thomson, D. J. *J. Appl. Phys.* **1993**, *74*, 3608.

(123) Goss, C. A.; Brumfield, J. C.; Irene, E. A.; Murray, R. W. *Langmuir* **1993**, *9*, 2986.

(124) Sheiko, S. S.; Moller, M.; Reuvekamp, E. M. C. M.; Zandbergen, H. W. *Phys. Rev. B: Condens. Matter* **1993**, *48*, 5675.

(125) Atamny, F.; Baiker, A. *Surf. Sci.* **1995**, *323*, L314.

(126) Schneir, J.; Villarrubia, J. S.; McWaid, T. H.; Tsai, V. W.; Dixson, R. *J. Vac. Sci. Technol., B* **1996**, *14*, 1540.

(127) Dongmo, L. S.; Villarrubia, J. S.; Jones, S. N.; Renegar, T. B.; Postek, M.; Song, J. F. *Ultramicroscopy* **2000**, *85*, 141.

(128) Jarausch, K. F.; Stark, T. J.; Russell, P. E. *J. Vac. Sci. Technol., B* **1996**, *14*, 3425.

(129) Markiewicz, P.; Goh, M. C. *Rev. Sci. Instrum.* **1995**, *66*, 3186.

(130) Markiewicz, P.; Goh, M. C. *J. Vac. Sci. Technol., B* **1995**, *13*, 1115.

(131) Odin, C.; Aime, J. P.; Elkaakour, Z.; Bouhacina, T. *Surf. Sci.* **1994**, *317*, 321.

(132) Xu, L.; Yao, X. W.; Zhang, L. P.; Li, M. Q.; Yang, F. J. *Phys. Rev. B: Condens. Matter* **1994**, *49*, 2875.

(133) Xu, S.; Amro, N. A.; Liu, G. Y. *Appl. Surf. Sci.* **2001**, *175*, 649.

(134) Bietsch, A.; Schneider, M. A.; Welland, M. E.; Michel, B. *J. Vac. Sci. Technol., B* **2000**, *18*, 1160.

(135) Trenkler, T.; Hantschel, T.; Stephenson, R.; De Wolf, P.; Vandervorst, W.; Hellemans, L.; Malave, A.; Buchel, D.; Oesterschulze, E.; Kulisch, W.; Niedermann, P.; Sulzbach, T.; Ohlsson, O. *J. Vac. Sci. Technol., B* **2000**, *18*, 418.

(136) McFarland, A. W.; Poggi, M. A.; Bottomley, L. A.; Colton, J. S. *Nanotechnology* **2005**, *16*, 1249.

(137) Sekimoto, M.; Yoshihara, H.; Ohkubo, T. *J. Vac. Sci. Technol.* **1982**, *21*, 1017.

(138) Johnson, K. L.; Kendall, K.; Roberts, A. D. *Proceedings of the Royal Society of London Series A -Mathematical Physical and Engineering Sciences* **1971**, *324*, 301.

(139) Derjaguin, B. V.; Muller, V. M.; Toporov, Y. P. *J. Colloid Interface Sci.* **1975**, *53*, 314.

(140) Maugis, D. *J. Colloid Interface Sci.* **1992**, *150*, 243.

(141) Greenwood, J. A. *Proceedings of the Royal Society of London Series A - Mathematical Physical and Engineering Sciences* **1997**, *453*, 1277.

(142) Weihs, T. P.; Nawaz, Z.; Jarvis, S. P.; Pethica, J. B. *Appl. Phys. Lett.* **1991**, *59*, 3536.

(143) Adamson, A. W. *Physical Chemistry of Surfaces*; Wiley & Sons: New York, 1990.

(144) Carpick, R. W.; Dai, Q.; Ogletree, D. F.; Salmeron, M. *Tribol. Lett.* **1998**, *5*, 91.

(145) Helt, J. M.; Batteas, J. D. *Langmuir* **2005**, *21*, 633.

(146) Hsu, S. M.; Zhang, J.; Yin, Z. F. *Tribol. Lett.* **2002**, *13*, 131.

Chapter 2.

Atomic Scale Wear and Tip Mediated Defect Nucleation

2.1 Introduction

Although the nucleation of defects is a primary mechanism for energy dissipation leading to wear in tribological contacts,[5,6] there are few reports of the direct observation of defect nucleation *prior* to the onset of gross wear.[3,4,7-12] Muscovite mica, a layered alumino-silicate in the form of $KAl_2(Si_3AlO_{10})(OH)_2$, has been frequently employed as a model surface for the investigation of the atomic scale relationship between friction,[3,13-23] adhesion[16,21,24-30] and wear[3,19,31] by atomic force microscopy (AFM)[32] and surface forces apparatus[15,33-37] (SFA) measurements due to the ability to readily generate large domains of atomically smooth surface. The layered sheet structure of mica has an ~ 10 Å periodicity normal to the (001) crystal plane (Figure 2.1a), which is defined by the repeating boundary layers of K^+.[38] The K^+ ions electrostatically bind the layers together and act to neutralize the net negative charge associated with the partial substitution of Si with Al (on average one out of every four) in the basal plane. The K^+ interlayer demarcates the preferred cleavage planes and defines the atomic boundaries along which shearing of the layers most readily occurs. Under aqueous conditions, the outermost K^+ layer is exchanged into solution and therefore has yet to be imaged due to its ready displacement. With the K^+ ions solvated, the outermost mica surface exposes a hexagonally arrayed pattern of oxygen atoms with a 5.2 Å periodicity (Figure 2.1b).

AFM studies of mica surfaces have shown that under sufficiently high loads the surface becomes damaged and ~ 2 Å or ~ 10 Å deep holes are formed depending on the imaging conditions. Kopta and Salmeron have previously reported that in low vacuum (p ~ 10^{-2} Torr), for loads of up to 400 nN (i.e. Hertz mean pressure, p_m, of ~ 3.9 GPa; Appendix 2.1) no wear is found to occur.[3] However, following the introduction of approximately one monolayer of water to the surface (relative humidity > 50 %), wear scars appear within 1 – 5 scans at the same load. Additionally, with the presence of water at the surface the critical load for the formation of wear scars was observed to decline to

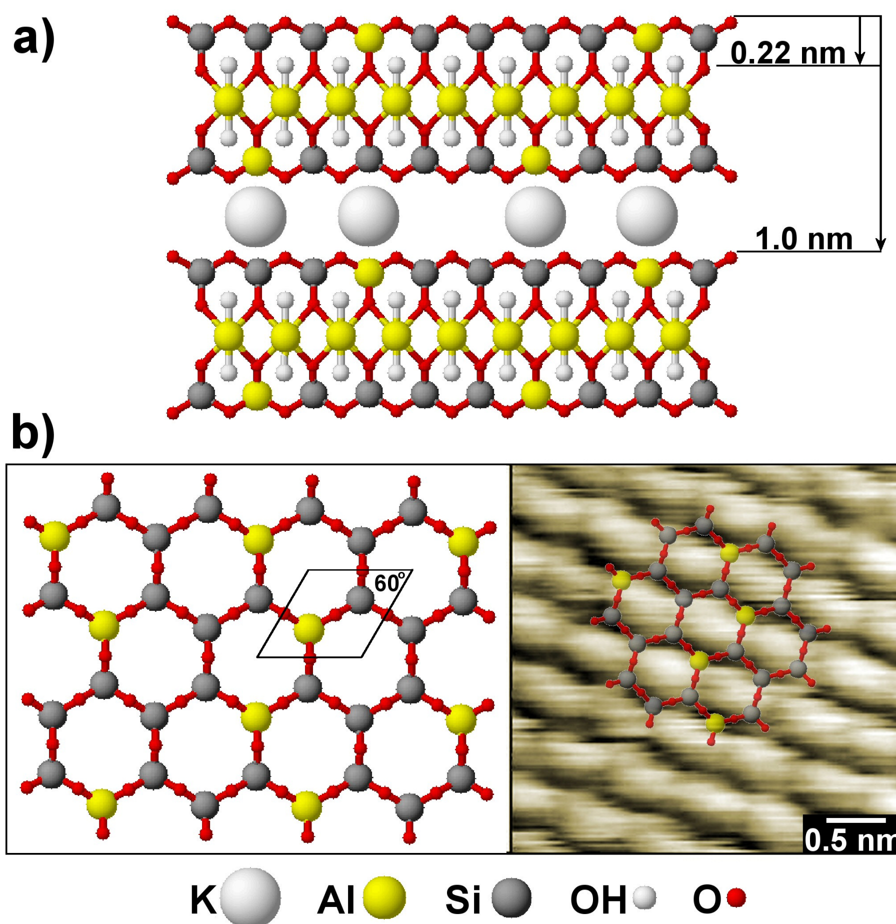

Figure 2.1 a) Cross-section depicting micas layered structure along the c-axis with interlayer distances referenced to the SiO_3/AlO_3 tetrahedral basal plane. b) A graphic representation and an unfiltered AFM topographic image (3.4 nm × 3.4 nm) of the mica (001) crystal plane showing the 5.2 Å lattice periodicity.

loads between 70 - 80 nN (p_m ~ 2.25 GPa).[3] Depending on the load and the number of repeated scans over a fixed area, scars ~ 2 Å or ~ 10 Å in depth could be formed. The ability to wear the surface, however, was reported to be independent of humidity above 50 %, corresponding to approximately a monolayer coverage of water,[39] indicating an important role of *interfacial* water in catalyzing the rupture of surface bonds. This is reasonable as water is known to promote hydrolysis of bridging Si-O-M bonds (where M is Si or Al).[40-45] Intuitively, one may anticipate that a saturated mica surface (such as a surface immersed in solution) would then possess tribochemical properties similar to that with monolayer coverage of water.

In this chapter, the wear of mica surfaces under aqueous environments of varied pH is explored. Using AFM we have evaluated the simultaneous changes in surface topography, friction and adhesion at the mica surface under controlled pH conditions. By altering solution conditions (pH) and applied load, the extent and nature of the observed wear was found to be influenced dramatically. In fact, with the appropriate control of applied load, number of scans and pH, we have been able, for the first time, to directly observe defect production (the breaking of terminal surface bonds) as detected in the form of a surface restructuring *prior* to the onset of gross wear. Here we distinguish defect nucleation from gross wear by taking the later as the point where pitting or abstraction of molecular surface fragments begins (i.e. the formation of 2 Å pits or scars). The degree of wear can be completely controlled by modification of imaging conditions and pH. Under low pH conditions (pH ≤ 3) the wear threshold pressure (p_{thresh}), relating to the formation of 2 Å pits, is equivalent to that of a simply humid environment and complete inhibition of wear (corresponding to an increase in the number of scans by

nearly an order of magnitude) is observed for these trials conducted at the p_{thresh} for higher pH studies.

2.2 Experimental

AFM images and force-distance measurements were made with a Molecular Imaging PicoSPM (Phoenix, AZ) coupled with an RHK Technology SPM 1000 Electronics, Revision 8 (Troy, MI). Images were typically collected at scan rates of 1.4 Hz to 33 Hz with an image resolution of 256 lines per image. All AFM data were collected in solutions with high purity water (EASYpure RF, 18.2 MΩ·cm, Barnstead, Dubuque, IA) at room temperature (22 ± 3°C). The pH of the solution environment was adjusted with HCl and KOH (Aldrich, Milwaukee, WI). The experiments employed commercially available Si (Silicon MDT, Tallinn, Estonia) and Si_3N_4 (ThermoMicroscopes, Santa Clara, CA) cantilevers. The normal force constant of each lever used (typically on the order of ~ 0.4 N/m) was individually calibrated against a lever of known spring constant.[46] The proximal tip shape and radius of curvature (R) of each AFM tip used was determined by imaging and analyzing topographic profiles of a $SrTiO_3$(305) single crystal.[47] Briefly, at least ten topography line traces across the $SrTiO_3$ (100)/(001) steps are fit with a second order polynomial and the tip radius of curvature (R) is then extracted by solving for the circle of curvature (K) at the asperity apex. The circle of curvature (K) can be evaluated for any point on a function ($f(x)$) which describes the proximal tip shape. Once K has been evaluated, then the tip radius of curvature (R) is simply equal to the inverse of the circle of curvature ($R = 1/K$). Further information on tip shape characterization with this method can be found in Chapter 1, Appendix 1.1. The

adhesive forces (F_{adh}) between the AFM tip and surface were determined from force-distance measurements with an approach- retract rate of ~ 50 μs per point, with 32 data points acquired every 4.52 Å, over a total range of 200 nm in each acquired force-distance curve. Prior to experimentation the AFM tips were oxidized and hydroxylated in a 4:1:1 mixture of high purity H_2O, 30% reagent grade H_2O_2 (Fisher) and concentrated NH_4OH (Fisher) at 80°C for ~ 1-5 minutes. The tips were then thoroughly rinsed with high purity H_2O and used immediately. During experiments the tip chemistry then varies with pH just as silica,[48] i.e. with a neutral silanol covered surface possessing an isoelectric point between pH 2 – 3, with a gradual charge increase via the formation of an anionic surface species with increasing pH (~ 0.004 charges/nm^2 – 2 charges/nm^2) over the range of pH 3 – 10.[49,50] The details related to the adhesion of silica surfaces by AFM as a function of pH has been previously discussed by Batteas et al.[51]

Muscovite mica (Structure Probe Inc., West Chester, PA) surfaces were prepared by cleavage with a fresh surface used for each experiment. Addition of the imaging solution to the disjoining surfaces was found to facilitate cleavage. Surface wear was evaluated by first imaging a large region of the surface (typically 1000 nm × 1000 nm) at low loads to avoid surface damage. Wear scans were then conducted in the center of this area (400 nm × 400 nm) at the desired load and number of scan cycles. The wear threshold pressures (p_{thresh}) were established for the said pH ranges using the Hertz mean pressure (p_m) description.[52,53] Here we define this threshold pressure as the contact pressure required to wear away the first layer of the mica surfaces, yielding a 2 Å deep wear scar within the limit of 10 scans. Returning to low load conditions and rescanning a larger region encompassing the trial area allowed for the resulting impact on surface

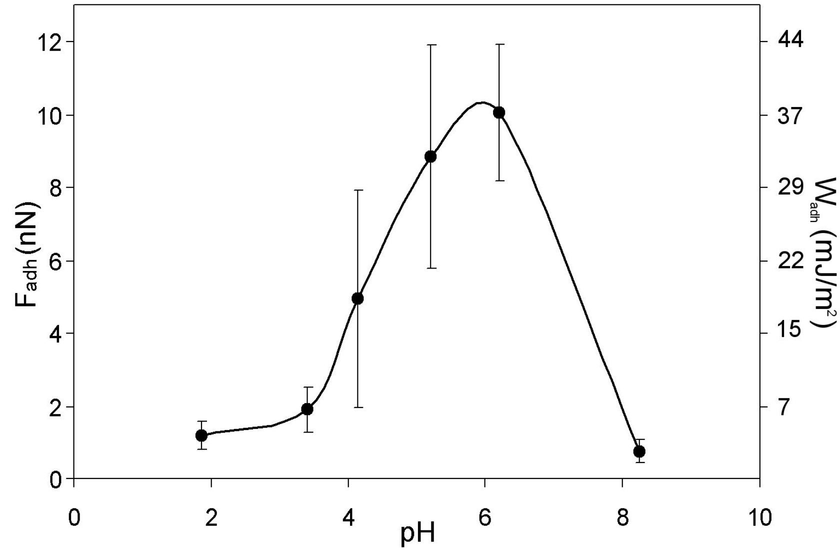

Figure 2.2 A plot of the mean F_{adh} and W_{adh} vs. pH for muscovite mica employing an oxidized Si_3N_4 tip with a radius of curvature of 58 ± 6 nm. Each data point corresponds to the average of >180 adhesion measurements.

structure as a function of load to be examined. Forces of adhesion (F_{adh}) measurements were then conducted within the wear trial area and on the surrounding native mica surface. In this manner the native surface served as an internal reference, which eases interpretation of F_{adh} data by circumventing the uncertainties associated with wear trial effects on tip chemistry. The mean work of adhesion (W_{adh}) was estimated from F_{adh} measurements using the Johnson, Kendall and Roberts (JKR)[54] continuum mechanics model (eq. 2.1).

$$F_{adh} = -1.5\pi R W_{adh} \tag{2.1}$$

In order to minimize the error related to tip wear (i.e. in calculating W_{adh} and p_{thresh}) the tip radius of curvature (R) was determined *prior* to, as well as *after*, each individual wear experiment.

2.3 Results and Discussion

To evaluate the tribochemistry of mica surfaces exposed to aqueous environments, we have used atomic force microscopy (AFM) to probe the simultaneous changes in topography, friction and local adhesion at the mica surface under varying pH conditions and varying imaging loads. The mean adhesive force (F_{adh}) and work of adhesion (W_{adh}) vs. pH is shown in Figure 2.2. Here we find that the force of adhesion starts low at pH 2, peaks around pH 6 (nearly six times that at pH 2) and then declines in more alkaline environments. This pH dependence on adhesion is similar to that found for silica surfaces under the same conditions with a shift in the peak adhesion from pH 4.5 for silica/silica to pH 6 for the hydroxylated Si_3N_4/mica interaction.[50,51] Based on this adhesion vs. pH profile, we chose to evaluate the details of the friction and topography under varying loads for 3 pH ranges, pH 2-3, pH 5-6 and pH > 8.

At the highest pH conditions (pH ~ 8), the mica surface undergoes rapid wear. Even under low loads, wear scars ~ 2 Å in depth form readily. The threshold pressure for wear at pH 8 was found to be ~ 1.2 GPa. With additional scans (>10) wear scars 10 Å or

Table 2.1 Tribochemical properties of micas (001) crystal plane in solution

Property	Mica wear pH 3	Mica wear pH 5	Mica wear pH 8
p_{thresh}	2.1 (2.25^a)	1.5	1.2
$F_{adh}^{Charged}/F_{adh}^{Native}$	-	0.38 - 0.75^{b,c,d}	-
$F_{f}^{Charged}/F_{f}^{Native}$	-	0.74 – 1^{b,c,d}	-
Charge stability (min.)	≤ 2	> 10	< 10

Table 2.1 Hertz wear threshold pressures (p_{thresh}) for removal of basal SiO_3 and AlO_3 tetrahedral units; $^a p_{thresh}$ of mica determined by Kopta et al.[3] under low vacuum (RH ~ 50%); ^{b}mean force of adhesion and force of friction ratio within the charged (nucleation regime) and native mica surface; ^{c}values correspond to nucleation regime where the surface possesses *repulsive* defects; ^{d}values for the gross wear regime (2.2Å pit formation) are equal to or greater than unity due the introduction of *attractive* defects.

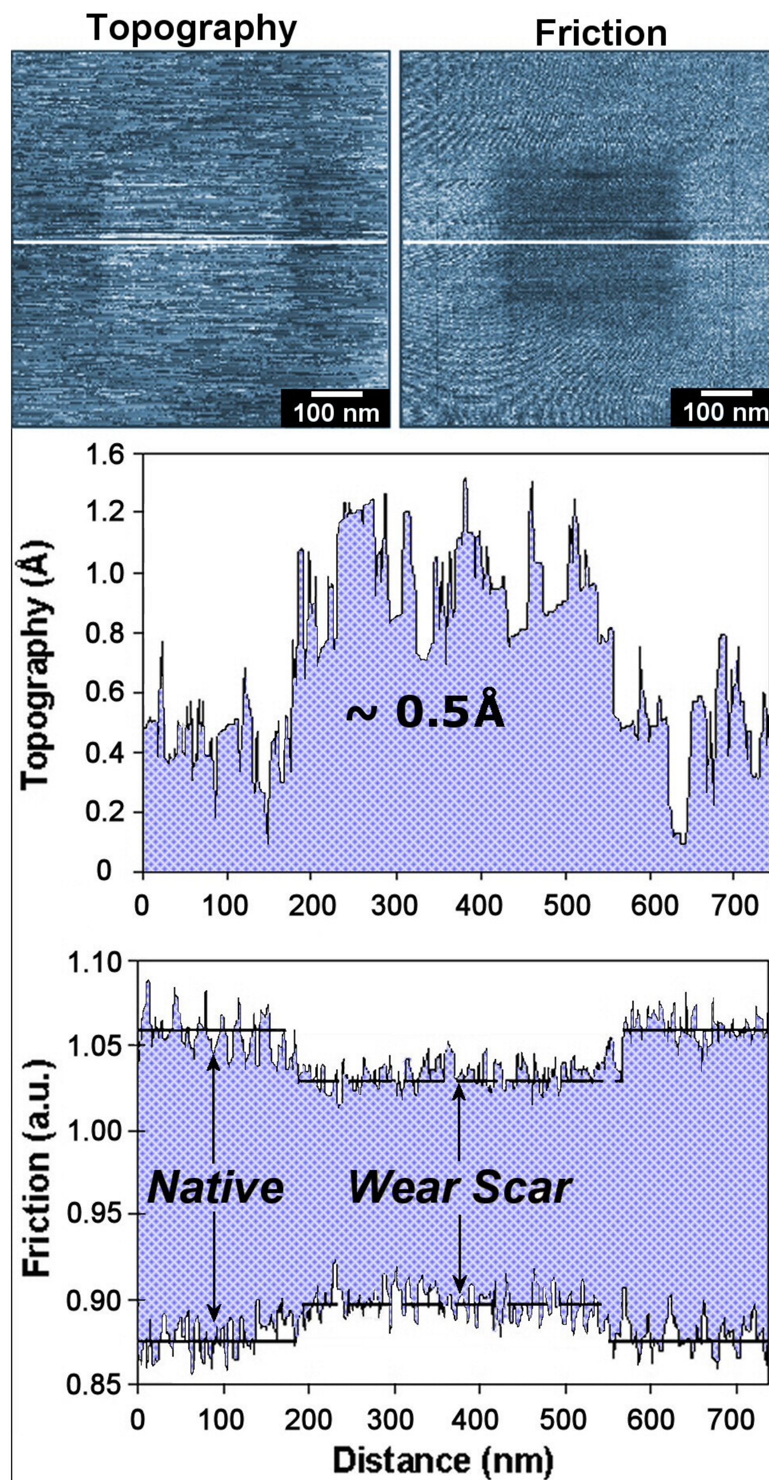

Figure 2.3 Topographic and friction images, 750 nm × 750 nm, of mica's basal plane following defect nucleation induced by scanning over the central 400 nm × 400 nm region at pH 5. Wear trial consisted of 10 scans (100 ms/line or 10 Hz) at a Hertz mean pressure (p_m) of 0.74 GPa. The corresponding topography line trace and friction loop indicate that the outermost surface has expanded slightly by ~ 0.5 ± 0.2 Å and has become negatively charged with respect to the unworn, native mica surface.

more are rapidly formed. Interestingly, the depth of the wear scars formed under these pH conditions is found to scale roughly linearly with the number of scans for wear scars of up to 60 - 70 Å in depth. Upon removal of a 10 Å layer, the friction in the wear scar is found to be equivalent to that of the contiguous unworn mica surface, indicating that wear has progressed from the outermost oxygen terminated basal plane to the next chemically equivalent repeat layer (data not shown). High resolution imaging within the wear scar also confirms this, as the same 5.2 Å hexagonal periodicity of the unworn mica surface is observed. The rapid wearing (relative to trials run in acidic media, Table 2.1) of the mica surface under these conditions is consistent with the more facile chemical dissolution of oxides in alkaline solution conditions.[42,49,55,56]

Lowering the pH to between 5 - 6 the threshold pressure is found to increase to ~ 1.5 GPa. Imaging with low loads (p_m ~ 0.74 GPa ~ ½ p_{thresh}), the surface friction in the imaged region was observed to *decline* relative to the unworn surface prior to any noticeable wear (topographically) on the nanometer scale (Figure 2.3). An increased repulsion between like charges on the tip and surface, as compared to the unworn region, would account for the observed friction decline indicating an increased population of surface anions, presumably siloxy ($Si\text{-}O^-$) groups,[45,57] within the defective mica framework as well as on the tip. Thus, we attribute this decrease to the accumulation of negative surface charge both on the tip and on the imaged surface through OH^- insertion into the Al-O-Si and Si-O-Si bonds, which is facilitated by the scanning of the tip over the sample under load. The load acts to stress surface bonds, reducing the barrier for OH^- insertion. Interestingly, the larger scale surface topography of the "worn" region was also observed to change slightly, with an *increase* in topography by ~ 0.5 Å, which is

near the noise limit of ± 0.3 Å (Figure 2.3). This increase in surface topography would be consistent with the ultimate hydroxylation of the surface as OH^- and H^+ cap the resulting surface dangling bonds as they break open. Thus, while little change in topography is observed on the large scale, clear frictional contrast is present, and is found to be lower than that of the unworn region. Adhesion measurements, as summarized in Table 2.1, within the native and worn ("induced") region show a marked shift to lower adhesive forces for the worn surface, which is expected for the proposed repulsive tip-sample interaction.

Under pH 5 – 6 imaging conditions, the resulting load induced resident surface charges exhibited a temporal stability between ~ 10 – 45 minutes (with contrast in the F_f images gradually fading to undetectable limits) depending on the number of subsequent scans. This persistence provided ample time to obtain the force of adhesion (F_{adh}) measurements with AFM force-distance spectroscopy. Inspection of the F_{adh} for these charged regions, even those with minute frictional contrast such as in Figure 2.4, indicates that the decrease in friction is associated with a concomitant decrease in the work of adhesion (W_{adh}) by ~ half relative to the unworn mica surface (Figure 2.4). Again this can most likely be attributed to a local increase in the population of negative charges acting between the tip and surface within the wear trial area. Thus, in comparison to the native mica surface, as the surface bonds are broken open, defect nucleation results in charging of the surfaces, contributing an additional repulsive component to the tip-sample contact, effectively reducing the adhesive and frictional forces.

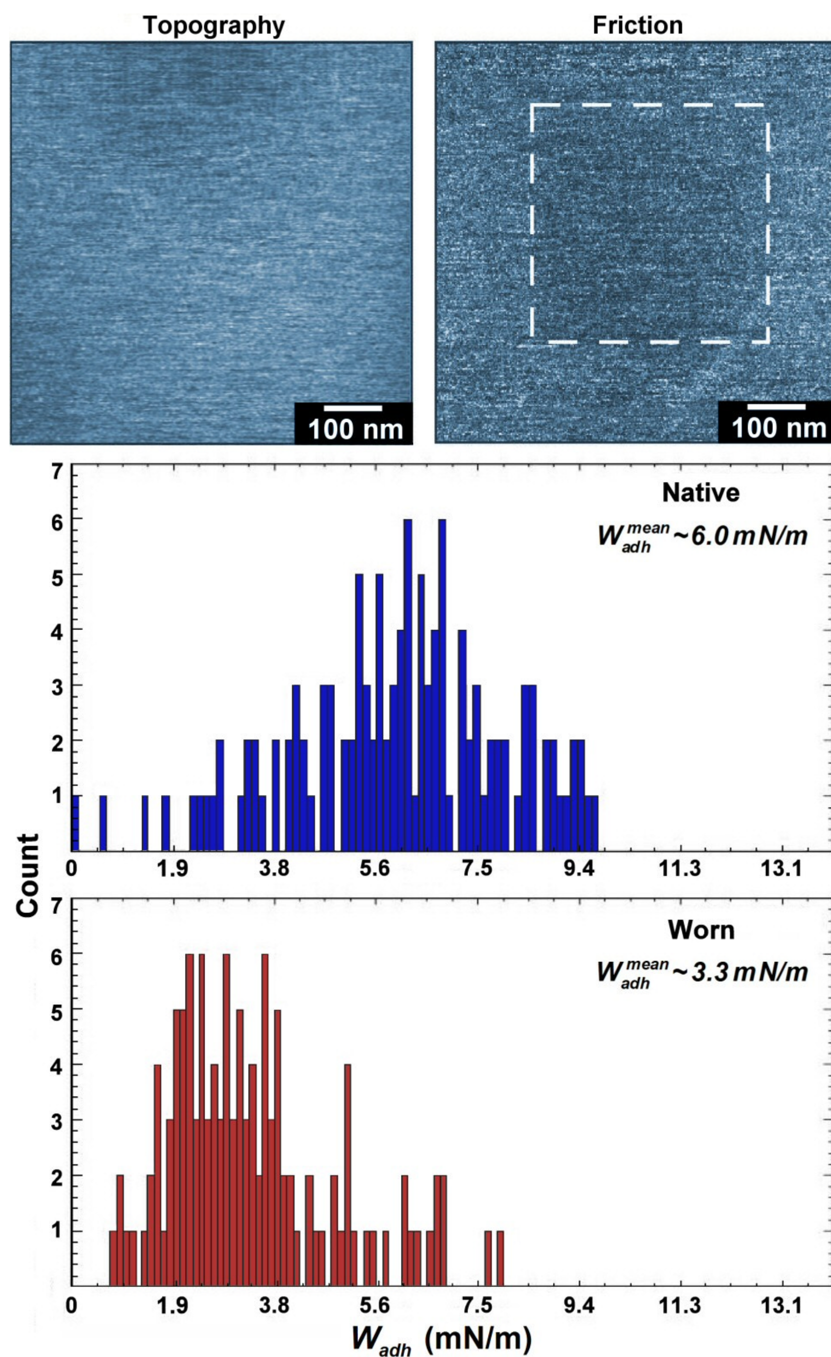

Figure 2.4 Distribution of work of adhesion (W_{adh}) measurements for mica's surface after 10 scans over a 400 nm × 400 nm area (indicated by the outline) at pH 5 and a p_m of 0.61 GPa. The 120 F_{adh} measurements were taken within the *worn* (charged) and *unworn* (native) mica surfaces. The clear shift in the W_{adh} distribution to lower adhesive forces within the wear trial area, relative to native mica, is consistent with creation of (-) charged surface species. The accompanying 700 nm × 700 nm post wear frictional force image exhibits poor contrast between the worn (indicated by the outline) and unworn surfaces illustrating the higher sensitivity of FD spectroscopy over frictional force imaging to local, *low density* chemical changes. Topography shows no discernible changes in surface structure from the wear trial (z-scale 0.75Å).

Some general considerations implicit in Figure 2.4 are worthy to note. First, a pronounced variation in tip chemistry is evident when one compares the W_{adh} for the *native mica/post wear tip* contact (~ 6 mN/m in Figure 2.4) to the *native mica/native-hydroxylated tip* contact (~ 33 mN/m in Figure 2.1). This effect can not be attributed to large changes in tip curvature or "shape" since the nominally parabolic AFM tips were characterized *pre* and *post* each individual wear experiment.[58] Typically (at least for trials in acidic solution below the threshold pressure for gross wear) the post wear radius of curvature measured to within ca. ± 10% of the initial (pre-wear) *R* value. This clearly illustrates that although the tip dimension has not changed, the chemistry most certainly

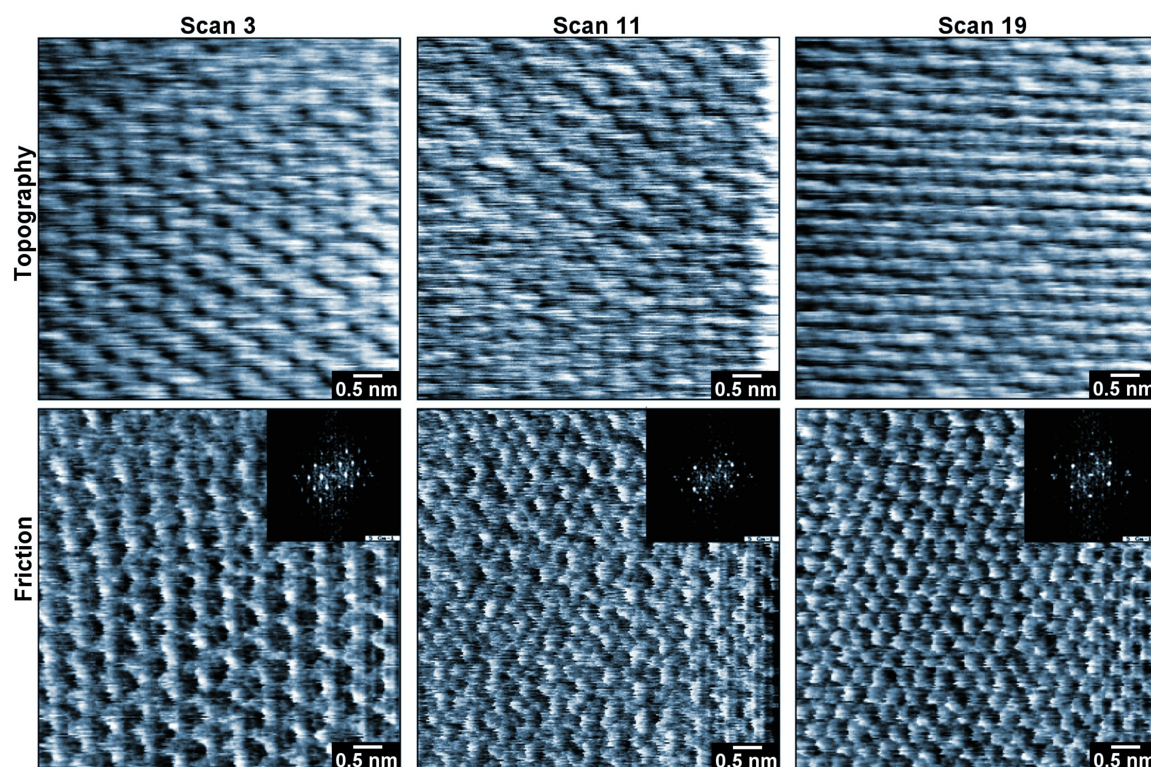

Figure 2.5 Topography (z-scale 1.25Å) and F_f images monitoring the tribochemical surface reconstruction of the native mica lattice from a 5.2Å (scan 3) to a ~3Å (scan 19) periodicity under the local stress of an AFM tip. Images are of the 3rd, 11th and 19th scans during continuous scanning at a rate of 33 Hz over a (7×7) nm^2 region at pH 5 and an applied load of 9 nN (p_m ~ 1.25 GPa). The 2D FFT insert of the F_f micrographs illustrates the lattice transition where the intermediate state (11th scan) possesses a mixed 3Å and 5.2Å periodicity.

has been altered. Secondly, Figure 2.4 also makes it apparent that frictional force (F_f) measurements are less responsive than F_{adh} measurements to the subtle changes in surface chemistry, which in this instance is ascribed to a small population of defects. The large differences in *lateral* versus *normal* cantilever spring constants (~ 100 times stiffer laterally) is responsible for the sensitivity limitations of F_f imaging.[59] Thus, AFM F_{adh} measurements are more sensitive to local chemical changes than its lateral force counterpart.

After the formation of charged regions on the surface, lattice resolution images of the region indicate that although no wear scar has been formed, the surface periodicity is transforming from the native 5.2 Å periodicity of the unworn surface to a mixture of ~ 3 Å and 5.2 Å regions (as illustrated in scan 11 of Figure 2.5). With repeated scanning, the surface is found to ultimately transform completely to a surface with a ~ 3 Å periodicity. The lattice reconstruction can be readily followed by sequential scanning of a 7 nm × 7 nm region (Figure 2.5) at loads of ~ 9 nN (p_m ~ 1.25 GPa ~ 0.75× p_{thresh}). A benefit of this *in situ* reconstruction/imaging is the ability to observe the transition, where a mixed population of the two discrete surface states, i.e. native and nucleated defects (scan 11), are detectable. Such information may find applications in calculating the kinetic parameters of such tip assisted tribochemical processes when conducted in conjunction with the contact-radius line step (*CRLS*) analysis described in Chapter 3.

The lattice resolved reconstruction suggests that the change in the observed structure at the outermost surface is due to the scission of the surface Si-O-Si and Al-O-Si bonds, along with the concomitant insertion of OH^- and H^+ to terminate the cleaved surface bonds. Thus, by controlling the water environment pH we have been able to

directly observe the first stage of mica wear, defect formation as the outermost surface bonds have been ruptured, ultimately changing the observed lattice structure *prior to any gross wear of the surface*. Defect nucleation occurs when the load is below the critical threshold for breakdown of the layer (abstraction of terminal surface species). Here we note that this is clearly a direct observation of a tribochemical reaction. Although hydroxide insertion is thermodynamically favorable for Si-O-Si bonds, it is the added scanning of the surface that assists in driving this reaction along, allowing conversion from the 5.2 Å to a 3 Å surface periodicity. Simply having the surface in this solution alone does not result in the complete transformation of any specific region. It is the additional bond strain imparted to the surface by the contact, which facilitates this transition locally, thus *mechanically* catalyzing the reaction.

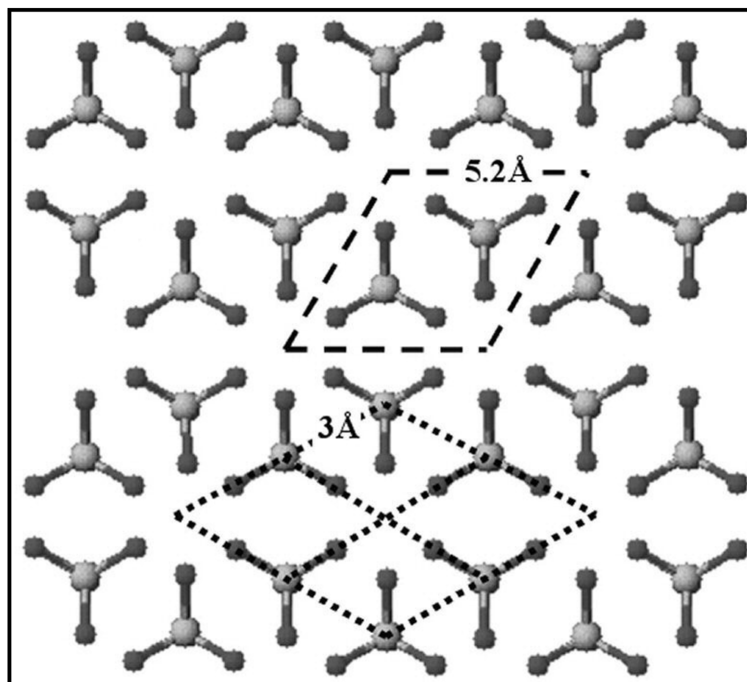

Figure 2.6 Proposed geometric description of the ~ 0.3 nm periodicity observed for micas tribochemical lattice reconstruction. All terminal oxygen bridges of the Si/Al tetrahedra (light central sphere) are broken and surface dangling bonds are shown capped with hydroxyl (only oxygen atoms are shown; dark spheres).

The appearance of the ~ 3 Å reconstructed periodicity is intriguing, however, since contact mode AFM only provides lattice resolution it is difficult to assign the origin of this corrugation. As a starting point, we propose a simple geometric argument to rationalize these observations. If, as a limiting case, we assume that *all* terminal surface bonds are ultimately cleaved and the resulting dangling bonds are capped, steric constraints may promote defect inversion[45] or rotation about the apical Si-O bond yielding a hydrogen bonded six member ring. Figure 2.6 is a graphical rendering of this limiting case with the hydroxyl nests (six member ring) evident at the lattice vertices. It is apparent, however, that such a rearrangement leads to a vicinal oxygen distance between neighboring M-O moieties of only ~ 1.6 Å, which depending on termination, can also introduce lattice strain obviating this simple description. Considering the "defective" lattice persists even under the stresses imposed by the AFM tip during *in situ* monitoring of the reconstruction, it appears that an additional mechanism is deterring complete destruction of the basal surface. There are a number of interesting corollaries to other work on high silica zeolites,[57] silica,[60] cristobalite[44] and kaolinite[61] that lend support to our current interpretation of the reconstruction, i.e. hydrogen bonding is contributing significantly to the stability of the reconstructed surface.[61] For instance, Koller et al. have examined the siloxy-silanol ($SiO^{-}\cdots HOSi$) defect interaction in high silica zeolites and found that six member rings are able to form stable conformations with multiple defects.[57] A hydrogen bonded network[61] (undoubtedly present in the reconstructed lattice) could provide this stability,[45,57] as well as position the reconstructed lattice for "self healing" where the surface defects re-condense.[60] Attempts to observe this reversion *in situ* have been pursued, however unequivocal evidence of this healing process has not

yet been realized. Recently, Pelmenschikov et al. have theoretically explored the energetics of self-healing (condensation of silanol defects)[60] within β-cristobalite as well as the penalties associated with hydrolyzing siloxane bridges within this crystals (111) and (001) crystal planes.[44] AFM investigations of this system may provide direct evidence for this proposal, however we have yet to undertake such an investigation and will be the subject of further study.

When the load is increased above the threshold pressure of ~ 1.5 GPa, wear scars ~ 2 Å in depth are observed (Figure 2.7), which corresponds to removal of the outermost SiO_3/AlO_3 tetrahedral layer. Once the MO_3 (M = Si or Al) basal fragments are removed, the underlying aluminate (Gibbsite) layer is exposed and in aqueous solution carries a net positive charge for pH ≤ 10.[62,63] This is another "model" property of mica as it provides a chemically amplified signal for detection of the onset of the gross wear regime. Considering that the AFM tip at this pH should carry a net negative charge, we would expect an additional coulombic attraction between the AFM tip and the worn region of the surface. This is indeed observed and presents itself as a clear increase in friction, Figure 2.7, in the wear region relative to the native mica surface. By controlling the degree of wear under these pH conditions, we can take advantage of the differing degrees of wear to selectively generate negatively (*defect nucleation*) and positively (*abstraction*) charged regions on mica surfaces. As mica is a frequently employed substrate for adsorption of a number of molecular systems, charge patterning may have applications in several areas, including the formation of controlled nanostructures on mica templates as well as providing a means for modifying protein adsorption on mica surfaces, whose adsorption properties are typically charge sensitive.[64-67] The oxygen terminated surface of

the octahedral Al^{3+} layer is, however, somewhat unstable under these pH conditions and high quality lattice resolution images of this surface were not readily obtained as continued imaging leads to rapid deterioration of the surface forming holes of ~ 10 Å in depth. As with the pH 8 studies, the 10 Å deep wear scar possesses the same friction signal as the contiguous native mica surface.

Under the lowest pH conditions (pH < 3), wear of the surface does not occur with the same load and scan conditions as at the higher pH's even though the surface is still immersed in water. In fact, the surface shows no wear under *identical loads* with over 8 times the number of scans required for wear a pH 5 - 6 (Figure 2.8). Clearly this is due to insufficient amounts of OH^- in the water to catalyze the Si-O-Si or Al-O-Si bond scission needed to initiate wear. This pronounced increase in stability, even while immersed in water, can be attributed to the significantly lower base catalyzed activation barrier, which is 2 - 3 times smaller than the H^+ mediated pathway (Table 2.2).[43,44,68,69]

Table 2.2 - Threshold pressures for mica wear under solution conditions, and *ab initio* calculated activation energies (E_a) for various catalytic hydrolysis pathways

Conditions	p_{thresh} [1]	**Hydrolysis activation energy (E_a)**
Mica wear pH 3	2.1 GPa	-
Mica wear pH 5	1.5 GPa	-
Mica wear pH 8	1.2 GPa	-
Si−O−Si {OH^- catalyzed}	-	2-8 kcal/mol [68]
Si−O−Al {H^+ catalyzed}	-	16 kcal/mol [43]
Si−O−Si {H^+ catalyzed}	-	24 kcal/mol [43]
Si−O−Al {H_2O catalyzed}	-	26 kcal/mol [43]
Si−O−Si {H_2O catalyzed}	-	29 kcal/mol [43,69]

Table 2.2 Threshold pressures (p_{thresh}) were calculated with Hertz continuum mechanics theory. p_{thresh} corresponds to the gross deformation (abstraction) regime that is defined by removal of SiO_3 and AlO_3 basal tetrahedral units.

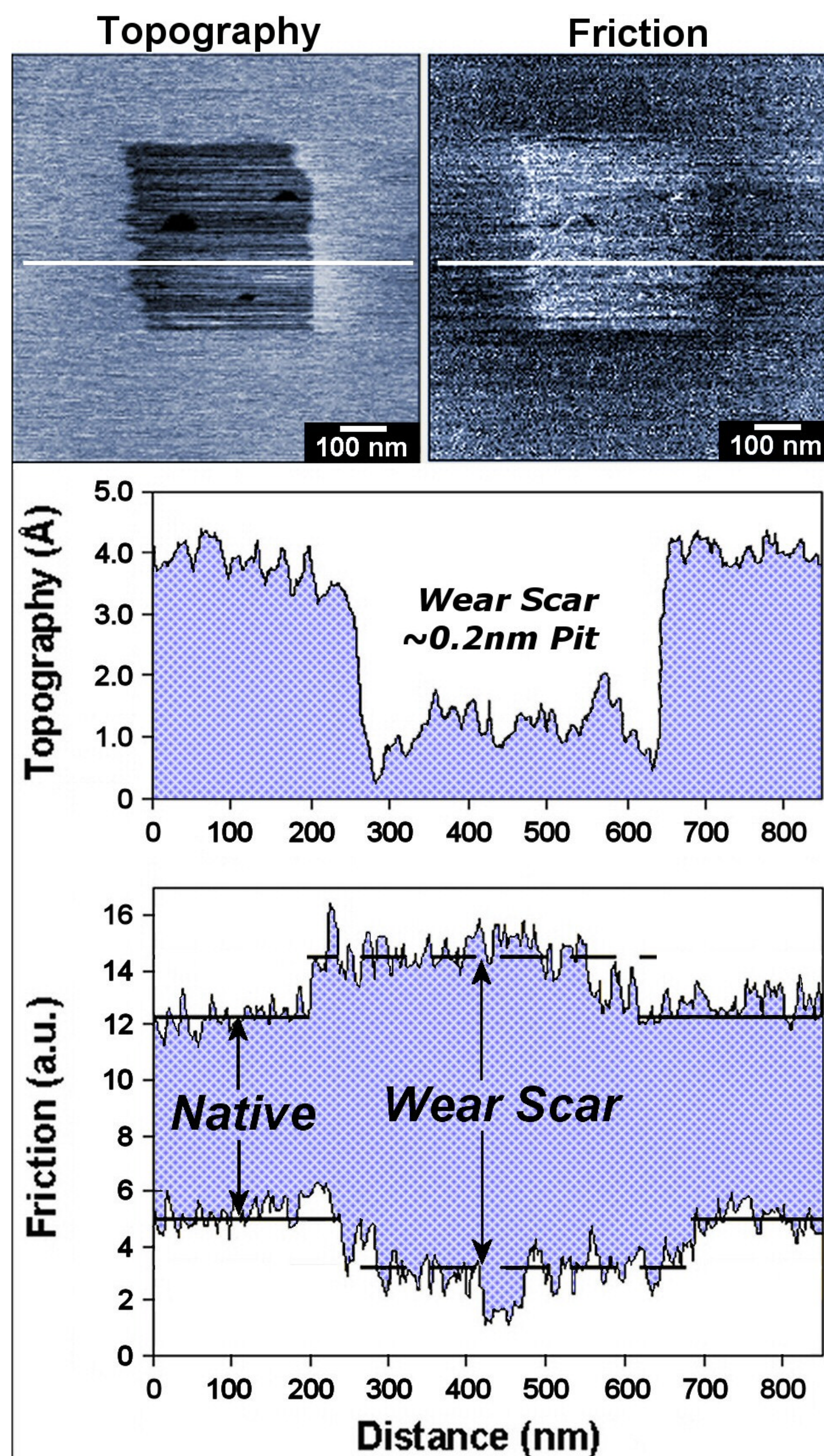

Figure 2.7 Topography and frictional force images, 870 nm × 870 nm, following abstraction of the basal planes terminating molecular fragments under pH 5 conditions at a p_m of 1.67 GPa for 10 scans (at 10 Hz). The corresponding friction loop indicates that the worn surface has become positively charged, effectively increasing the local friction relative to the unworn mica. The worn area is depressed by the depth of the $Al-O_3/Si-O_3$ fragment of the $Al-O_4/Si-O_4$ tetrahedral unit (~ 0.22 nm) and exposes the sequential alumina layer that carries a net positive charge at this pH.[44,45]

Comparison of the threshold forces for removal of the SiO_3/AlO_3 tetrahedral layer, i.e. generating 0.22 nm wear scars, under the three pH ranges illustrates the tribochemical influence hydroxide ions have on hydrolysis of surface bonds. Table 2.2 summarizes the threshold pressures and the *ab initio* calculated activation energies (E_a) for water, acid and base catalyzed Si-O-M hydrolysis.[43,68] For the pH 3 studies, we find that only after the load is increased to 23 nN ($p_m \sim 2.1$ GPa) is any noticeable wear observed (in the limit of 10 scans). Interestingly the threshold force previously determined by Salmeron and co-workers of ~ 70 – 80 nN ($p_m \sim 2.25$ GPa) is consistent with the range our findings in acidic solutions .[3] With sufficiently high loads, as with pH 5 - 8, surface charging is also observed at pH 3, however, this condition is much less stable at pH 3, relative to pH 5, with discernible friction contrast lasting only a few minutes. This rapid disappearance is likely attributed to the increased H^+ concentration available for charge capping. The characteristics of surface wear as a function of pH suggest that load (i.e. the local stress field) plays a more significant role in the conditions where the OH^- concentrations are the lowest, due to the necessity to strain the bridging oxygen bonds more and induce cleavage in the absence of OH^- to facilitate bond scission. The critical load for this transition should therefore be readily linked with the minimum stress needed to facilitate bond scission in the presence of a particular [OH^-].

2.4 Insights Into the Atomic Scale Wear Behavior Of Crystal Surfaces

There have been many theoretical and experimental studies on wear of oxides and the generation and propagation of defects within condensed matter. Here a few examples of crystalline systems within the context of tip induced defect nucleation and wear are

described. The examples will focus on studies of defect nucleation that have revealed the prototypical behavior of what is to be expected (and what is detectable with AFM) of a surface reconstructing under the influence of an AFM tip. At the most fundamental level of defect nucleation, this includes *terminal* surface bond rupture for covalent systems as well as removal of ions from ionic surfaces. Although not a common observation, several groups have reported surface charging with little to no topography changes during wear experiments. Using the nanoscale Kelvin probe, capable of measuring variations in surface potential (work function mapping), Bhushan and DeVecchio have observed electron deficient regions within the "zero wear" regime for single crystal aluminum under ambient conditions (RH 45 % ± 5 %).[7] Their potential maps clearly illustrate the charging effect prior to catastrophic failure of the surface, however, the appearance of a minute square raster pattern in the topography image indicates that they are not likely in the atomic, defect nucleation regime but are in the early stages of gross wear.[7]

A very interesting account of the atomic scale, defect nucleation regime was observed by Carpick et al. while studying the frictional properties of halide crystals (KF, KCl and KBr) in UHV. Upon imaging these surfaces, the evolution of "mysterious" high friction regions occurred for all crystal surfaces. An interesting characteristic of the halide systems is that for KBr the increased friction was not accompanied with a change in topography, however, topographic contrast on the order of 0.2 nm was found to simultaneously occur for the KF crystal. For comparison, Table 2.3 provides a summary of the tribological properties of mica and these halide crystals. It is believed that "defects" are triggered by the AFM contact, however it is not clear why localization of the high friction regions occurs and why the high and low friction regions have nearly

identical adhesive forces; the latter is quite a peculiar finding and worthy of attention. Further experimental work is needed to address the questions this work raises and will be invaluable in the effort towards bridging simulation and experiment.[70-72]

For mica, under pH 5 – 6 imaging conditions, the tip induced surface charges have a temporal stability between 10 – 45 minutes, and yield a reduction in both the frictional force and force of adhesion, which is again relative to the native, unworn surface. Lattice resolved images within such charged regions, even areas with negligible topographic and friction contrast, portray a transforming mica lattice with the two, native 5.2 Å and reconstructing 3 Å, lattice constants. As demonstrated in Figure 2.5, this transition can be monitored *in situ* by scanning at a load ~ 75% of the threshold force for SiO_3/AlO_3 abstraction. The progression from the 0.52 nm to the 0.3 nm periodicity provides for the first time, explicit evidence, as well as, a characteristic structure of the metastable "nucleation" wear regime.

Table 2.3 - Tribological properties of mica and halide crystals within Defect Nucleation Regime

Sample	Anion Radius (nm)	Native Lattice (nm)	Reconstructed Periodicity (nm)	Nucleation Height (nm)	$F_{adh}^{Induced}/F_{adh}^{Native}$	$F_f^{Induced}/F_f^{Native}$
Mica[†]	-	0.52[a]	0.3	≤0.05± 0.03	0.38 – 0.75[b]	0.74 – 1[b]
KF[‡]	0.136	0.378	-	0.2 ± 0.03	0.98	2.3
KCl[‡]	0.181	0.445	-	0.04 ± 0.02	0.93	1.79
KBr[‡]	0.195	0.467	-	< 0.02	0.94	1.24

Table 2.3 [†]From refs. 1 and 2 with topography, friction and adhesion data corresponding to the defect nucleation regime; [‡]From ref. 4; [a]For micas(001) crystal plane; $F_{adh}^{Induced}/F_{adh}^{Native}$ is the ratio of force of adhesion measurements within the wear induced region to the native surface; $F_f^{Induced}/F_f^{Native}$ is the force of friction ratio of measurements within the wear induced region to the native surface; [b]Depends strongly on pH and the extent of surface charging.

A brief comparison of mica wear[1-3,19] to the tip induced dissolution of calcite is instructive, since there are distinct differences between these two systems. Dickinson, Langford, Kim, Park, Hariadi and Scudiero[10-12,73] have elegantly explored calcite and brushite dissolution in supersaturated solutions with AFM. They have found strong correlations between theoretical and experimentally determined activated volumes and realistic activation energies using a relatively straightforward model. Application of a similar model to mica has had some difficulties with agreement between empirically fitted material constants and their "known" values.[3] There is a fundamental difference between mica and calcite that may be limiting the model's success when applied to mica. The basal mica plane is a covalent network of bridging oxygen bonds, which require scission in order for defect nucleation to occur. On the other hand the nucleating stage for calcite (an ionic crystal) involves the displacement of individual surface ions into solution (separating ion pairs). As demonstrated by Dickinson, calcite wear does not exhibit a critical load where dissolution suddenly begins. This is in stark contrast to mica, where in UHV and under solution conditions, a critical threshold pressure is observed, thus indicating that mechanical stress accounts for a significant portion of the energy required to cleave the surface bonds, and comparisons between the two systems should be conducted with caution, especially relating to adaptation of models.

2.5 Summary and Conclusions

Using AFM we have been able to directly observe defect nucleation in the form of surface charging and surface restructuring of the oxygen terminated mica surface prior to the formation of visible wear scars. This indicates that under aqueous environments extensive scission of bridging Si-O-Si and Al-O-Si bonds occurs, yielding anionic (e.g.

SiO^-) and hydroxyl (Si-OH and Al-OH) terminated surfaces, pre-empting wear scar formation. The transformation is explicitly observed with a 5.2 Å to ~ 3 Å lattice reconstruction. The role of hydroxide in the stimulation of mica wear is clearly demonstrated and is typified by observations under acidic conditions (pH 3) where surface degradation is inhibited until loads of ca. 23 nN (p_m ~ 2.1 GPa). Surprisingly the onset of wear in pH 3 aqueous solution appears at approximately the same load conditions required to initiate wear when only a single monolayer of water is present at the surface.[3] The threshold pressure for wear decreases with increasing pH, illustrating the interplay of hydroxide ion concentration and the activation barrier for catalytic wear of mica surfaces. The ability to pattern regions of varying surface charge via controlled load and scan conditions also represents a new way to carry out nanoscale surface structure design and templating, which may be useful for the site specific binding of proteins or other charged molecules (e.g. organic dyes)[74-76] on a surface without the need for surface functionalization.

Appendix 2.1 - Contact Radius and Pressure Calculation

The Hertz contact radius (a) is given as a function of the tip radius of curvature (R), the normal force (F_z) and the combined tip-sample elastic modulus (ε).[52,53]

$$a = \left(\frac{3RF_z}{4\varepsilon} \right)^{1/3} \text{ with } \varepsilon = \left(\frac{1-\nu_1^2}{E_1} + \frac{1-\nu_2^2}{E_2} \right)^{-1} .$$

The individual Poisson ratios (ν_i) and Young's moduli (E_i) for mica and a Si tip are (ν_1 = 0.1 and E_1 = 56.5 GPa) and (ν_2 = 0.3 and E_2 = 155 GPa) respectively.[3] With an R of 35 nm and a load of 400 nN the Hertz contact radius is 5.7 nm. For our work with a Si_3N_4 tip, ν_2 = 0.24 and E_2 = 220 GPa.[77] The Hertz contact radius and normal load are then utilized to estimate the Hertz mean pressure ($p_m = F_z/\pi a^2$).

Chapter 2 References -

(1) Helt, J. M.; Batteas, J. D. *Langmuir* **2005**, *21*, 633.

(2) Helt, J. M.; Batteas, J. D. *J. Chem. Phys.*, *to be submitted*.

(3) Kopta, S.; Salmeron, M. *J. Chem. Phys.* **2000**, *113*, 8249.

(4) Carpick, R. W.; Dai, Q.; Ogletree, D. F.; Salmeron, M. *Tribol. Lett.* **1998**, *5*, 91.

(5) *Modern Tribology Handbook*; 1st ed.; Bhushan, B., Ed.; CRC Press: Boca Raton, 2001; Vol. 1, pp 1460.

(6) Carpick, R. W.; Salmeron, M. *Chem. Rev.* **1997**, *97*, 1163.

(7) DeVecchio, D.; Bhushan, B. *Rev. Sci. Instrum.* **1998**, *69*, 3618.

(8) Prioli, R.; Reigada, D. C.; Freire, F. L. *Appl. Phys. Lett.* **1999**, *75*, 1317.

(9) Prioli, R.; Reigada, D. C.; Freire, F. L. *J. Appl. Phys.* **2000**, *87*, 1118.

(10) Park, N. S.; Kim, M. W.; Langford, S. C.; Dickinson, J. T. *J. Appl. Phys.* **1996**, *80*, 2680.

(11) Park, N. S.; Kim, M. W.; Langford, S. C.; Dickinson, J. T. *Langmuir* **1996**, *12*, 4599.

(12) Dickinson, J. T.; Hariadi, R. F.; Langford, S. C. *Ceram. Trans.* **1999**, *102*, 213.

(13) Erlandsson, R.; Hadziioannou, G.; Mate, C. M.; McClelland, G. M.; Chiang, S. *J. Chem. Phys.* **1988**, *89*, 5190.

(14) Carpick, R. W.; Agrait, N.; Ogletree, D. F.; Salmeron, M. *J. Vac. Sci. Technol., B* **1996**, *14*, 1289.

(15) Salmeron, M. *Tribol. Lett.* **2001**, *10*, 69.

(16) Carpick, R. W.; Agrait, N.; Ogletree, D. F.; Salmeron, M. *Langmuir* **1996**, *12*, 3334.

(17) Carpick, R. W.; Enachescu, M.; Ogletree, D. F.; Salmeron, M. *Mat. Res. Soc. Symp. Proc.* **1999**, *539*, 93.

(18) Demirel, A. L.; Granick, S. *J. Chem. Phys.* **1998**, *109*, 6889.

(19) Hu, J.; Xiao, X. D.; Ogletree, D. F.; Salmeron, M. *Surf. Sci.* **1995**, *327*, 358.

(20) Piner, R. D.; Mirkin, C. A. *Langmuir* **1997**, *13*, 6864.

(21) Xu, L.; Salmeron, M. *Langmuir* **1998**, *14*, 2187.

(22) Tsujimichi, K.; Tamura, H.; Hirotani, A.; Kubo, M.; Komiyama, M.; Miyamoto, A. *J. Phys. Chem., Part B* **1997**, *101*, 4260.

(23) Wei, Z. Q.; Wang, C.; Bai, C. L. *Langmuir* **2001**, *17*, 3945.

(24) Eastman, T.; Zhu, D. M. *Langmuir* **1996**, *12*, 2859.

(25) Knarr, R. F.; Quon, R. A.; Vanderlick, T. K. *Langmuir* **1998**, *14*, 6414.

(26) Teschke, O.; de Souza, E. F. *Appl. Phys. Lett.* **1999**, *74*, 1755.

(27) Teschke, O.; Ceotto, G.; de Souza, E. F. *Phys. Chem. Chem. Phys.* **2001**, *3*, 3761.

(28) Barthel, E.; Roux, S. *Langmuir* **2000**, *16*, 8134.

(29) Vakarelski, I. U.; Ishimura, K.; Higashitani, K. *J. Colloid Interface Sci.* **2000**, *227*, 111.

(30) Raviv, U.; Laurat, P.; Klein, J. *J. Chem. Phys.* **2002**, *116*, 5167.

(31) Miyake, S. *Appl. Phys. Lett.* **1994**, *65*, 980.

(32) Binnig, G.; Quate, C. F.; Gerber, C. *Phys. Rev. Lett.* **1986**, *56*, 930.

(33) Israelachvili, J. N. *Intermolecular and Surfaces Forces*, 2nd ed.; Academic Press: New York, 1992.

(34) Frantz, P.; Artsyukhovich, A.; Carpick, R. W.; Salmeron, M. *Langmuir* **1997**, *13*, 5957.

(35) Yoshizawa, H.; Israelachvili, J. *J. Phys. Chem.* **1993**, *97*, 11300.

(36) Yoshizawa, H.; Chen, Y. L.; Israelachvili, J. *J. Phys. Chem.* **1993**, *97*, 4128.

(37) Pashley, R. M.; Israelachvili, J. N. *J. Colloid Interface Sci.* **1984**, *101*, 511.

(38) Bailey, S. W. *Rev. Mineral.* **1984**, *13*, 1.

(39) Xu, L.; Lio, A.; Hu, J.; Ogleterre, D. F.; Salmeron, M. *J. Phys. Chem., Part B* **1998**, *102*, 540.

(40) Gunko, V. M.; Turov, V. V.; Zarko, V. I.; Voronin, E. F.; Tischenko, V. A.; Dudnik, V. V.; Pakhlov, E. M.; Chuiko, A. A. *Langmuir* **1997**, *13*, 1529.

(41) Fischer, T. E.; Mullins, W. M. *J. Phys. Chem.* **1992**, *96*, 5690.

(42) Xiao, Y. T.; Lasaga, A. C. *Geochim. Cosmochim. Acta* **1996**, *60*, 2283.

(43) Xiao, Y. T.; Lasaga, A. C. *Geochim. Cosmochim. Acta* **1994**, *58*, 5379.

(44) Pelmenschikov, A.; Strandh, H.; Pettersson, L. G. M.; Leszczynski, J. *J. Phys. Chem., Part B* **2000**, *104*, 5779.

(45) Sokol, A. A.; Catlow, C. R. A.; Garces, J. M.; Kuperman, A. *J. Phys. Chem., Part B* **2002**, *106*, 6163.

(46) Tortonese, M.; Kirk, M. *SPIE Proc. - Micromach. Imag.* **1997**, *3009*, 53.

(47) Sheiko, S. S.; Moller, M.; Reuvekamp, E. M. C. M.; Zandbergen, H. W. *Phys. Rev. B: Condens. Matter* **1993**, *48*, 5675.

(48) Bousse, L.; Mostarshed, S. *J Electroanal Chem* **1991**, *302*, 269.

(49) Iler, R. K. *The Chemistry of Silica*; Wiley- Interscience: New York, 1979.

(50) Marti, A.; Hahner, G.; Spencer, N. D. *Langmuir* **1995**, *11*, 4632.

(51) Batteas, J. D.; Quan, X. H.; Weldon, M. K. *Tribol. Lett.* **1999**, *7*, 121.

(52) Hertz, H. *J. Reine Angew. Math.* **1881**, *92*, 156.

(53) Johnson, K. L. *Contact Mechanics*; Cambridge University Press: Cambridge, 1987.

(54) Cicerone, M. T.; Blackburn, F. R.; Ediger, M. D. *Macromolecules* **1995**, *28*, 8224.

(55) Xu, H.; Van Deventer, J. S. J. *Comput. Chem.* **2000**, *24*, 391.

(56) Brady, P. V.; Walther, J. V. *Geochim. Cosmochim. Acta* **1989**, *53*, 2823.

(57) Koller, H.; Lobo, R. F.; Burkett, S. L.; Davis, M. E. *J. Phys. Chem.* **1995**, *99*, 12588.

(58) Maw, W.; Stevens, F.; Langford, S. C.; Dickinson, J. T. *J. Appl. Phys.* **2002**, *92*, 5103.

(59) Ogletree, D. F.; Carpick, R. W.; Salmeron, M. *Rev. Sci. Instrum.* **1996**, *67*, 3298.

(60) Pelmenschikov, A.; Leszczynski, J.; Pettersson, L. G. M. *J. Phys. Chem., Part A* **2001**, *105*, 9528.

(61) Benco, L.; Tunega, D.; Hafner, J.; Lischka, H. *J. Phys. Chem., Part B* **2001**, *105*, 10812.

(62) Hiemstra, T.; Yong, H.; Van Riemsdijk, W. H. *Langmuir* **1999**, *15*, 5942.

(63) Veeramasuneni, S.; Yalamanchili, M. R.; Miller, J. D. *J. Colloid Interface Sci.* **1996**, *184*, 594.

(64) Billsten, P.; Carlsson, U.; Elwings, H. Studies of the Conformations of Adsorbed Proteins with the use of Nanoparticle Techonology. In *Biopolymers at Interfaces*; 1st ed.; Malmsten, M., Ed.; Marcel Dekker: New York, 1999; Vol. 75; pp 627.

(65) Wadu-Mesthrige, K.; Xu, S.; Amro, N. A.; Liu, G. Y. *Langmuir* **1999**, *15*, 8580.

(66) Holmlin, R. E.; Chen, X. X.; Chapman, R. G.; Takayama, S.; Whitesides, G. M. *Langmuir* **2001**, *17*, 2841.

(67) Deere, J.; Magner, E.; Wall, J. G.; Hodnett, B. K. *J. Phys. Chem., Part B* **2002**, *106*, 7340.

(68) Batteas, J. D.; Weldon, M. K.; Raghavachari, K. Bonding & Inter-Particle Interactions of Silica Nanoparticles: Probing Adhesion at Asperity-Asperity Contacts. In *Nanotribology: Critical Assessment and Research Needs*; Hsu, S. M., Ying, Z. C., Eds.; Kluwer Academic: Boston, 2003; pp 387.

(69) Kubicki, J. D.; Xiao, Y.; Lasaga, A. C. *Geochim. Cosmochim. Acta* **1993**, *57*, 3847.

(70) Shluger, A. L.; Rohl, A. L.; Wilson, R. M.; Williams, R. T. *J. Vac. Sci. Technol., B* **1995**, *13*, 1155.

(71) Loppacher, C.; Bennewitz, R.; Pfeiffer, O.; Guggisberg, M.; Bammerlin, M.; Schar, S.; Barwich, V.; Baratoff, A.; Meyer, E. *Phys. Rev. B: Condens. Matter* **2000**, *62*, 13674.

(72) Gnecco, E.; Bennewitz, R.; Gyalog, T.; Loppacher, C.; Bammerlin, M.; Meyer, E.; Guntherodt, H. J. *Phys. Rev. Lett.* **2000**, *84*, 1172.

(73) Scudiero, L.; Langford, S. C.; Dickinson, J. T. *Tribol. Lett.* **1999**, *6*, 41.

(74) Karthaus, O.; Kawatani, Y. *Jpn. J. Appl. Phys., Part 1* **2003**, *42*, 127.

(75) Xu, W.; Guo, H. Q.; Akins, D. L. *J. Phys. Chem., Part B* **2001**, *105*, 7686.

(76) Ozcelik, S.; Akins, D. L. *Appl. Phys. Lett.* **1997**, *71*, 3057.

(77) Hazel, J. L.; Tsukruk, V. V. *J. Tribol. - Trans. ASME* **1998**, *120*, 814.

Chapter 3.

Scanning Probe Nanotribology
and the Contact Radius – Line Step Relationship

3.1 Introduction

Surface related nanoscale phenomena are inherently complex and difficult to probe owing to the vanishingly small population of species of interest. For instance, the population of defective nuclei within the AFM tip-surface contact is estimated to be on the order of unity and amounts to having the sensitivity to detect a single ruptured bond within a matrix of ca. 120 bonds, or ~ 1%.[1-5] Surface wear phenomena are further complicated by chemical and history dependent dynamics, which continuously alter the dominant energy dissipating mechanisms.[1,2,6,7] The activation and coexistence of various energy relieving pathways, such as abrasion, becomes more problematic once the wear threshold is breached, which further convolutes the various mechanisms at work. The direct evidence needed to unravel the mechanistic details of the tribological processes germane to wearing contacts can be probed with the atomic force microscopes (AFM) various modes of operation.[8-10] AFM is well suited for probing tribochemical wear especially with the advent of force distance (FD) spectroscopy and frictional force (F_f) imaging.[1,2,5,10-26] Quantitative interfacial energies, charge distributions and interfacial tip-mediated reaction kinetics for phenomenally small wear areas (< 10 nm^2) can be measured, capturing surface modification and degradation from an atomistic and molecular point of view.[1,2,5,12-14,27-33] With precise control over the applied load (F_z) and scan rate of a *single* asperity, demarcation of the tribochemical and mechanical/load

dependent wear regimes is attainable.[1,2] Although typical wear rates exceed AFM raster cycles by an order of magnitude or more, the idea is to elucidate wear dynamics through measurement of discrete chemical interactions rather than from purely mesoscopic observations and statistical ensembles. *In situ* nanoscale modification of material properties, through controlled bond rupture and molecular fragment abstraction, offers direct access to a surfaces response to local chemo-mechanical stresses.[1,2,5,12] Such inelastic perturbations can induce both physical and chemical changes to the surface, leading to wear intermediates with physical characteristics that are unique from the bulk and therefore may be performance limiting. Understanding the fundamental surface interactions during and after wear events is therefore necessary and will provide the evidence needed to aid the current effort of wear map modeling for micro/macroscopic bodies; situations with many wear mechanisms operating in concert.

The ability to forecast the breakdown of surfaces in relative motion, facilitates device design and engineering by giving the insight to avoid materials with inferior performance characteristics, as well as, to bring to light the wear mechanisms that may limit a device's operational lifetime. In our earlier nanoscale wear studies, it was found that the capacity to deterministically predict the wear behavior for arbitrary scan areas was not readily achieved.[1,2,6,7] From this work and from work by other groups, it became clearly apparent that a basic element in designing nanoscale AFM studies was not addressed and could provide the experimental rigor needed to improve the accuracy of wear predictions. As with all analytical techniques, experiments must be designed such that we are assured the measurements accurately describe the phenomena being monitored. With respect to AFM wear studies, whether it is a mechanical, corrosive or

tribochemical wear pathway, the native surfaces contact history is revealed as defects within the native crystal lattice or the residing adducts.[6,7] If the recorded scan history is inaccurate then the effort to extract the surface's response, via relationships between the activation parameters of defect nucleation and scan frequency (i.e. number of scans), can be severely impeded. With this in mind, a simple calculation is described that conditions the AFM data set by determining the most appropriate AFM scanning parameters for nanoscale wear trials. Here, the purpose is to avoid inadvertent multiple passes due to overlap of sequential line scans. The prevalence of scan overlap in nanotribology studies is striking and we have found that it can have deleterious affects on frequency (experimental number of scans; N_{scans}^{Exp}) - load dependent studies, and thereby taint the observations and their interpretation.

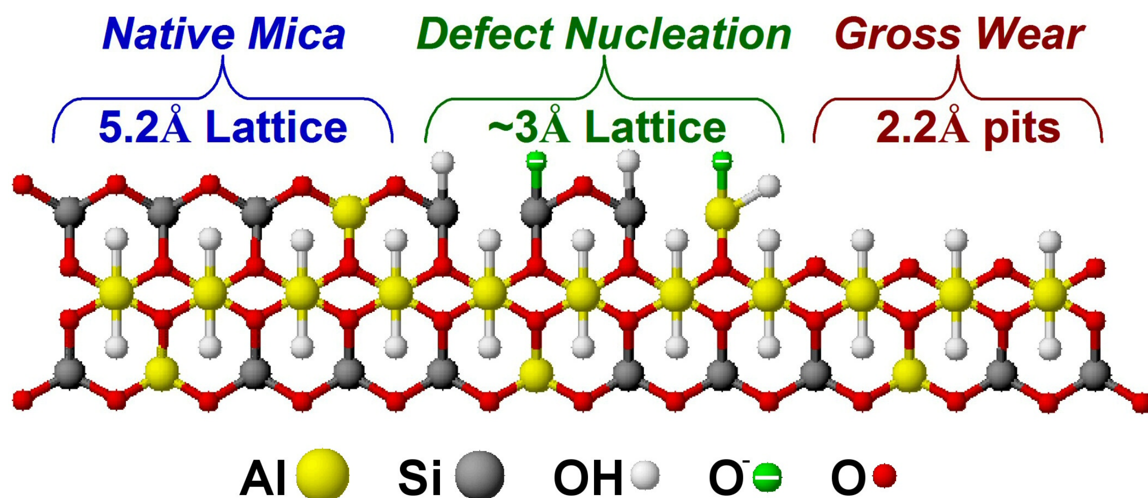

Figure 3.1 Pictorial representation, orthogonal to the (001) plane, illustrating the progressive deterioration of micas basal plane during tribochemical wear processes.[1]

Muscovite mica, a layered alumino-silicate in the form of $KAl_2(Si_3AlO_{10})(OH)_2$, has been a standard for atomic scale investigations due to the ability to readily generate large domains of atomically smooth surface.[1,2,5,10,34] Mica's (001) crystal plane displays a 5.2 Å lattice, Chapter 2 Figure 2.1a, while the alumino-silicate sheets normal to the (001) plane have a periodicity of ~ 10 Å, Figure 2.1b.[3,4,35] These repeating sheets are electrostatically bound by K^+ ions, which act to neutralize the negative charge associated with the partial substitution of Si with Al (1 out of every four). Mica also possesses an octahedral coordinated alumina layer that is 2.2 Å from the surface of the (001) basal plane. The facile cleavage and chemical uniqueness of each mica layer in solution makes mica a model substrate for tribology investigations.[27,28,36] In Chapter 2, we illustrated the progressive wear behavior of mica in solution, which begins with the rupture of terminating surface bonds (defect nucleation) and advances to the gross wear regime and generation of wear scars equal to or greater than 2.2Å. Figure 3.1 provides a graphical representation of this sequence of events. Here, mica is employed to examine the impact of scan overlap on a surfaces contact scan history, using a *contact radius – line step* (*CRLS*) relationship developed with Hertz contact mechanics theory. *CRLS* analysis will be tested by attempting to predict the requisite number of image scans required for experiments devoid of scan overlap to achieve an equivalent degree of surface wear found with "parent" trials possessing overlap. Therefore, by design, all experiments are conducted in pairs; one trial with scan overlap and one without. In this manner, the non-overlapping, *CRLS* derived trial is internally referenced to the "parent" trial (with overlap) fostering comparison and evaluation of the role that scan overlap plays in defect generation and wear as investigated by AFM.

3.2 Analysis Methodology

Development of the *CRLS* analysis first requires a functional form describing the geometry of the tip – surface contact. Although there are several models available, in order to maintain simplicity, the most general form defined by Hertz continuum mechanics is implemented. Here, the contact radius (a) of a spherical AFM tip on a flat elastic body is defined as: [36]

$$a = \left(\frac{3RF_z}{4\varepsilon} \right)^{1/3} \quad \text{with} \quad \varepsilon = \left(\frac{1-v_1^2}{E_1} + \frac{1-v_2^2}{E_2} \right)^{-1}. \qquad (3.1, 3.2)$$

Respectively, R, F_z and ε are the tip radius of curvature, the applied normal force and the combined elastic modulus, with ε given in terms of the individual Poisson ratio (v_i) and Young's modulus (E_i) of the tip and sample.

The second component of this analysis considers the general AFM image acquisition settings, i.e. image resolution *res* (lines scanned per image) and slow scan length L_{sscan}. Although these settings have brought little attention as experimental parameters, the presented analysis indicates that they can predictably impact the tip-surface contact history and can therefore be employed advantageously in nanotribology studies. Specifically, *CRLS* analysis uses the ratio of L_{sscan} and *res*, eq. 3.3, to define the line step (*LS*) or pitch of successive line traces along the slow scan axis. Figure 3.2 illustrates the inverse relationship between *LS* and *res* for the specified slow scan lengths (L_{sscan}).

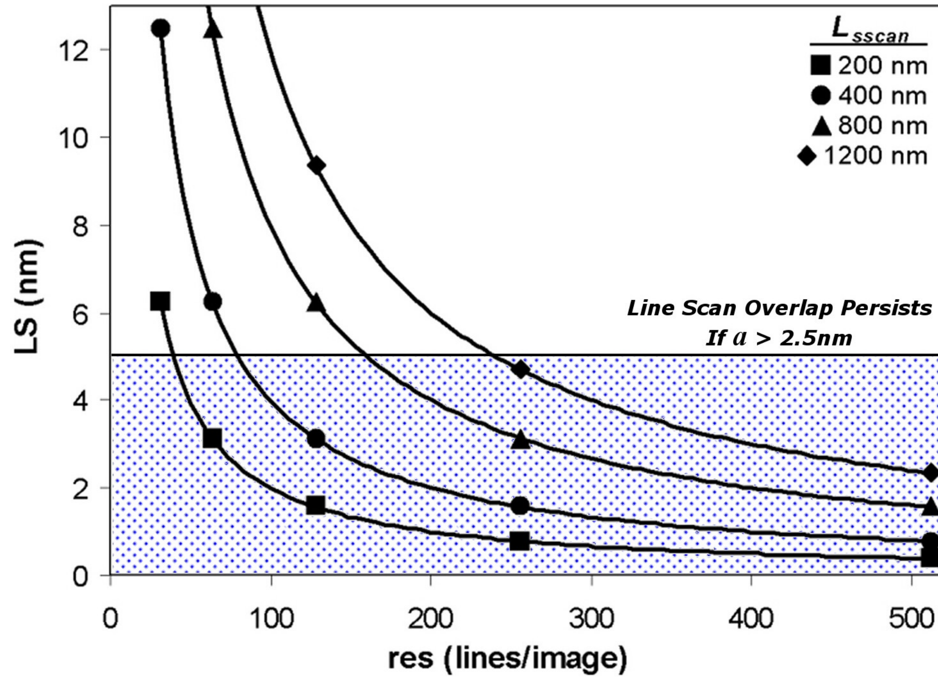

Figure 3.2 The inverse relationship between the images line step (*LS*) and image resolution (*res*) for several slow scan lengths L_{sscan}. The shaded region illustrates that scan overlap will persist if the contact radius $a > 2.5$ nm. For wear trials within the shaded area this implies that scan overlap will systematically contribute unaccounted attempts (scan history) to defect production.

$$LS = \frac{Length_{slowscan}}{resolution} = \frac{L_{sscan}}{res} \tag{3.3}$$

Taken within the context of conducting AFM wear trials, a striking feature is apparent in Figure 3.2. For a typical image resolution of 256, the line step is less than 5 nm for a L_{sscan} of 1.2 μm, indicating that unless $a \leq 2.5$ nm, overlap of successive lines traces will occur. Furthermore, the contribution of scan overlap, postulated to introduce unaccounted scan history to the surface, becomes more significant for the smaller scan areas common to nanotribology studies (e.g. $LS \sim 1.56$ nm for a L_{sscan} of 400 nm with a *res* of 256). In order to assess the impact of scan overlap on surface degradation, a comparison of overlapping and non-overlapping trials conducted under identical load

conditions is required. Comparison is accessible by establishing criteria that effectively eliminates line scan overlap from AFM experiments. The *c*ontact *r*adius - *l*ine *s*tep ratio (*CRLS*), eq. 3.4, intuitively provides this bridge for comparison. Within the non-overlap limit, eq. 3.4 states that the ratio of the contact radius to line step is required to be less than or equal to one-half.

$$CRLS = \frac{a}{LS} \leq 1/2 \tag{3.4}$$

This relationship further indicates that when the line step equals the contact diameter ($LS = 2a$), all areas of the imaged substrate are contacted with the AFM tip while still avoiding overlap of successive line scans. This specific solution to eq. 3.4 is taken as the ideal condition for an AFM wear trial, and therefore is employed to establish the ideal length of the slow scan axis (L_{sscan}^{CRLS}), which is simply the product of the contact diameter and image resolution eq. 3.5. Within the Hertz model, substitution then provides a general form of L_{sscan}^{CRLS}, which can be determined *a priori* provided the tip radius of curvature is known, and the applied load and image resolution are predefined. The relationship expressed in eq. 3.5 is especially useful for the realization of self-consistent load dependent wear studies, since a L_{sscan}^{CRLS} versus F_z plot enables experiments to be designed and conducted in the absence of scan overlap and the unaccounted scan history it imparts to the surface.

$$L_{sscan}^{CRLS} = 2a \times res = res \times \left(\frac{6\,RF_z}{\varepsilon} \right)^{1/3} \tag{3.5}$$

The proposed analysis is intended to condition AFM data sets so that a single image scan, for a range of applied loads, systematically applies a single scan's worth of load dependent contact history to the surface. Here, line scan overlap and the contribution of secondary, defect generating scanning attempts are explicitly avoided, and therefore condition the data set for more intensive analysis; such as relating the number of image scans to defect nucleation's kinetic parameters.[5,12,13,29,30,37,38] In this regard, if it is assumed that the Hertz pressure distribution adequately describes the tip-surface contact over a range of applied loads, then the geometric (contact) attempt frequency by the defect initiating body, i.e. the AFM tip, is well defined within a single scan limit. By not considering this in the design of AFM nanotribology studies, the scan history will invariably be convoluted with the non-linear load dependencies implied by the eqs.(3.3-3.5). Although avoiding these secondary influences is desirable, comparison of wear trials with and without scan overlap could potentially provide further insight into the kinetics of defect nucleation within defective lattices, enabling the activation energies for primary, secondary and tertiary events to be ascertained.[32,33]

The work presented herein focuses on testing the appropriateness of *CRLS* analysis in this context by directly comparing the overlapping and non-overlapping cases. Although the rational behind avoiding the overlap of successive line scans is logical, one may dismiss its utility since single, repeated line traces accomplish this without complication. Additionally, the most commonly used AFM tips possess parabolic profiles that invariably yield position dependent stresses relative to the contact center (see Figure 3.3). This latter point is addressable in a several ways: (1) the radial stress variation can be included in models of the tip-surface contact for studies probing the

dynamics of tip mediated defect generation, and (2) one can employ intentionally blunted probes with a flattened, punch like contact area.[39] One of the principal justifications of the proposed analysis relates to measurement accuracy within the active trial area and the favorable statistics achieved when working over nanoscale areas greater than the contact diameter. The sensitivity to the typically small population of defects nucleated within the wear trial area has been found to be readily monitored by at least one of the scanning probe observables, e.g. friction, adhesion or surface topology. Previous work on mica wear succinctly demonstrated this aspect, where during the early stages of defect nucleation, discernible changes in topography and friction were not readily apparent, while significant changes in the mean F_{adh} between the native and defective mica surfaces were observed.[1,2,6,7] The ability to accurately probe adhesive interactions within the large scan area, i.e. (400×400) nm^2, therefore proved beneficial. Conversely, generating a statistically relevant F_{adh} data set from the repeated, single-line trace studies would encompass several experimental challenges considering the critical dimension (contact diameter) of the test area would have been less than 10 nm. In lieu of the experimental liberties obtained when working with large, nanoscale test areas, the impetus to improve the accuracy of AFM data sets related to tip mediated tribochemical processes is desirable. *CRLS* analysis provides such an improvement, where the excess tip-surface contact history resulting from line scan overlap is evaluated. In conjunction with the experimental guidelines outlined by this method, the calculated excess history is then implemented as a correction factor for overlapping wear trial data, which further enables the wear behavior to be predicted for a range of applied loads. Although the analysis presented here only accounts for the elastic component of the tip-surface contact,

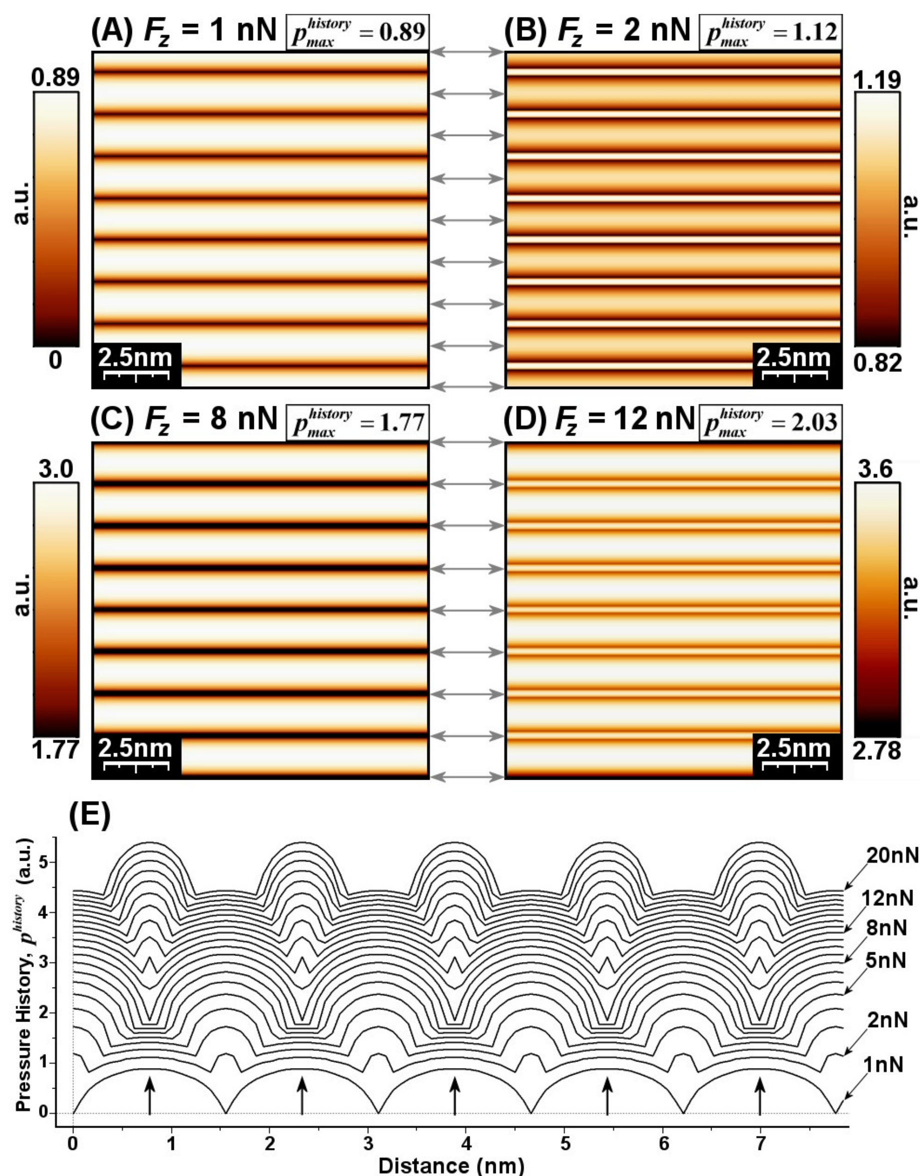

Figure 3.3 Simulated AFM image scans depicting the local cumulative, scan history resulting from overlap of Hertz contacts for several applied loads; a) without scan overlap and (b-d) with varying degrees of scan overlap. Simulations were conducted for a silicon tip, R = 30nm, on a mica surface over a (400 × 400) nm^2 image area. AFM scanning parameters (*res* = 256, *LS* = 1.5625 nm) were held constant for all simulations. The depicted images are of a (12.5 ×12.5) nm^2 portion of the simulated scan area. (e) Cumulative scan history pressure profiles, normal to the fast scan axis, for a variety of applied loads. Profiles show the periodic movement of the cumulative pressure history peak from the contact center to the middle of the line traces. Gray arrows, with a *LS* pitch of 1.5625 nm, indicate the location of the fast scan raster direction, as well as, the tip-sample contact center.

the estimated systematic errors in recorded scan history are none the less representative of the minimum contribution of scan overlap effects. Therefore, these approximations

can be immediately applied to correct earlier F_z vs. N_{scans} studies and presents a foundation for continued improvement. The *CRLS* methodology thereby provides a unique experimental framework for conducting comparative scanning probe nanoscale investigations of defect propagation with, and without, the influence of line scan overlap.

Additionally, in the instances where a scanned probe is employed as a scribe for nanolithography, the presented methodology may also provide enhanced control over nanoscale pattern fabrication and fidelity. In such situations, it is advantageous to uniformly populate a surface with a single species of defects (e.g. charges, holes, vacancies etc.) associated with a discrete wear regime or nanoscale feature. Our previous studies demonstrated that tip-mediated degradation of mica's surface proceeds sequentially in a three step process: (1) an initial surface charging due to M-O bond rupture; (2) fragmentation/displacement of the SiO_n/AlO_n basal units yielding ~ 2.2 Å holes; and (3) removal of the aluminate layer yielding 10 Å holes.[1,2] This process is readily controlled even with line scan overlap, further making mica an ideal candidate to test *CRLS* analysis. To assess the ideal (without overlap) and non-ideal (with overlap) cases, it is necessary to get a handle on the effects of scan overlap and to bridge the two scenarios in terms of the additional scan history overlap imparts to the surface.

The cumulative nature of line scan overlap and how it can add additional complexity to scanning probe nanoscale investigations can be visualized in simulated AFM wear trials. The images of Figure 3.3 are representative wear simulations of a silicon AFM tip (R = 30 nm) on a mica surface under a variety of applied loads. The AFM scanning parameters were held constant for these examples, i.e. a (400 × 400) nm^2 scan area and an image resolution of 256 (*LS* of 1.5625 nm). The values of these

parameters are consistent with those typically employed in experimentation, as well as, those used throughout the course of our work in developing this analysis. The images of Figure 3.3 are high resolution views, (12.5 × 12.5) nm^2, of a portion of the trial area. Here, the image contrast represents the cumulative (additive) pressure history, $p^{history}$, (arbitrary scale units) experienced by the surface at specific locations in the scanned image area. The gray arrows represent the line step's fast scan direction where the center of the AFM tip is rastered during imaging. Importantly, it is here, at the center of the tip-surface contact, where the Hertz pressure distribution is at its maximum (p_{max}), equal to 1.5× the mean contact pressure (p_m), and corresponds to the peak in the pressure history for trials conducted in the absence of line scan overlap. However, when line scan overlap exists the *cumulative* pressure history ($p^{history}$) may not coincide with p_{max}. Due to the *additive* accounting employed in the simulations, this peak radial stress is redefined as the non-dimensional maximum pressure history, $p_{max}^{history}$, and is given in the upper right hand corner of each image for reference. There are several interesting features appearing in Figures 3.3b-d that are direct consequences of line scan overlap. As implied, Figure 3.3a represents the ideal *CRLS* scan, where under an applied load of 1 nN scan overlap does not occur. Here, as would be expected from the Hertz model, the peak pressure history ($p_{max}^{history}$ ~ 0.89) is found at the contact center as indicated by the intensity scale bar. However, as the load is increased so does the contact diameter, ($F_z \propto a^3$), which leads to the cumulative pressure profiles found in Figures 3b-c. The most striking feature of these simulations is the movement of cumulative pressure history peak from the contact center to the midpoint between successive line traces. Even under low loads, for example 2 nN in Figure 3.3b, this progressive translation leads to a maximum cumulative pressure

($p_{max}^{history}$ ~ 1.19) at the midpoint between line traces and not at the contact center ($p^{history}$ ~ 1.12). Furthermore, the movement is periodic, a direct consequence of the contact radius- load - *LS* inter-dependency. The profiles in Figure 3.3e clearly illustrate this periodic variation in the cumulative pressure history intensity for a range of applied loads, noting that arrows at the bottom of the plot indicate the position of the contact center during each line trace.

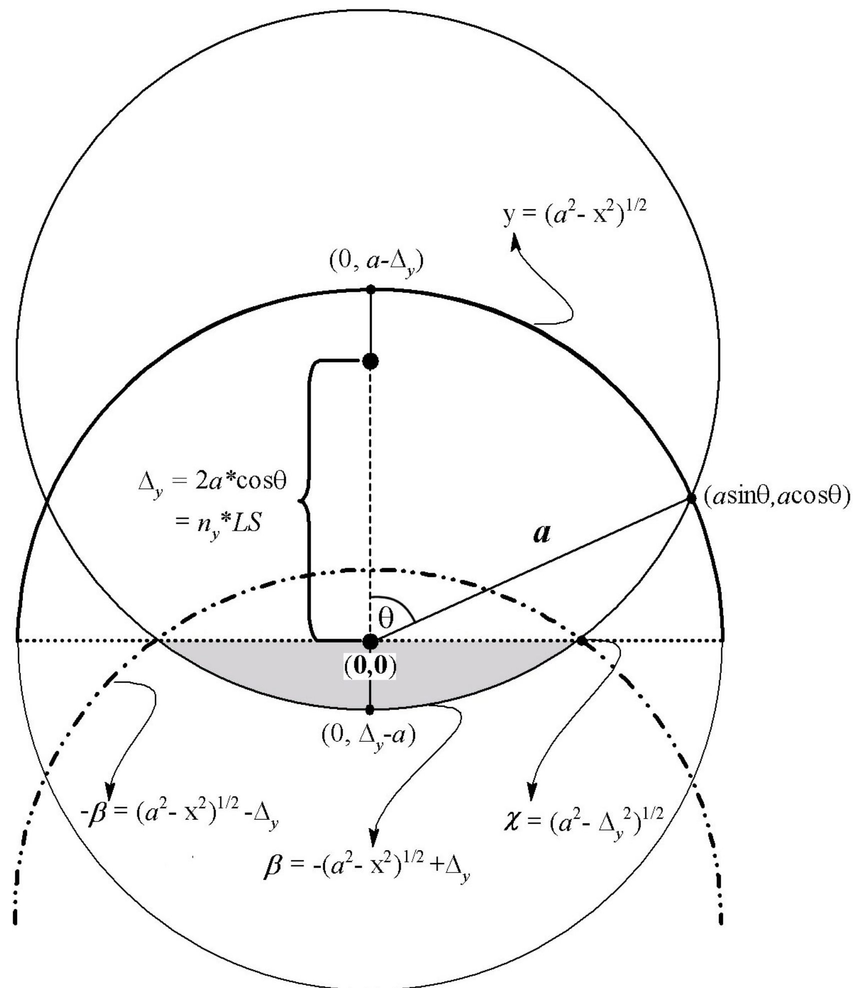

Figure 3.4 Geometry of overlapping contacts of radii *a* according to Hertz continuum mechanics theory.

The additional scan history evident in the simulated AFM scans of Figure 3.3 can be estimated in terms of a scan correction ($scan_{cor}$), defined as the number of *non-overlapping* scans required to achieve, under identical experimental conditions, the same contact history (e.g. degree of wear) in an overlapping trial. $Scan_{cor}$ can be arrived at naturally by association to the force of overlap (F_{ovlp}), which is simply the integrated Hertz pressure within the area of overlap in successive line traces. According to the Hertz model, the pressure distribution $p(r)$ is given in terms of r, the distance from the center of contact via eq. 3.6.[27,28,36] Once the boundary of the overlapping area is defined, F_{ovlp} can be estimated numerically. The derivation of the expressions employed for numerical evaluation can be found in the Appendix 3.1.

$$F_z = \int_0^{2\pi}\int_0^{a} p(r) r dr d\theta = \frac{1.5 F_z}{\pi a^2}\int_0^{2\pi}\int_0^{a}\left(1-\frac{r^2}{a^2}\right)^{1/2} r dr d\theta = \frac{2 p_{max} \pi a^2}{3} \tag{3.6}$$

Here, p_{max} is the maximum contact pressure and is equal to 1.5× the Hertz mean pressure (p_m). In our calculations we employed the following, eq. 3.7, Cartesian coordinate form of $p(r)$.

$$p(x,y) = \left[1 - \frac{(x^2+y^2)}{a^2}\right]^{1/2} \tag{3.7}$$

In practice, $scan_{cor}$ is calculated in terms of F_{ovlp}^{Total}, eq. 3.8a, the total force within all successive overlapping line traces. F_{ovlp}^{Total} is formulated from a geometric breakdown of sequential overlapping circular contacts of radii a, Figure 3.4, leading to the three integrals in expression 3.8b. Normalizing F_{ovlp}^{Total} with ($F_z \times res$) approximates the additional, dimensionless scan history per experimental scan imparted to the surface from

line scan overlap. The pressure distributions $p(x,y)$ hemispherical symmetry is accounted for by the two preceding the summation and the functions α, β, and χ are given in eqs. 3.9 - 3.11, and are also noted in Figure 3.4.

$$scan_{cor} = 1 + \frac{F^{I}_{ovlp} - F^{II}_{ovlp} + F^{III}_{ovlp}}{res \times F_z} = 1 + \frac{F^{Total}_{ovlp}}{res \times F_z} \tag{3.8a}$$

$$= 1 + \frac{2 \times \sum_{m_l}^{m_i} \{res - m_y\} \left(\frac{1.5 F_z}{\pi a^2} \right) \left[\int_0^{a \sin(\theta)} \int_0^{\sqrt{a^2 - x^2}} p(x,y)\, dy dx - \int_{\alpha}^{a \sin(\theta)} \int_0^{\beta} p(x,y)\, dy dx + \int_0^{\chi} \int_0^{-\beta} p(x,y)\, dy dx \right]}{res \times F_z} \tag{3.8b}$$

$$\alpha = \begin{cases} 0 & \text{for } \left(\theta \le \frac{\pi}{3} \right) \\ \chi & \text{for } \left(\theta > \frac{\pi}{3} \right) \end{cases} \tag{3.9}$$

$$\beta = -\sqrt{a^2 - x^2} + 2\, a \cos(\theta) \tag{3.10}$$

$$\chi = \sqrt{a^2 - (2\, a \cos(\theta))^2} \tag{3.11}$$

The Hertz half-space and the associated overlap are undefined for negative y values and therefore necessitates the third integral in eq. 3.8b whose first integration limit is the negative of eq. 3.10. This situation arises when $\theta > 60°$ or equally $\Delta_y > a$. Here, Δ_y is the center-to-center distance along the slow scan axis for successive line traces as referenced to the first scan line ($n_0 = 0$).

$$\Delta_y = n_y \times LS = 2a \cos(\theta) \tag{3.12}$$

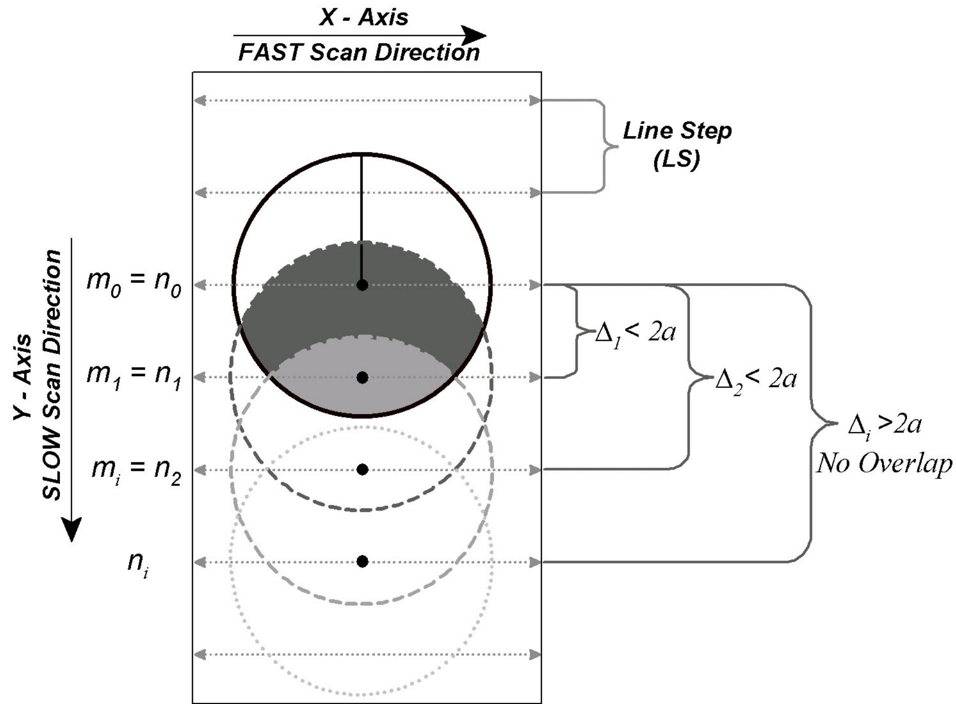

Figure 3.5 Illustration of the elements used for $scan_{cor}$ analysis of sequential raster lines.

The positive integer increment n_y corresponds to the nth line step from n_0 as shown in Figure 3.5. Again the steps are along the slow scan axis, which is arbitrarily assigned to the *y*-axis in Figures 3.4 and 3.5. Since scan overlap does not occur for the ith successive scan, where $\Delta_i \geq 2a$, the series is then truncated on the line scan prior to the n_i ($n_i = 2a / LS$) line trace. For convenience the summation is re-defined in terms of m_y, which encompasses the integer range [m_1, m_i], since the last overlapping line trace is $m_i = n_{i\text{-}1}$ and the 1 in eqs. 3.8a-b accounts for n_0. The relationships defined in eqs. 3.1 and 3.12 indicate that $n_i \propto F_z^{1/3}$, which enables $scan_{cor}$ to be evaluated *a priori* for a given material pair. The merit of eq. 3.12 and the value of the θ - *a* relationship it establishes is further exemplified by its ability to simplify $scan_{cor}$ calculations. This θ - *a* relationship provides a general, geometric based form of the correction to be established and it is

proposed that this form, established with the tenets of Hertz continuum elasticity, is applicable to "all" tip – substrate material pairs.

According to *CRLS* analysis, the calculated $scan_{cor}$ provides an estimate of the additional scan history applied to the surface by scan overlap. For example, if $scan_{cor}$ has been evaluated to be unity, then there is no additional history applied to the surface from scan overlap. However, if $scan_{cor}$ is found to be greater than unity, then the surface has experienced additional scan history due to scan overlap. In this situation $scan_{cor}$ can be used to predict the number of non-overlapping scans, i.e. with a trial area defined by eq. 3.5, required to impart to the surface the identical scan history achieved when scan overlap is present. The product of $scan_{cor}$ and the experimental number of scans conducted with line scan overlap, N_{scans}^{Exp}, yields the corrected number of scans ($N_{scans}^{correct}$) within the non-overlap limit as defined by eq. 3.13. In this manner, the experimental AFM trial with line scan overlap is the "parent" from which the *CRLS* prediction, $N_{scans}^{correct}$, and future non-overlapping experiments are based. For instance, non-overlapping trials with L_{sscan} defined by eq. 3.5 can then be conducted at a Hertz mean pressure (p_m) equivalent to that of the "parent" overlapping study. After evaluation of $scan_{cor}$ for the parent trial, the paired non-overlapping wear experiment is then performed for a number of scans equal to $N_{scans}^{correct}$. The extent of surface degradation may then be evaluated for both trials with force of adhesion (F_{adh}) measurements, topography and frictional force microscopy. Again, within the Hertzian development, the two wear experiments are coupled and the elastic scan history in both trials is equivalent. Deviations from *CRLS* predictions are to be expected since the tenets of continuum elasticity do not include inelastic energy dissipation pathways natural to a wearing contact.

$$scan_{cor} \times N_{scans}^{Exp} = N_{scans}^{correct} \tag{3.13}$$

3.3 Experimental

3.3.1 CRLS Model Parameters

A silicon (Si) AFM microcantilever with a tip possessing a radius of curvature (R) of 30 nm was used for numerical $scan_{cor}$ analysis on a muscovite mica substrate. $Scan_{cor}$ was evaluated for a range of applied loads with L_{sscan} and res fixed at 400 nm and 256 lines per image, respectively. The physical constants of v_i and E_i for mica and silicon are 0.1, 56.5 GPa and 0.3, 155 GPa respectively.[5,40] Mathcad 8 (MathSoft, Inc.), Graphmatica Version 1.6e (kSoft, Inc.) and WSxM 4.0 Develop 7.4 (Nanotec Electronica S.L., Spain) were used for numerical calculations (as derived in Appendix 3.1) and graphical analysis.

3.3.2 AFM Wear Studies Empirically Testing CRLS Analysis

AFM measurements were acquired at room temperature, 22 ± 3ºC, with a Molecular Imaging Pico SPM (Phoenix, AZ), operating in constant cantilever deflection mode, coupled with RHK Technology SPM 1000 Revision 8 DSP Electronics (Troy, MI). Experimental wear trials were conducted in high purity water (18.2 MΩ·cm, Easypure RF, Barnstead, Dubuque, IA) adjusted with HCl (Fisher) to a pH ~ 5. Si_3N_4 cantilever tip assemblies were acquired from ThermoMicroscopes (Santa Clara, CA) and were SC2 cleaned prior to use in a 4:1:1 (v/v) mixture of 18.2 MΩ·cm H_2O, 30% reagent grade H_2O_2 (Fisher) and concentrated NH_4OH (Fisher) at 80°C. Imaging of a

$SrTiO_3$(305) single crystal provides an estimate of the tip apex radius of curvature (R).[41] At least 10 topographic line traces across the $SrTiO_3$(100)/(001) steps were fit with a second-order polynomial, which is then used to extract R by solving for the local asperities circle of curvature (K). The circle of curvature (K) at any point on the function ($f(x)$) is equal to $K = (|f(x)|)/([1+(f(x)')^2]^{3/2})$ and is the inverse of the (tips) radius of curvature ($K = 1/R$). For more information regarding circle of curvature calculations see Appendix 1.2. Analysis revealed that the tips used in the present study possessed an R of 76 and 68 nm. After *each* wear trial R was determined again and consistently showed no change within ±15% of the original values. Cantilever spring constants were calibrated against levers of known spring constants yielding ($k_{Tip\ radius}$) $k_{76\text{nm}} = k_{68\text{nm}} = 0.41$ N/m.[42] The values of v_i and E_i for the Si_3N_4 cantilevers are 0.24, 220 GPa respectively.[43] Wear trials were performed on (400 × 400) nm^2 and (L_{sscan}^{CRLS} × 400) nm^2 regions at a *res* of 256 lines per image, with a scan rate of 10 Hz (100 ms/line). The SC2 cleaned tip and freshly cleaved mica were allowed to equilibrate in solution for ~ 2 hours prior to wear experiments. In our previous work it was found that this equilibration time drastically reduces the effects of thermal drift during image acquisition.[1,2]

CRLS analysis was tested by implementing the paired (overlap/non-overlapping) wear trial methodology discussed previously. Briefly, $scan_{cor}$ is first calculated for the (400 × 400) nm^2 overlap wear trial under a predetermined load. Similar experiments are then performed under an identical p_m without line scan overlap, i.e. trials were conducted over a (L_{sscan}^{CRLS} × 400) nm^2 region. Here, L_{sscan}^{CRLS} is defined by eq. 3.5 and was calculated for each paired experiment. The number of scans performed for the non-overlapping wear

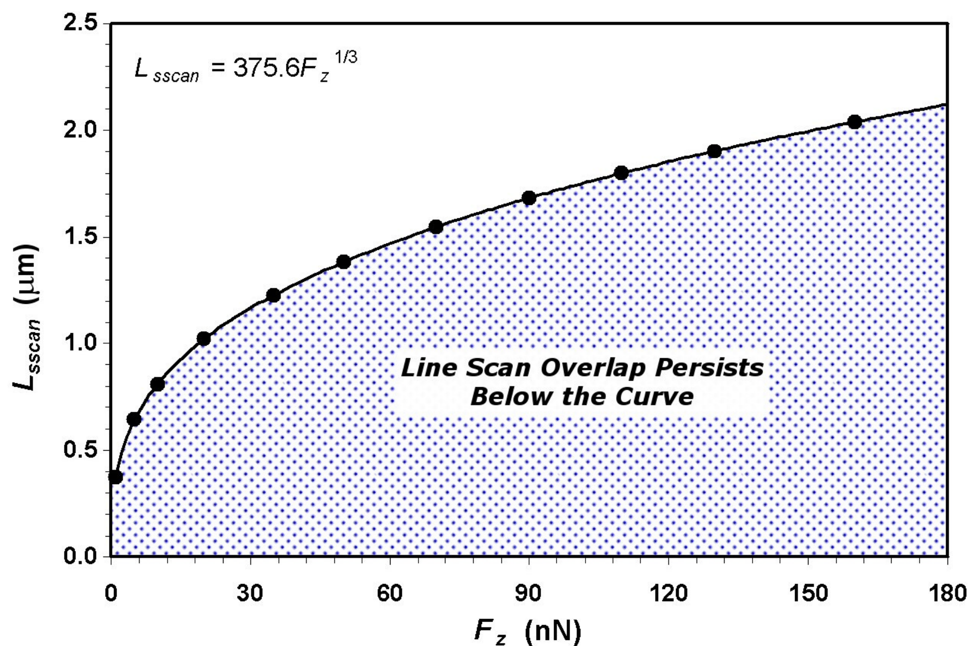

Figure 3.6 Projected slow scan length, L_{sscan}^{CRLS} defined by eq. 3.5, required to avoid line scan overlap for a silicon tip (R = 30 nm) and a mica substrate.

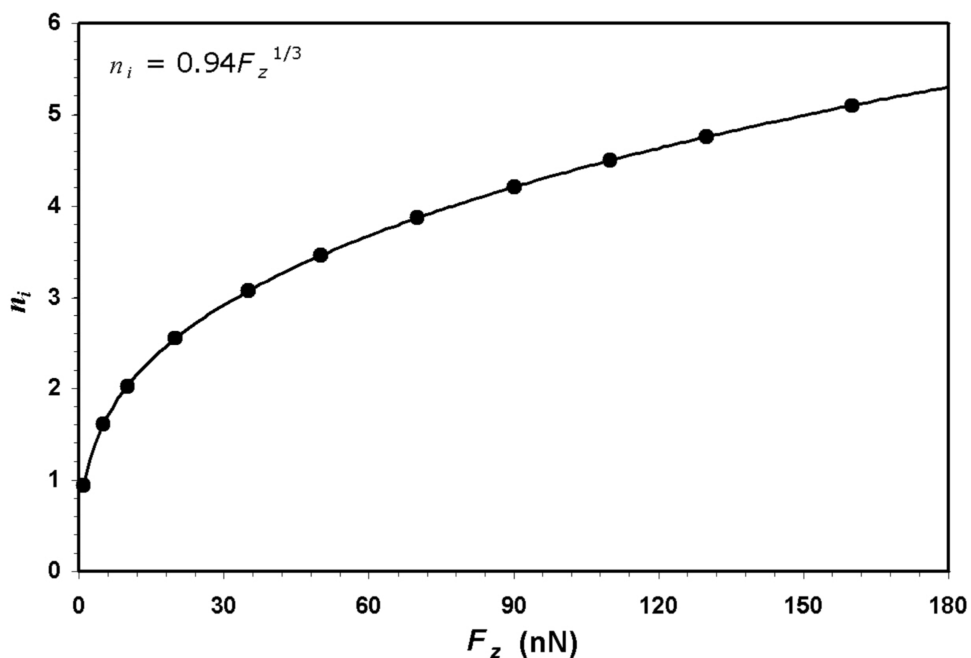

Figure 3.7 Projected truncating parameter n_i, as defined by eq. 3.12, for the silicon-mica material pair. n_i indicates the number of successive line scans with scan overlap and will therefore contribute to the unaccounted contact history that is estimated by $scan_{cor}$.

trial is predefined, $N_{scans}^{correct}$ in eq. 3.13, and is the product of $scan_{cor}$ and the experimental N_{scans} in the (400 × 400) nm^2 run. Trials conducted in this manner are then paired, meaning that the extent of wear in both regions should be nearly equivalent, although, exact duplication is not expected for trials within the severe wear regime since *CRLS* predictions use continuum elasticity theory and wearing contain inelastic processes. Force of adhesion (F_{adh}) measurements were conducted with an approach - retract rate of 50 µs per point with points acquired every 4.52 Å. Between 100 – 120 F_{adh} measurements were acquired on both the native mica surface and the wear trial area after each experiment. In this manner the native mica surface serves as an internal reference so that the degree of wear within the (400 × 400) and (L_{sscan}^{CRLS} × 400) nm^2 regions could be justly compared. Internal referencing eliminates uncertainties that can arise from wear induced changes in tip structure and chemistry. The state of the worn surface can then be evaluated by comparison of topography, F_{adh} and frictional force (F_f) imaging within the native and worn mica regions.

3.4 Results and Discussion: Does Overlap Really Matter?

3.4.1 Modeling Overlap

For the mica-Si material pair, the L_{sscan}^{CRLS} vs. F_z plot given in Figure 3.6, indicates that ideal, non-overlapping AFM wear trials over a (400 × 400) nm^2 scan area can only be achieved under very low applied loads. Similarly, Figure 3.7 illustrates the expected truncating parameters (n_i) proportionality to load ($n_i \propto F_z^{1/3}$), indicating that the number of successive scans contributing unaccounted scan history to the surface escalates non-

linearly with load. Figures 3.6 and 3.7 are instructive and clearly demonstrate that the systematic error associated with this geometric-scanning effect can pervade AFM nanotribology data sets. As outlined by the *CRLS* analysis, this systematic error is addressable and can be quantified in terms of a $scan_{cor}$. An analytical solution of eq. 3.8b over all θ is not available and therefore $scan_{cor}$ was evaluated numerically for a wide range of loads, including those summarized in Appendix Table A3.1. Figure 3.8 illustrates the expected shifted power law dependence $scan_{cor}$ has on F_z, eq. 3.14, for the mica-silicon material pair. The interpretation of $scan_{cor}$ is straightforward. Referring to Figure 3.8, under a load of 75 nN, $scan_{cor}$ was found to be 2.29, meaning that a single image scan imparts 2.29 scans worth of scan history to the surface or more than doubles the probability of initiating the events associated with defect nucleation and growth. Calculations also show that even for a load of 5 nN, $scan_{cor}$ expressed a 25% departure from the experimental number of scans value (Table A3.1). These results provide compelling insight into the actual history experienced by the surface and prompts new questions into how this additional scan history affects defect growth and interpretation of extracted kinetic parameters. More on this aspect is addressed at the end of this chapter.

$$scan_{cor} = 0.4379 \times F_z^{1/3} + 0.5534 \times F_z^{-0.0555} \qquad (3.14)$$

Although one can extrapolate the correction for a range of loads with this expression, it is not a universal solution since the variables, namely *res*, *LS* and the material dependent *a*, are part of the fit. According to this Hertzian development, a *percent force overlap* vs. θ plot, Figure 3.9, is a universal overlap correction curve and is applicable to any tip-substrate material pair. This general overlap correction curve is realized by taking advantage of the normalized θ - *a* relationship derived from the Hertz

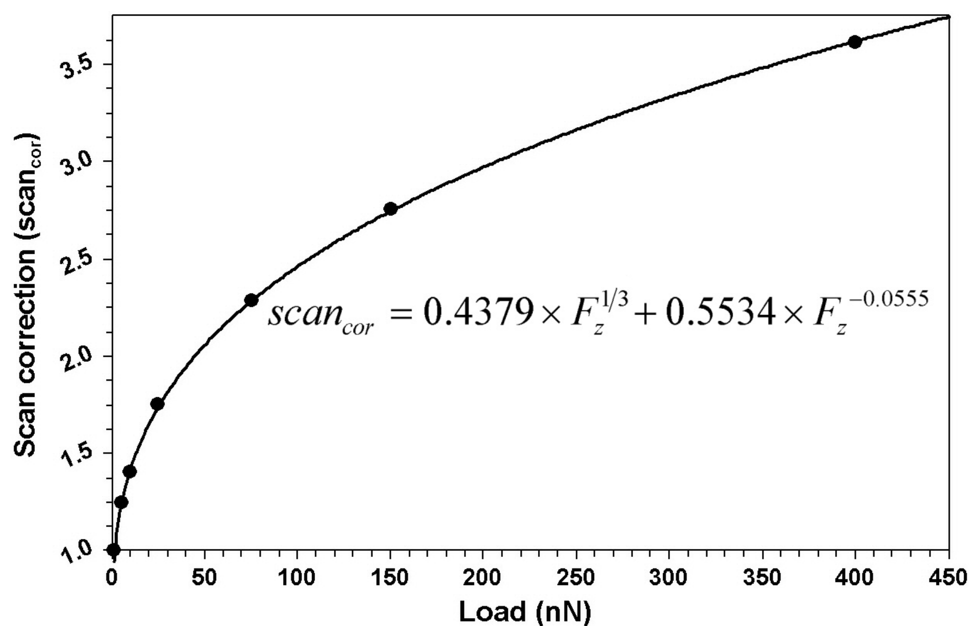

Figure 3.8 Numerical results of eq. 3.8b for $scan_{cor}$ (filled circles in plot). AFM image parameters were *res* of 256 (LS = 1.5625 nm) and L_{sscan} of 400 nm for a silicon AFM tip (R = 30 nm) and a mica substrate. Linear regression analysis (solid line) finds that $scan_{cor}$ follows a shifted power law dependence with F_z.

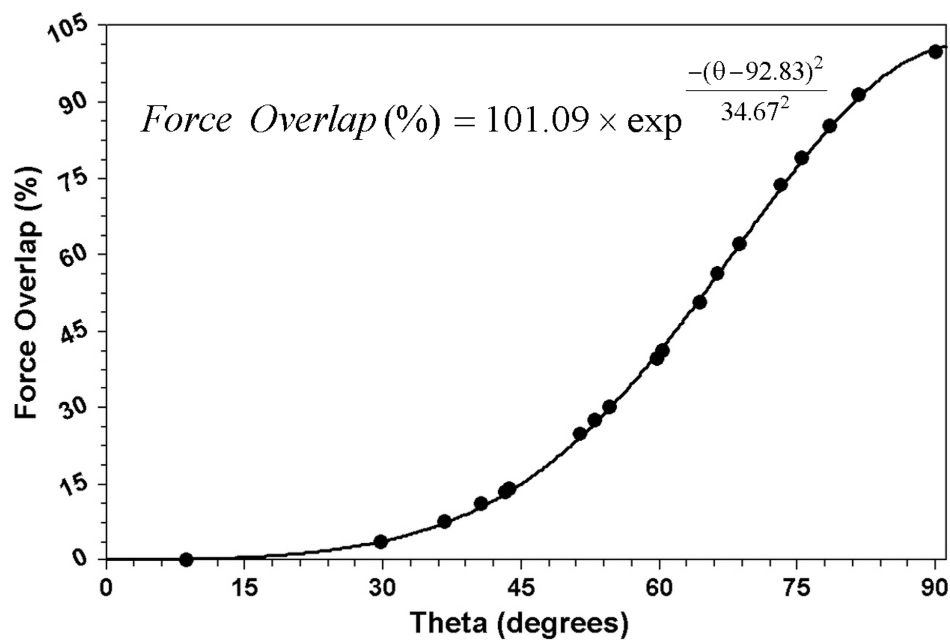

Figure 3.9 General form of the overlap correction curve for all tip-substrate material combinations for estimating $scan_{cor}$. Linear regression analysis (solid line) finds that the percent force overlap grows exponentially with θ.

contact geometry, eq. 3.12, and by leaving the m_y and *res* variables for the final summation. Thus, the general $scan_{cor}$ form is given as a function of (θ, m_y), where both parameters have pure geometric origins centered on a. One can then readily calculate $\theta(m_y)$ and simply sum over the range of angles to get $scan_{cor}$ via eq. (3.15). Non-linear regression analysis finds a standard error of 0.48 for the fit in Figure 3.9, which corresponds to a few percent error in the calculated $scan_{cor}$. Thus, eq. 3.15 is a reasonable approximation of eq. 3.8b and provides a straightforward expression to implement the *CRLS* methodology for all tip-substrate material pairs.

$$scan_{cor}(\theta, m_y) = 1 + \sum_{\theta(m_l)}^{\theta(m_i)} \left[\frac{res - m_y}{res} \right] \times \left(1.0109 \times exp^{\frac{-(\theta - 92.83)^2}{34.67^2}} \right) \tag{3.15}$$

3.4.2 Paired AFM Wear Studies

Wear trials were first performed over a (400 × 400) nm^2 region under a p_m of 1.4 GPa for 5 scans. As can be seen in Figure 3.10b/f the F_f has decreased, relative to the native mica, in most of the worn region yet there is little to no change in topography, Figure 3.10a/d, in the same low friction areas. We have previously addressed the qualities of pH dependent wear of mica and owe this to localized Si-O/Al-O surface bond rupture yielding negatively charged surface species.[1,2] Since the oxidized, hydroxylated Si_3N_4 tip primarily exhibits a SiO_2 surface at pH 5,[44] and the isoelectric point (IEP) of SiO_2 falls between pH 2-3, the tip will therefore carry a net *negative* charge under these aqueous conditions.[45-47] We can therefore conclude that the extra repulsive interactions acting between the negatively (-) charged defective surface and the negatively (-) charged tip lead to the observed decline in friction (Figure 3.10b/f). The broad distribution of F_{adh}

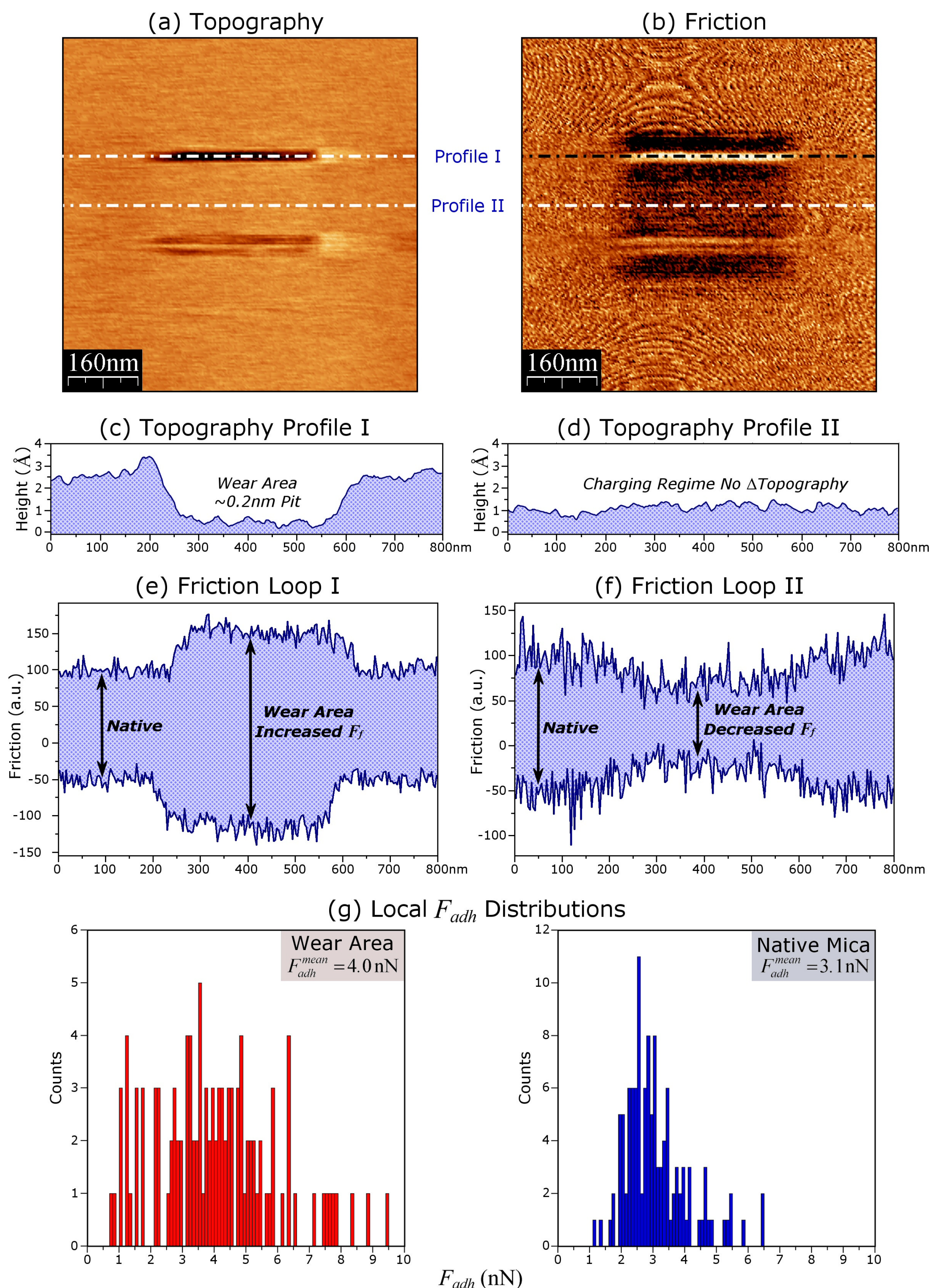

Figure 3.10 AFM analysis of wear trial area *with* scan overlap. Trial was conducted for 5 scans over a (400 × 400) nm^2 scan area under a p_m of 1.4 GPa. AFM a) topography, b) frictional force, F_f, and the respective topography profiles (c-d) and friction loops (e-f). g) Local F_{adh} distributions for the native and wear trial areas. Each distribution consists of at least 110 F_{adh} measurements. According to eqs. (3.5 and 3.13), L_{sscan} and $scan_{cor}$ are 2.2 μm and 3.0 respectively. In practice the paired trial was conducted with L_{sscan} of 2.0 μm (Figure 3.11).

measurements, Figure 3.10g, suggests that the worn surface and tip possess several types of defects (e.g. charges and pits). This is also evident in the topography (Figure 3.10c) and F_f (Figure 3.10e) profiles, which indicate the presence of 2.2 Å holes with a correspondingly higher friction. Working under solution conditions gives us the ability to chemically qualify these observations based upon the unique IEP of the individual mica layers. Using Al_2O_3 IEP (pH ~ 9) as a reference, it is anticipated that the surface of mica's aluminate layers should retain a net *positive* charge under these pH 5 conditions and thereby introduce the additional attractive tip/surface potential. This is consistent with the increased frictional force, relative to the native mica surface, observed for the 2.2 Å deep holes.[1,47]

The paired, non-overlapping ($L_{sscan}^{CRLS} \times 400$) nm^2 trial was conducted using *CRLS* analysis of the preceding experiment with line scan overlap. *CRLS* calculations indicate that the slow scan length (L_{sscan}^{CRLS}), under an equivalent load, should be 2.2 μm. $Scan_{cor}$ was found to be 3.0, instructing us to perform the non-overlapping wear trial for a total of 15 scans (eq. 3.13). In practice a L_{sscan}^{CRLS} of 2.0 μm was used because the spring constant of the AFM cantilever was calibrated after the trials were complete and the nominal spring constants were used in the initial, experimentally applied L_{sscan} calculations. In all cases the error between theoretical and experimental L_{sscan} was ~10% and is not likely to substantially influence the results. The topographic and F_f images, Figure 3.11a-b, show that surface charging Figure 3.11d/f and abstraction Figure 3.11c/e of materials from the mica surface also occurs for the non-overlapping experiment.[1] The extent of wear for this *CRLS* experiment is in near quantitative agreement with the previous (400 × 400) nm^2 overlapping trial, as indicated by the relative area composed of ~ 0.22 nm pits

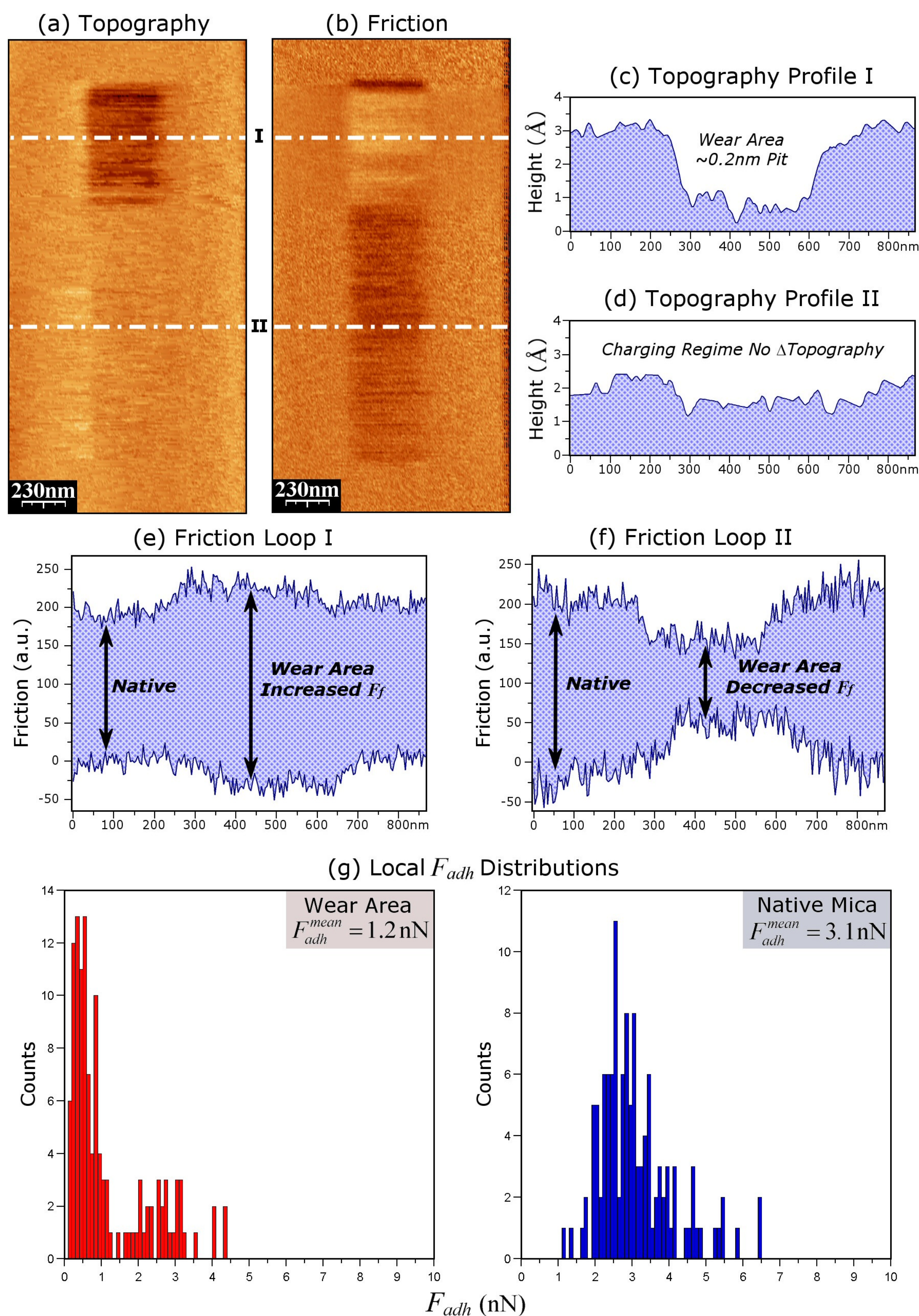

Figure 3.11 AFM analysis of the wear trial area, *without* scan overlap, that is paired with the trial in Figure 3.10. Trial was conducted for 15 scans over a (2000 × 400) nm^2 scan area under a p_m of 1.4 GPa. AFM a) topographic and b) frictional force, F_f, and the respective topography profiles (c-d) and friction loops (e-f). g) Local F_{adh} distributions for the native and wear trial areas. Each distribution consists of at least 110 F_{adh} measurements.

(abstraction regime). In terms of a percentage, ca. 21% of the overlapping trial area is occupied by ~ 0.22 nm pits, while ca. 30 % of the non-overlapping, *CRLS* trial area possesses ~ 0.22 nm pits. The agreement in the extent of surface degradation for the paired trials within the *mild* wear regime for mica is impressive, especially considering the simplicity of this analysis.

There are, however, important distinctions between these two trials that are noteworthy. For instance, closer inspection with FD spectroscopy, comparing Figure 3.10g and Figure 3.11g, clearly indicates that the F_{adh} distributions within the wear trial area for the two studies are markedly different. For the non-overlapping wear trial, a narrow F_{adh} distribution, Figure 3.11g, with two distinct peaks is evident, while a broad distribution is observed in the overlapping case Figure 3.10g. The discrete peaks in the *CRLS* trial likely represents the two fundamental defect species generated during mica surface damage; proceeding in a discrete progressive fashion, i.e. from the surface charging (surface bond rupture) to the molecular abstraction (~ 0.22 nm pits) regime.[1] There is, however, a noticeable difference in the maximum F_{adh} measured between these two trials that needs further inquiry, as the origin of this difference is presently unclear. In a broader sense, the FD spectroscopy measurements may also be indicating that defect generation is more uniform in the non-overlapping, ($L_{sscan}^{CRLS} \times 400$) nm^2, trial region than in the paired overlapping, (400×400) nm^2, trial. Although more work is required to substantiate this hypothesis, it is not an unreasonable conjecture, considering that the sequence of defect generating events for the *CRLS* derived trials are geometrically more evenly distributed over the working area.

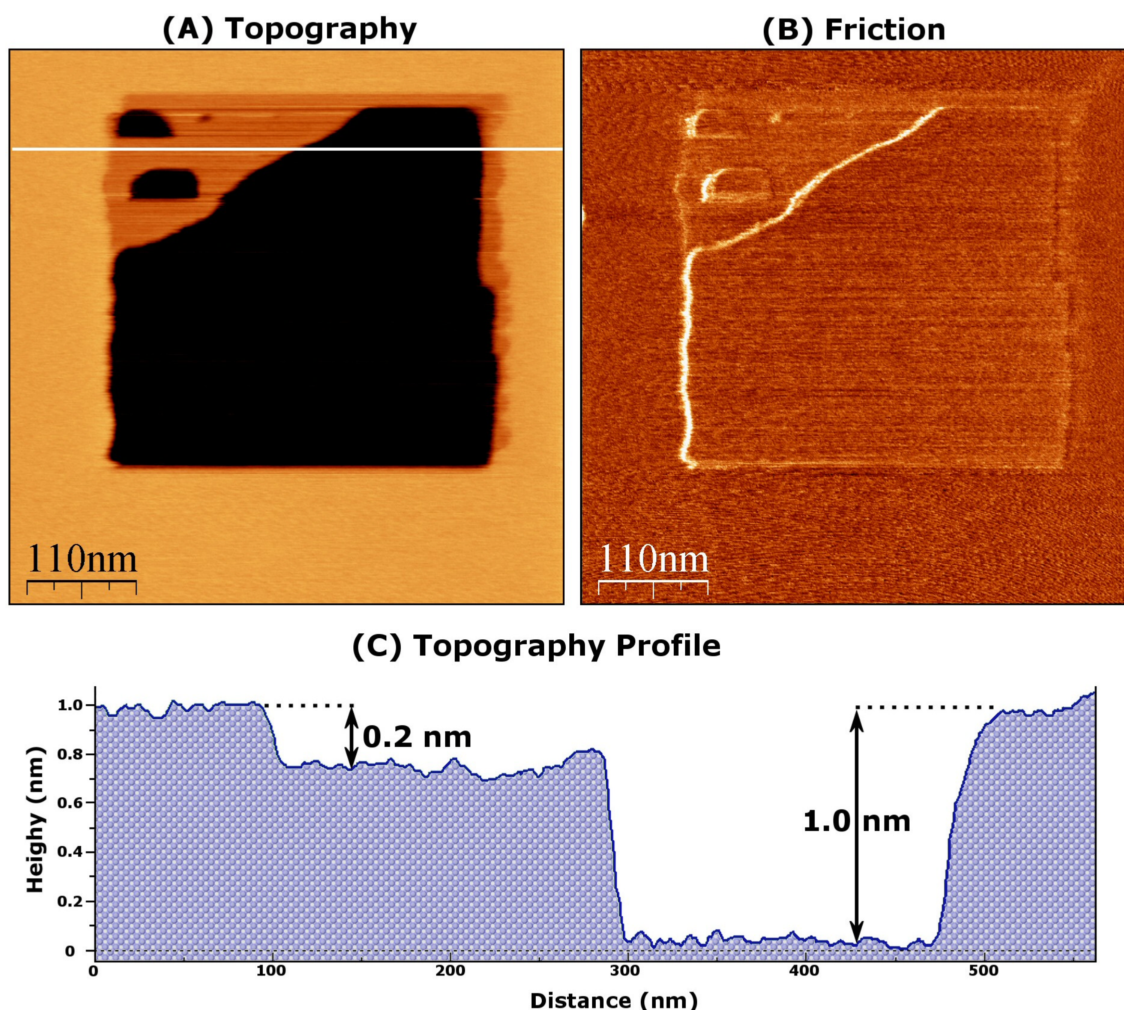

Figure 3.12 AFM analysis of wear trial area *with* scan overlap. Trial was conducted for 10 scans over a (400 × 400) nm^2 scan area under a p_m of 1.5 GPa. AFM a) topographic and b) frictional force, F_f, and c) topography profile. According to eqs. (3.5 and 3.13), L_{sscan} and $scan_{cor}$ are 2.3 μm and 3.2 respectively. In practice the paired trial was conducted with L_{sscan} of 2.1 μm (Figure 3.13).

To test this hypothesis, *CRLS* analysis was also employed to investigate its predicative capabilities within the gross deformation regime; a regime where elastic energy dissipating pathways only account for a small part of the total energy within the contact. Gross wear trials were similarly performed over a (400 × 400) nm^2 region under a p_m of 1.5 GPa for 10 scans. This resulted in removal of the first mica repeat layer, leaving a 10 Å wear scar over ~ 85% of the scan area, Figure 3.12a/c. Frictional force

imaging, Figures 3.12b, is unable to detect a difference between the native and worn SiO_3 planes, corroborating topography measurements that a complete repeat layer was excavated. The residual area is defined by a ~ 2.2 Å deep step, resulting from removal of the outermost $Si\text{-}O_3$ surface units. Again, the 2.2 Å deep hole exposes the surface of the aluminate layer and, although much less distinct, an increase in friction is observed (profile not shown). The small ΔF_f in the aluminate area may be attributed to tip-size effects, as well as, a high population of defects present on this layers surface (indicated by the two 10 Å holes in the center of the ~ 2.2 Å deep step). The controlled generation of 2.2 Å and 10 Å holes has been previously demonstrated by Salmeron et al.,[5] as well as, by Helt et al.[1] In the solution studies by Helt and Batteas[1], the ease of generating the 10 Å holes far exceeds that of the 2.2 Å, as the apparent threshold pressure for breakdown of the aluminate layer, again under pH 5 conditions, appears to be less than the threshold pressure for breakdown of the basal (001) crystal plane. There are inherent difficulties in establishing even a nominal value for the aluminate layers threshold pressure, as the apical SiO_3/AlO_3 units of the basal plane need to be removed without introducing defects into this layer. The lack of clear friction contrast on the 2.2 Å step, Figure 3.12b, instructs us that this alumina layer is likely highly defective even though topographically it appears to be intact.

Again a paired ($L_{sscan}^{CRLS} \times 400$) nm^2 trial was conducted using *CRLS* analysis of the preceding (400 × 400) nm^2 run. Contact radius-line step calculations within the non-overlap limit led to a L_{sscan}^{CRLS} of 2.3 μm and a $scan_{cor}$ of 3.2, indicating that this run would consist of 32 scans. An L_{sscan}^{CRLS} of 2.11 μm was used for reasons explained earlier. As illustrated in Figures 3.13a/b, after 32 scans nearly exclusive removal of the basal planes

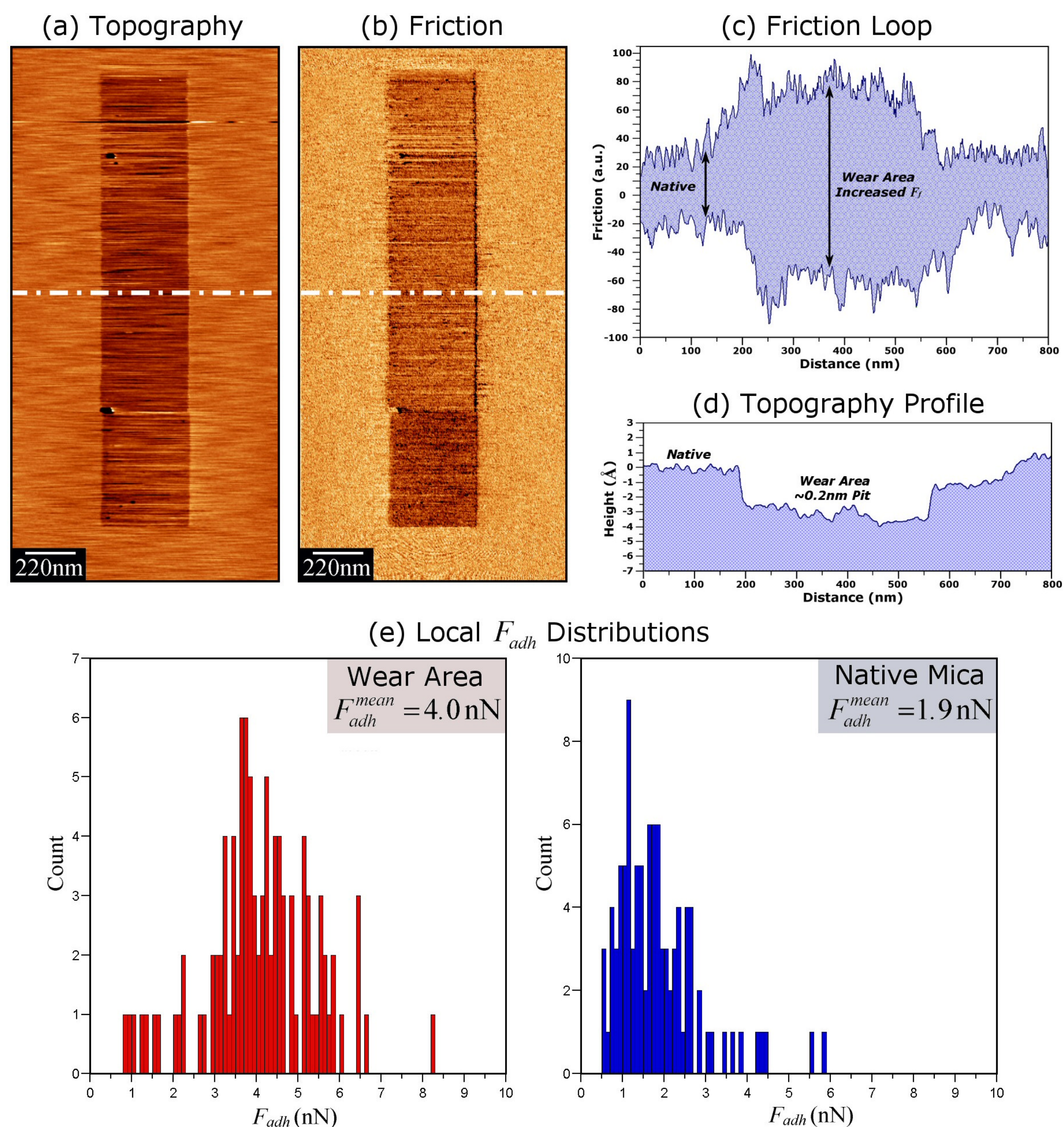

Figure 3.13 AFM analysis of the wear trial area, *without* scan overlap, that is paired with the trial in Figure 3.12. The wear trial was conducted for 32 scans over a (2100 × 400) nm^2 scan area under a p_m of 1.5 GPa. AFM a) topographic and b) frictional force, F_f, images and the respective (c) friction loop and (d) topography profile. e) Local F_{adh} distributions for the native and wear trial areas. Each distribution consists of at least 100 F_{adh} measurements.

apical SiO_3/AlO_3 molecular fragments resulted, yielding a 2.2 Å deep region. Here the wear scars feature fidelity is impressive and supports our earlier hypothesis that the more uniform load distribution enabled by this analysis invariably increases the resulting wear scar uniformity. Clearly the 2.2 Å hole has a larger F_f (Figure 3.13c) and F_{adh} (Figure

3.13e) relative to the native mica owing to the coulombic attraction between the net negatively (-) charged tip and net positively (+) charged aluminate surface. A significant departure in the extent of wear, relative to the parent (400 × 400) nm^2 trial in Figure 3.12, is observed in both topographic and F_f imaging. This clearly demonstrates the importance of scan overlap on defect growth, where rapid removal of the aluminate layer occurs as a direct consequence of the additional scan history applied within overlapping sequential line traces. The inability of the *CRLS* model to accurately predict this gross wear behavior is a testament to the significance of line scan overlap in the generation and propagation of defects within inelastic contacts. Considering the presented model is based entirely on elastic continuum mechanics, such deviations are expected and instructive. Here, the role of scan overlap on defect growth is substantial and results in removal of a complete mica crystalline layer, which is equivalent to progressing to a completely distinct wear regime. This is compelling evidence that such effects can compromise AFM data sets. Our paired AFM wear experiments show that the presented approach can be to used establish a benchmark for probing the details of how defects proliferate, especially since a variety of derivative tests, such as varying *res* with a fixed scan size, may also be pursued.

There are several instances where *CRLS* analysis and $scan_{cor}$ can be beneficial. Recent work investigating mica wear under vacuum and humid conditions by Salmeron et al. utilized the relationship between the number of AFM scans, load, micas material properties and the tip penetration depth to estimate the critical defect density (η_{crit}) for breakdown of micas surface.[5] In their studies the scan size was held constant, while F_z was incrementally adjusted. This allowed them to monitor the number of scans (N_{scans})

required to remove the apical SiO_3/AlO_3 basal units (create a 2.2 Å pit) at each load. This data was then used to extract η_{crit} and physical constants (B_0) from a N_{scans} - F_z plot initially developed by Dickinson.[12,13] From Figure 3.2 and the load range specified in their work it is apparent that scan overlap existed. According to *CRLS* analysis, the experimental N_{scans} is expected to be *smaller* than the actual number of scans experienced by the surface. This is worth noting since the employed theory holds $N_{scans} \propto e^{(-B_0)}$, and as pointed out by the authors, the fitted B_0 was overestimated by ~13×. Part of this disagreement can be attributed to an *underestimate* of N_{scans} that results from the overlap of successive line traces.[5] In a similar case, our recent work investigating muscovite mica wear in aqueous solution also did not account for this additional scan history and prevented kinetic analysis of the initiating stages of defect nucleation, which is readily followed as a reconstruction of the native mica lattice from 5.2 Å to 3 Å periodicity.[1] In this work, the lattice reconstruction is observed to occur progressively within the first 20 experimental scans conducted over a (7×7) nm^2, under an applied load of 9 nN (p_m ~ 1.25GPa). If we employ *CRLS* analysis to find the corrected number of scans for these trials we find $scan_{cor}$ to be ca. 50, which indicates that a *single* experimental scan imparts roughly 50 scans of history to the surface. This is of course one of the principle reasons for development of the *CRLS* data set conditioning. Although such a finding is disconcerting, it does, however, present a possible novel use of the calculated $scan_{cor}$. For instance, such lattice resolved wear trials could be viewed as accelerated wear studies and enable rapid analysis of a materials tribological properties from nanoscale studies. A considerable amount of work is still required to fully assess the accuracy and predictive capabilities of the scan overlap model, yet there are several unique aspects that indicate

that this approach will assist both fundamental and practical inquires into defect nucleation and growth.

3.5 Summary and Conclusions

The systematic error attributed to scan overlap can be avoided by the *CRLS* analysis described. Our analysis has also arrived at a general expression that can estimate the actual scan history for previous experiments possessing scan overlap, allowing more accurate prediction of tip mediated wear phenomena. Experimentally, predictions are encouraging within the mild wear regime limit for mica under aqueous solution conditions, yet the current model is incapable of following severe wear trends. The empirical evidence obtained validates the importance of scan overlap in AFM wear studies and holds promise as a new methodology for probing the earliest stages of defect growth. Although, experiments containing line scan overlap can be beneficial for probing defect nucleation, comprehensive studies should include non-overlapping trials since the comparison can provide valuable new insight into how overlap and defect growth couple.

Appendix 3.1 - Derivation of Expressions for Scan Correction ($scan_{cor}$) Calculation

The initial functional form defining the regions of overlapping Hertz contacts of radius a is:

$$\left(\frac{1.5\,F_z}{\pi a^2}\right)\left[\int_0^{a\,sin\,(\theta)}\int_0^{\sqrt{a^2-x^2}} p(x,y)\,dy\,dx \;-\; \int_\alpha^{a\,sin\,(\theta)}\int_0^{\beta} p(x,y)\,dy\,dx \;+\; \int_0^{\chi}\int_0^{-\beta} p(x,y)\,dy\,dx\right]. \tag{A3.1}$$

As previously defined in the text and in Figure 3.4, the limits of integration β and χ are:

$$\beta = -\sqrt{a^2-x^2} + 2\,a\,cos(\theta) \tag{A3.2}$$

and

$$\chi = \sqrt{a^2-(2\,a\,cos\,(\theta))^2}\;. \tag{A3.3}$$

The three separate double integrals were evaluated independently as follows.

I. Integration of the first function in eq. (A3.1) –

$$2\left(\frac{3\,F_z}{2\pi a^2}\right)\int_0^{\sqrt{a^2-x^2}}\sqrt{\frac{a^2-x^2}{a^2}-\frac{y^2}{a^2}}\,dy \;=\; 2\left(\frac{3\,F_z}{2\pi a^2}\right)\left(\frac{\pi\left(a^2-x^2\right)}{4\,a}\right) \;=\; \left(\frac{3\,F_z}{4\,a^3}\right)\left(a^2-x^2\right), \tag{A3.4}$$

which is then integrated with respect to x to yield the analytic solution:

$$\left(\frac{3\,F_z}{4\,a^3}\right)\int_0^{a\,sin\,(\theta)}\left(a^2-x^2\right)dx \;=\; \left(\frac{3\,F_z}{4}\right)\left(sin\,(\theta) - \frac{1}{3}sin\,(\theta)^3\right). \tag{A3.5}$$

II. Integration of the second function in eq. (A3.1) –

$$2\left(\frac{3\,F_z}{2\pi a^2}\right)\int_0^{-\sqrt{a^2-x^2}+2\,a\cdot cos\,(\theta)}\sqrt{\frac{a^2-x^2}{a^2}-\frac{y^2}{a^2}}\,dy = \tag{A3.6}$$

$$=\left(\frac{3F_z}{2\pi a^3}\right)\left[\sqrt{4a\,cos(\theta)\sqrt{a^2-x^2}-4a^2\,cos(\theta)^2}\times\left(-\sqrt{a^2-x^2}+2a\,cos(\theta)\right)+\left(a^2-x^2\right)arcsin\left(\frac{2a\,cos(\theta)}{\sqrt{a^2-x^2}}-1\right)\right] \tag{A3.7}$$

Expression (A3.7) is then numerically evaluated with respect to x:

$$\int_{\alpha}^{a\ sin\ (\theta)} (\text{eq. A3.7})\, dx\ , \tag{A3.8}$$

where the integration limit α is dependent on the magnitude of angle θ. For θ greater than π/3, α is equal to χ as previously defined.

$$\alpha = \begin{cases} 0 \ \text{ for } \left(\theta \le \dfrac{\pi}{3}\right) \\ \chi \ \text{ for } \left(\theta > \dfrac{\pi}{3}\right) \end{cases} \tag{A3.9}$$

III. Integration of the third function in eq. (A3.1) –

$$\left(\frac{3F_z}{2\pi a^3}\right) \int_{0}^{\sqrt{a^2-x^2}-2a\cdot cos(\theta)} \sqrt{\frac{a^2-x^2}{a^2}-\frac{y^2}{a^2}}\, dy = \tag{A3.10}$$

$$=\left(\frac{3F_z}{2\pi a^3}\right)\left[\sqrt{4a\,cos(\theta)\sqrt{a^2-x^2}+4a^2\,cos(\theta)^2}\times\left(\sqrt{a^2-x^2}-2a\,cos(\theta)\right)+\left(a^2-x^2\right)arcsin\left(1-\frac{2a\,cos(\theta)}{\sqrt{a^2-x^2}}\right)\right] \tag{A3.11}$$

Expression (A3.11) is then evaluated numerically with respect to x:

$$\int_{0}^{\sqrt{a^2-(2a\cdot cos(\theta))^2}} (\text{eq. A3.11})\, dx\ . \tag{A3.12}$$

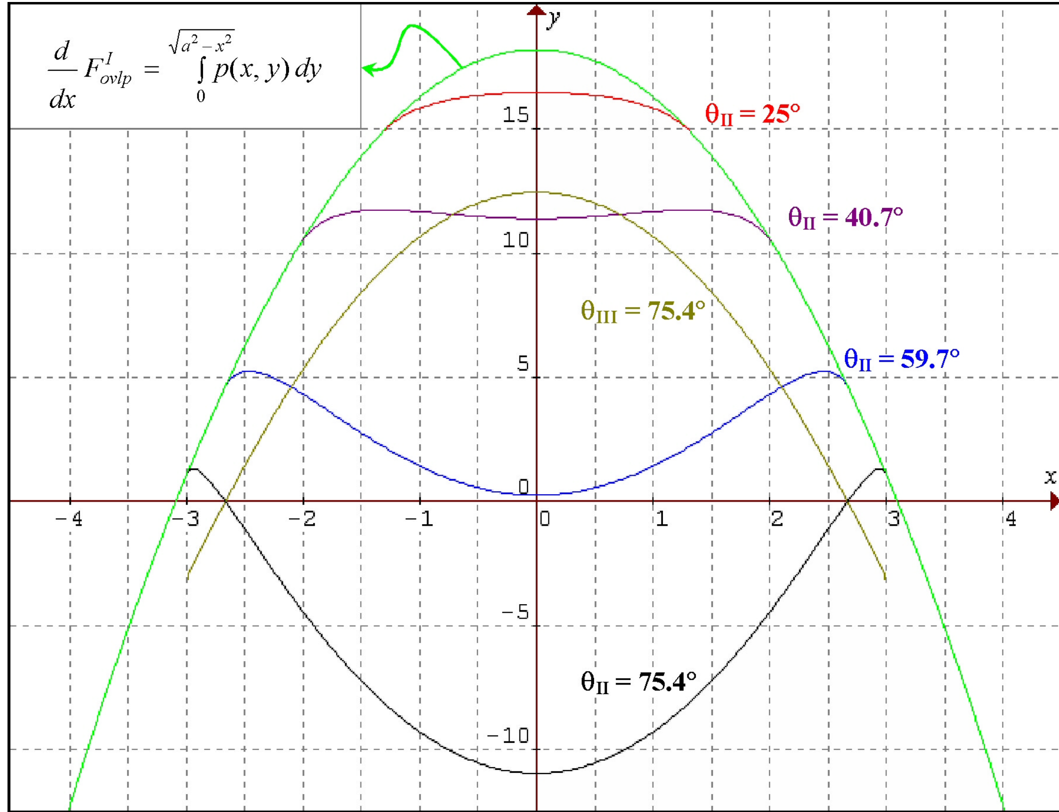

Figure A3.1 - Example forms of eqs. (A3.4, A3.7, A3.11) after first integration of for mica-silicon material pair. Here the load was 75 nN corresponding to a Hertz mean pressure (p_m) of 2.5 GPa. Experimental parameters were: R = 30 nm, res = 256, L_{sscan} = 400 nm and LS =1.5625 nm. The first term, F^{I}_{ovlp} given in eq. (A3.4), after first integration is independent of θ and is marked with the arrow. All functions defined with θ_{II} are forms of the *second* term (F^{II}_{ovlp}, eq. A3.7) after the first integration for the given angle. θ_{III} is representative of the *third* term (F^{III}_{ovlp}, eq. A3.11), which is only evaluated for θ > 60°.

Table A3.1 - Parameters and results from line $scan_{cor}$ calculations

F_z (nN)	a (nm)	n_i	$scan_{cor}$
1	0.73	1	1.00
5	1.25	2	1.25
10	1.58	3	1.41
25	2.14	3	1.76
75	3.09	4	2.29
150	3.90	5	2.75
400	5.41	7	3.62

ε =57.0 GPa[5], R = 30 nm, res = 256 and LS =1.5625nm

Chapter 3 References

(1) Helt, J. M.; Batteas, J. D. *Langmuir* **2005**, *21*, 633.

(2) Helt, J. M.; Batteas, J. D. Mica Surfaces: Charge Nucleation and Wear. In *Dekker Encyclopedia of Nanoscience and Nanotechnology*; Schwarz, J. A., Contescu, C. I., Putyera, K., Eds.; Marcel Dekker Inc.: New York, 2004; Vol. 3; pp 1947.

(3) Deer, W. A.; Howie, R. A.; Zussman, J. Rock-Forming Minerals. In *Sheet Silicates*; Longmans, Green and Co.: London, 1962; Vol. 3.

(4) Wyckoff, R. W. G. *Crystal Structures*; Interscience: New York, 1971.

(5) Kopta, S.; Salmeron, M. *J. Chem. Phys.* **2000**, *113*, 8249.

(6) *Modern Tribology Handbook*; 1st ed.; Bhushan, B., Ed.; CRC Press: Boca Raton, 2001; Vol. 1, pp 1460.

(7) *Springer Handbook of Nanotechnology*; 1 ed.; Bhushan, B., Ed.; Springer: Berlin, 2004, pp 1222.

(8) Binnig, G.; Quate, C. F.; Gerber, C. *Phys. Rev. Lett.* **1986**, *56*, 930.

(9) Binnig, G.; Gerber, C.; Stoll, E.; Albrecht, T. R.; Quate, C. F. *Europhys. Lett.* **1987**, *3*, 1281.

(10) Carpick, R. W.; Salmeron, M. *Chem. Rev.* **1997**, *97*, 1163.

(11) Bhushan, B.; Israelachvili, J. N.; Landman, U. *Nature* **1995**, *374*, 607.

(12) Dickinson, J. T.; Park, N. S.; Kim, M. W.; Langford, S. C. *Tribol. Lett.* **1997**, *3*, 69.

(13) Dickinson, J. T.; Hariadi, R. F.; Langford, S. C. *Ceram. Trans.* **1999**, *102*, 213.

(14) Batteas, J. D.; Quan, X. H.; Weldon, M. K. *Tribol. Lett.* **1999**, *7*, 121.

(15) Noy, A.; Vezenov, D. V.; Lieber, C. M. *Annu. Rev. Mater. Sci.* **1997**, *27*, 381.

(16) Hu, J.; Xiao, X. D.; Ogletree, D. F.; Salmeron, M. *Surf. Sci.* **1995**, *327*, 358.

(17) Marti, A.; Hahner, G.; Spencer, N. D. *Langmuir* **1995**, *11*, 4632.

(18) Carpick, R. W.; Agrait, N.; Ogletree, D. F.; Salmeron, M. *Langmuir* **1996**, *12*, 3334.

(19) Wei, Z. Q.; Wang, C.; Bai, C. L. *Langmuir* **2001**, *17*, 3945.

(20) Qian, L. M.; Xiao, X. D.; Wen, S. Z. *Langmuir* **2000**, *16*, 662.

(21) Cain, R. G.; Biggs, S.; Page, N. W. *J. Colloid Interface Sci.* **2000**, *227*, 55.

(22) Barrena, E.; Kopta, S.; Ogletree, D. F.; Charych, D. H.; Salmeron, M. *Phys. Rev. Lett.* **1999**, *82*, 2880.

(23) Lio, A.; Charych, D. H.; Salmeron, M. *J. Phys. Chem., Part B* **1997**, *101*, 3800.

(24) Ogletree, D. F.; Carpick, R. W.; Salmeron, M. *Rev. Sci. Instrum.* **1996**, *67*, 3298.

(25) Gnecco, E.; Bennewitz, R.; Gyalog, T.; Loppacher, C.; Bammerlin, M.; Meyer, E.; Guntherodt, H. J. *Phys. Rev. Lett.* **2000**, *84*, 1172.

(26) Bennewitz, R.; Gnecco, E.; Gyalog, T.; Meyer, E. *Tribol. Lett.* **2001**, *10*, 51.

(27) Johnson, K. L. *Contact Mechanics*; Cambridge University Press: Cambridge, 1987.

(28) Johnson, K. L.; Kendall, K.; Roberts, A. D. *Proceedings of the Royal Society of London Series A -Mathematical Physical and Engineering Sciences* **1971**, *324*, 301.

(29) Scudiero, L.; Langford, S. C.; Dickinson, J. T. *Tribol. Lett.* **1999**, *6*, 41.

(30) Park, N. S.; Kim, M. W.; Langford, S. C.; Dickinson, J. T. *Langmuir* **1996**, *12*, 4599.

(31) Carpick, R. W.; Dai, Q.; Ogletree, D. F.; Salmeron, M. *Tribol. Lett.* **1998**, *5*, 91.

(32) Pelmenschikov, A.; Strandh, H.; Pettersson, L. G. M.; Leszczynski, J. *J. Phys. Chem., Part B* **2000**, *104*, 5779.

(33) Pelmenschikov, A.; Leszczynski, J.; Pettersson, L. G. M. *J. Phys. Chem., Part A* **2001**, *105*, 9528.

(34) Israelachvili, J. N. *Intermolecular and Surfaces Forces*, 2nd ed.; Academic Press: New York, 1992.

(35) Adamson, A. W. *Physical Chemistry of Surfaces*; Wiley & Sons: New York, 1990.

(36) Hertz, H. *J. Reine Angew. Math.* **1881**, *92*, 156.

(37) Park, N. S.; Kim, M. W.; Langford, S. C.; Dickinson, J. T. *J. Appl. Phys.* **1996**, *80*, 2680.

(38) Maw, W.; Stevens, F.; Langford, S. C.; Dickinson, J. T. *J. Appl. Phys.* **2002**, *92*, 5103.

(39) Carpick, R. W.; Agrait, N.; Ogletree, D. F.; Salmeron, M. *J. Vac. Sci. Technol., B* **1996**, *14*, 1289.

(40) Mcneil, L. E.; Grimsditch, M. *J. Phys.: Condens. Matter* **1993**, *5*, 1681.

(41) Sheiko, S. S.; Moller, M.; Reuvekamp, E. M. C. M.; Zandbergen, H. W. *Phys. Rev. B: Condens. Matter* **1993**, *48*, 5675.

(42) Tortonese, M.; Kirk, M. *SPIE Proc. - Micromach. Imag.* **1997**, *3009*, 53.

(43) Hazel, J. L.; Tsukruk, V. V. *J. Tribol. - Trans. ASME* **1998**, *120*, 814.

(44) Fischer, T. E.; Mullins, W. M. *J. Phys. Chem.* **1992**, *96*, 5690.

(45) Bousse, L.; Mostarshed, S. *J Electroanal Chem* **1991**, *302*, 269.

(46) Colic, M.; Franks, G. V.; Fisher, M. L.; Lange, F. F. *Langmuir* **1997**, *13*, 3129.

(47) Arai, T.; Aoki, D.; Okabe, Y.; Fujihira, M. *Thin Solid Films* **1996**, *273*, 322.

Chapter 4.

A Benchtop Method for the Fabrication and Patterning of Nanoscale Structures on Polymers

4.1 Introduction

The drive to economically reduce electronic and sensor architectures to the nanometer level has prompted a creative surge in soft lithographic techniques.[1,2] These include microcontact printing (μCP),[3-10] nanoimprint lithography (NIL),[11-19] soft molding,[20] reverse NIL,[21] laser-assisted direct imprint (LADI),[22] cold welding nanotransfer,[23] lithography controlled wetting,[24] superlattice nanowire pattern transfer (SNAP),[25] nanotransfer printing (nTP),[26-28] molecular transfer lithography (MxL),[29] and micromolding in capillaries (MIMIC).[30-33] The processing requirements of each method (e.g., chemical treatments, temperatures, and pressures) as well as substrate compatibility are generally the limiting factors that narrow the range of materials that can be prepared by any single method mentioned above. For example, while most of these methods can be used to form metal nanostructures on planar[4,13,23,26,29,34] and/or curved surfaces,[35,36] the formation of patterned arrays of organic and inorganic molecules and particles are more readily obtained with capillary condensation,[24,37] MIMIC,[2,30-33,38-41] and μCP.[3,5-7,42-46] These methods may be combined by sequential implementation to provide several routes for the construction of multilevel, multiple composition nanostructured frameworks. An

additional driving force for the continued development of soft lithographic techniques is that an economic advantage can be provided by methods which enable direct transfer of patterned materials to other substrates (via either additive or subtractive processes) without the need for additional chemical treatments. This reduces the number of processing steps, the associated production of waste, and the inefficient use of materials from each step. Cold welding nanotransfer is one such example where direct transfer is possible, and this approach has proven to be compatible with the fabrication of organic-based components with potential use in the fabrication of molecular electronic devices.[23,47] Nanotransfer printing with chemically[26,28] and physically[29] driven interfacial "bonding" has also proven to be an effective means of metal surface patterning and has recently been illustrated for the formation of electrical test structures using self-assembled monolayers on surfaces such as GaAs.[48]

In this chapter, we present a method for the ***s***ynthesis and ***t***ransfer ***o***f ***m***aterials to and from ***p***olymers (STOMP), which may find applications in constructing sensors,[49] electronic devices,[50] optical materials,[51,52] photolithography masks[53] and layered photonic band gap structures.[54] As with many other soft lithographic (SL) techniques, STOMP utilizes preferential surface "modification" with a structured polymeric stamp in order to direct the formation of metal structures onto the stamp or substrate surface. The stamp geometry, interfacial free energies (hydrophilic/hydrophobic interactions) and applied loads cooperate to guide the resulting metal feature size. This benchtop route allows for the fabrication of multiple metal micro/nanostructures within the recesses and/or on the raised portions of a polymer stamp without the need for the addition of an 'adhesive' layer to direct the transfer of materials to the polymer stamp. Although other techniques

such as μCP are also capable of varying structural dimension (i.e., reducing feature size) by etching, the ability to directly produce and transfer metal arrays to a structured polymer in a single step is difficult to generate with other methods. The structures formed on the polymer stamps by the STOMP processes can also be subsequently transferred to other surfaces allowing the fabrication of multilayered structures, such as metallic gratings with nanoscale dimensions.

4.2 Experimental

4.2.1 General Patterning Process

In the STOMP method, nanostructures are formed by the compression of a malleable metal film (such as Au) deposited on a rigid support (such as mica) by a polymer stamp followed by chemical etching while the metal film is under compression by the stamp. The STOMP processing begins by initially wetting the Au and polymer surfaces with ultrapure water (EASYpure RF, 18.2 MΩ·cm, Barnstead, Dubuque, IA), methanol (Fisher Scientific), or a 1:1 v/v water/methanol mixture before compression to suppress bubble formation between the stamp and substrate and to reduce the surface tension between the water-based etchant and hydrophobic stamp. The samples were etched while under compression with Transene gold etchant type TFA (Danvers, MA), which was diluted with ultrapure water in ratios ranging from 2:3 to 1:12.5 v/v TFA/H_2O. Custom-built Teflon compression cells designed to hold ~ 1 cm^2 samples were used to compress polymer stamps against the Au coated surfaces under a fixed uniform load. After securing the components, the compression cells were immersed in 100 mL of the gold etchant solution. Etching was carried out at room temperature (22 ± 3°C) with rapid

stirring from 4 - 72 hrs, with a typical etching time of 20 h. Heating of the solution up to 70 ± 2°C could also be used to reduce the required etching times. After etching, the compression cell was dismantled and the sample removed and rinsed with a solvent, such as methanol, to facilitate the separation of the two surfaces and to reduce disruption of the Au nanostructures formed. The polymeric stamp and substrate were then gently rinsed with copious amounts of ultrapure H_2O and dried under vacuum (10 mTorr) at room temperature. The resulting structures were then characterized with scanning electron microscopy (SEM) and atomic force microscopy (AFM).

4.2.2 Fabrication of Polymer Stamps

Several different polymer stamps were used in this work. Micromolded polystyrene (PS) (MW of 235,000, Scientific Polymer Products Inc., Ontario, NY) stamps were fabricated by molding from a master silicon grating (such as TGG01, MikroMasch, Portland, OR), with an active area of 9 mm^2 or from a silicon AFM calibration standard (Veeco/TM Microscopes, Sunnyvale, CA), with an active area of 20 mm^2. The polymer stamps were formed by placing the silicon template face up in an aluminum or Teflon cell with 0.5 g of PS placed over the template. The cell was then heated to 210 ºC for 2 h and allowed to cool to room temperature. The PS stamp was then separated from the silicon template with brief sonication (2 min) in methanol and subsequently rinsed with ultrapure water. In addition to fabricated stamps, delaminated, commercially available recordable polycarbonate (PC) compact disks (CDs) could also be employed as stamps. CDs have been used as stamps in several patterning methods,[55,56] and are also suitable stamps for STOMP. The CD stamps were prepared by

removing the reflective metallic layer via scoring and vigorous rinsing with ultrapure water. The recording media was then removed with a rapid methanol rinse followed by brief sonication (30 s) in a 1:4 (v/v) methanol/water solution and a final rinse with ultrapure water. The stamps were then cut to the desired size.

4.2.3 Formation of Au Films

Gold (Au) films were prepared with a sputter coater (BAL-TEC MED 020, Liechtenstein, Germany). The Au target (99.99% purity) was obtained from Techno Trade International (Manchester, NH). Substrates coated with Au included freshly cleaved muscovite mica (Structure Probe Inc., West Chester, PA), glass coverslips (Fisher Scientific), and Si(100) wafers (Virginia Semiconductor, Fredericksburg, VA). The prepared films ranged from 70 to 300 nm in thickness with a deposition rate between 0.2 and 2 nm/s. The evaporated films exhibited a surface roughness of 5 – 10 nm RMS.

4.2.4 Evaluation of Load Dependence on Pattern Formation

The compressive load dependence on the structures that could be formed using STOMP was evaluated using two approaches. First, using a simple sequential variation of the load in a series of experiments with a planer compression cell, whereby the pressure is nominally uniform across the stamp/substrate interface. The second uses a nonplanar compression configuration in which convex lenses acted as the compression plates (*vide infra*). This second approach has the advantage that using the curved compression geometry results in a radial pressure gradient at the stamp-substrate interface, which allows for an entire series of structure vs load to be evaluated in a single experiment. The

normal load and pressure distribution could then be estimated with continuum contact mechanics theory (neglecting effects of the Au film[57-60]) as well by comparison to the observed deformation of the Au films and polymer stamps evaluated *ex situ* using a calibrated press.[61] The *ex situ* load dependent experiments evaluating deformation of the Au film by the polymer stamp were performed using a press employing a set of calibrated springs with a maximum load capacity of 153 ± 1.8 N.

4.2.5 Micro-Nanostructure Characterization

AFM images were acquired with either a Molecular Imaging Pico SPM (Phoenix, AZ) coupled with an RHK Technology SPM 1000 Controller, Revision 8 (Troy, MI), or a Park Scientific Autoprobe LS AFM (Veeco/TM Microscopes, Sunnyvale, CA). All AFM

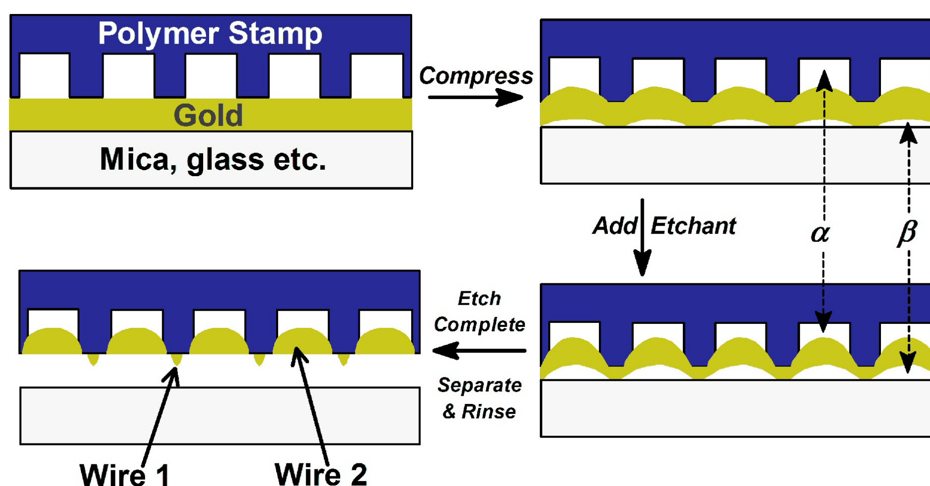

Figure 4.1 Schematic of the STOMP protocol using planar stamps with square sidewalls. A polymer stamp from a compact disk or prefabricated from a master template is brought into compressive contact with an Au film (typically 70 - 300 nm thick) on a rigid support such as mica, glass, or Si. Compression induces buckling in the Au film producing two channels, α and β. As the β channel is more hydrophilic than the α channel, etching occurs preferentially through the β channel and under the stamp ridges. After an etching step, the stamp and support are separated and rinsed. Depending on the duration of etching, Au micro/nanostructures form on the stamp ridges (*wires 1*) and/or within the stamp recesses (*wires 2*).

images were acquired in contact mode using commercially available Si_3N_4 AFM tips (Veeco, Sunnyvale, CA) with nominal tip radii of 10 – 30 nm and nominal spring constants of 0.1 N/m. SEM images were obtained with an Amray 1800 (KLA Tencor, San Jose, CA). To minimize charging, the typical SEM imaging conditions used an electron beam current of 110 μA with an acceleration voltage of 3.1 kV.

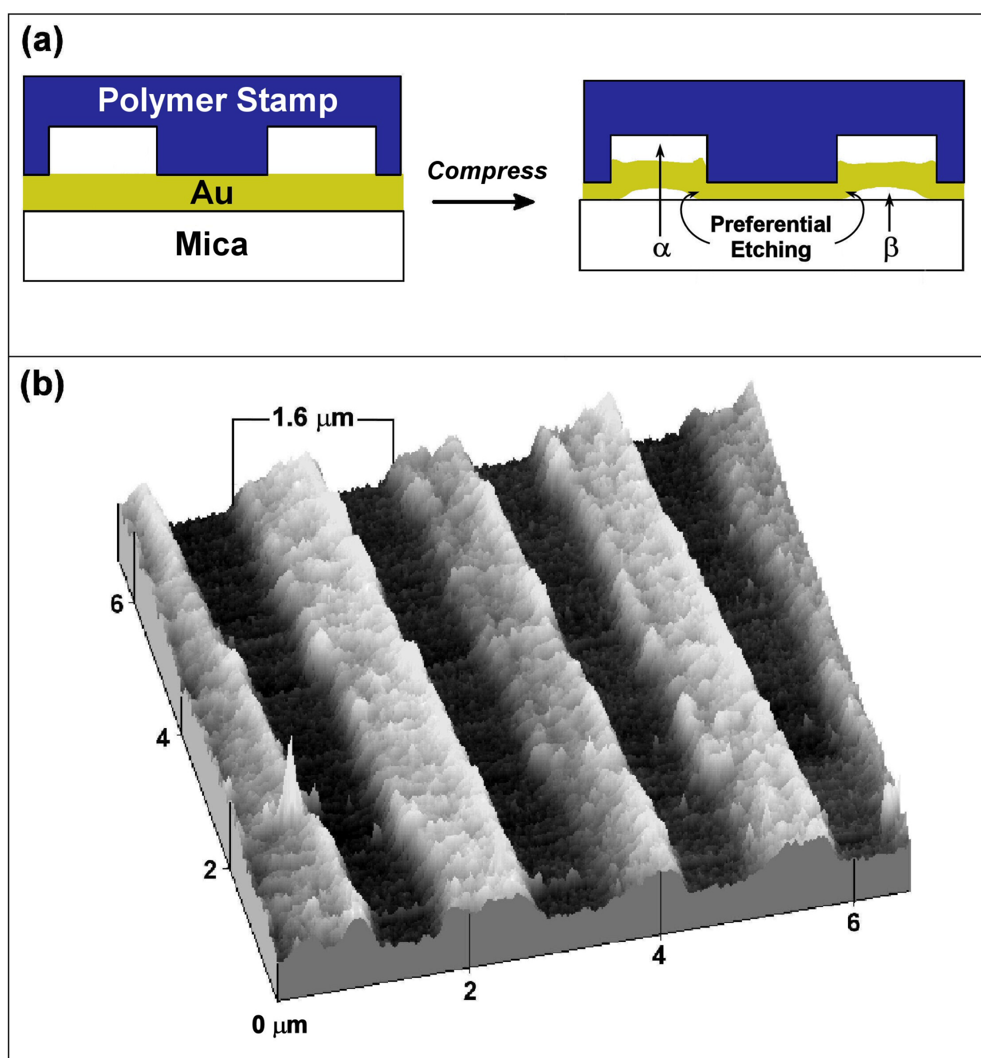

Figure 4.2 (a) Schematic of the plastic deformation that occurs when the Au film is compressed by the stamp. Thinning of the Au film occurs under the ridges, causing it to buckle and delaminate under the recesses from the support ultimately forcing the Au into the recesses of the stamp. (b) An AFM image of a 70 nm Au film on a PC stamp after compression using a typical load of 144 ± 1.8 N (corresponding to a mean pressure of ca. 69 MPa acting at the stamp-substrate sandwich interface) applied for 12 h and without etching. This shows that the initial 70 nm thick Au film has been thinned and raised into the stamp recesses after STOMP processing.

4.3 Results and Discussion

4.3.1 The General Patterning Process

In the STOMP method (Figure 4.1), nanostructures are formed by compressing a polymer stamp against a thin metal film (such as Au) deposited on a rigid support (such as mica, glass or Si) followed by chemically etching the film while under compression. After rinsing, the polymer stamp and support are separated, yielding structures of the initial film material wherein the resulting organization is dictated by the combination of the initial relief structure of the stamp, the interfacial chemistry (i.e., surface energies), and the overall compressibility of the stamp/film/substrate contacts. Using the STOMP process, structures ranging from microscale to the nanoscale are formed and are typically found either on the supporting substrate or within the space defined by the stamp recesses, and/or on the protruding features of the polymer stamp. Subsequent transfer of nanostructures from one surface to another can be readily achieved and enables the construction of more complicated architectures such as 3D superlattices. There are several architectures that can be fabricated by STOMP, and these can be described in three main classes: (1) embedded metal structures, (2) binary structures, and (3) multilayered structures. The structures formed are dependent upon the initial morphology of the stamp used, the pressure with which the stamp and substrate are compressed, and the length of time the samples are etched. In the work presented here, we employed two general types of stamps, those with saw-tooth structures and those with flat planar, ridged structures, consisting of raised lines, cylinders or crosshatched lines. Examples of the types of structures that can be fabricated using these stamps are described, as well as the impact of processing on the resulting structures.

4.3.2 Patterning with Planar Stamps

When polymer stamps with flat rectangular profiles such as those found on a compact disc (CD) are compressed against a 70 nm thick Au film on rigid supports such as mica (Figure 4.2), the Au structures produced are embedded in the stamp recesses after complete etching. Compression of the stamp against the Au film induces buckling, forcing the Au film to deform and to be thinned and displaced from under the ridges of the stamp up into the recesses (Figure 4.2b), delaminating from the substrate under these regions. This deformation and delamination of the film yields two channels (α and β). Such lifting of a 'nonbonded' metal film under loading can occur when the layer thickness is less than the contact width.[62-64]

Table 4.1 Surface Energies of the Polymers and Substrates Employed in this Work

Material	γ (mN/m)
Gold	1145 (50°C)[71]
Mica	144 (22°C)[72]
Polystyrene (PS)	40.7 (20°C)[73]
Polycarbonate (PC)	42.9 (20°C)[73]
Octadecyltriethoxy silane (OTE)	22[74], 31[75] (25°C)

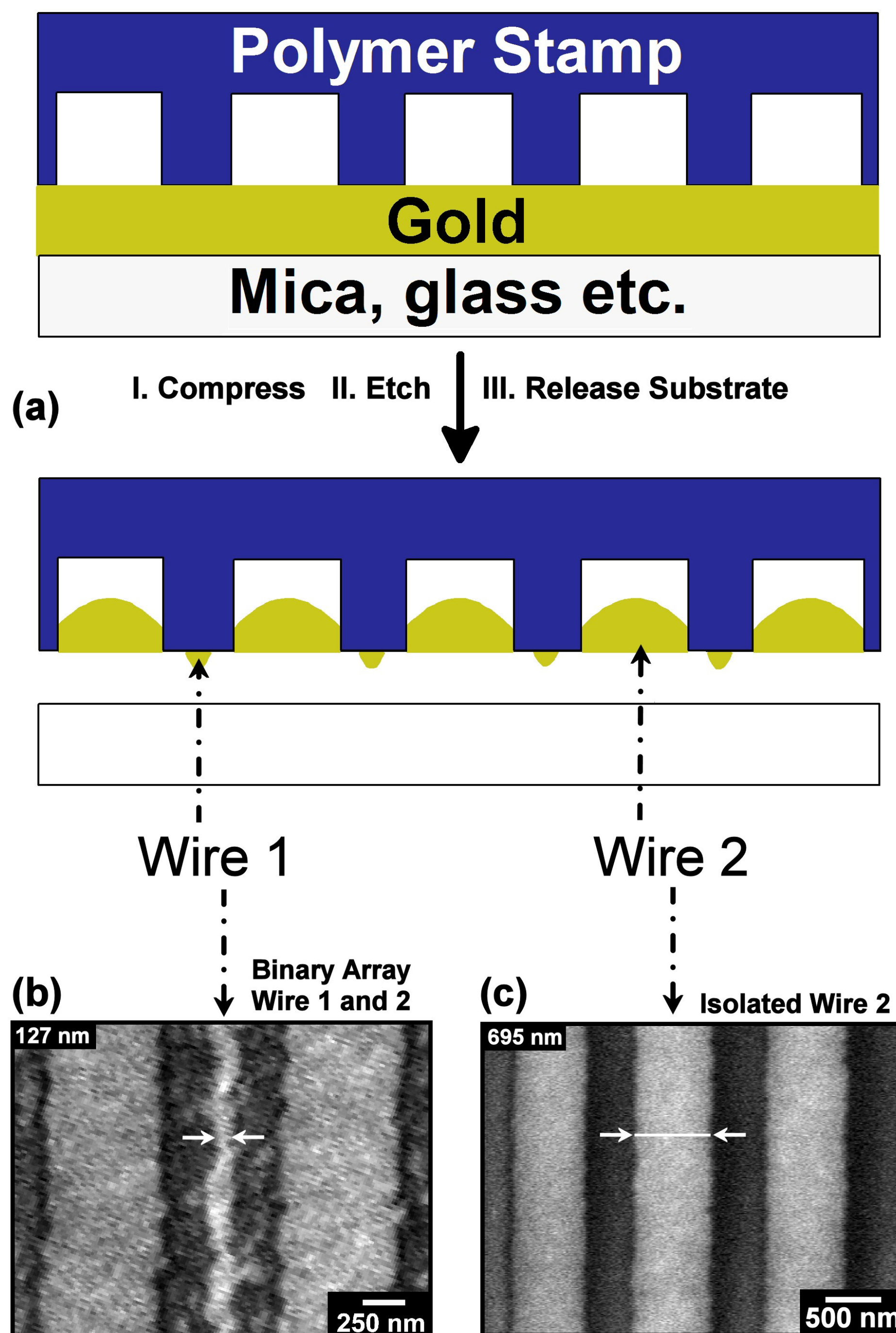

Figure 4.3 (a) Schematic illustrating the placement of the primary structures formed with a polymer stamp possessing a rectangular profile. *Wire 1* resides on the raised stamp feature while *wire 2* is inlaid between the raised polymer stamp features. (b) SEM image of a binary gold wire array. Wires reside on the raised (~ 127 nm, *wire 1*) and within the recessed (~ 750 nm, *wire 2*) regions of a rectangular polycarbonate stamp. The binary wire array is found at the center of the stamp - Au film contact where etching has not completely removed the Au film from under the stamp ridges. (c) SEM image of isolated Au wires (~ 695 nm) embedded in the recesses of a polycarbonate stamp (*wire 2*) following complete etching. The embedded wires (*wire 2)* are continuous over the patterned area of ~ 1 mm^2 and possess a maximum width variation of ~11% across the surface.

The two channels (α and β) formed during compression can be exploited to introduce a preferential etch in one channel (β) over the other (α), based on the solid - liquid interfacial energies of the materials forming the two channels (Table 4.1).[65,66] Under typical processing conditions, the α channel is hydrophobic, as it is defined by the polymer - Au interface, while the β channel offers a more hydrophilic conduit due to the substrate (e.g., mica, glass or an oxidized silicon wafer). Consequently, during etching, the diffusion of the aqueous phase enchant through the α channel is restricted relative to the β channel. This provides a mass transport advantage within the β channel for selective chemical etching below the raised Au, most likely initiating at the pinched strained interface of the Au/mica junction. The phenomenology of arrested or enhanced fluid flow through micro channels[40,67,68] has been extensively investigated and exploited in micrototal analysis systems[69] and MIMIC replication techniques.[2,33,38-41] We have tested this argument of restricted flow and anisotropic etching in our patterning process by conducting experiments in which Au films were deposited on octadecyltriethoxysilane (OTE) coated silicon or glass substrates. With these surface modifications, both the α and β channels are rendered hydrophobic. Processing under these conditions, etching was found to be severely impeded, with only the outermost contact periphery between the stamp and Au surface showing any well-formed structures.

Thus under typical STOMP conditions with a hydrophilic substrate, the Au underneath the ridges of the polymer stamp are etched away faster as the continual compression induces thinning and strain of the delaminating film leaving most of the Au only within the recessed stamp regions. Once all of the Au under the stamp ridges has been etched away, embedded Au wires remain within the stamp recesses (Figure 4.3c,

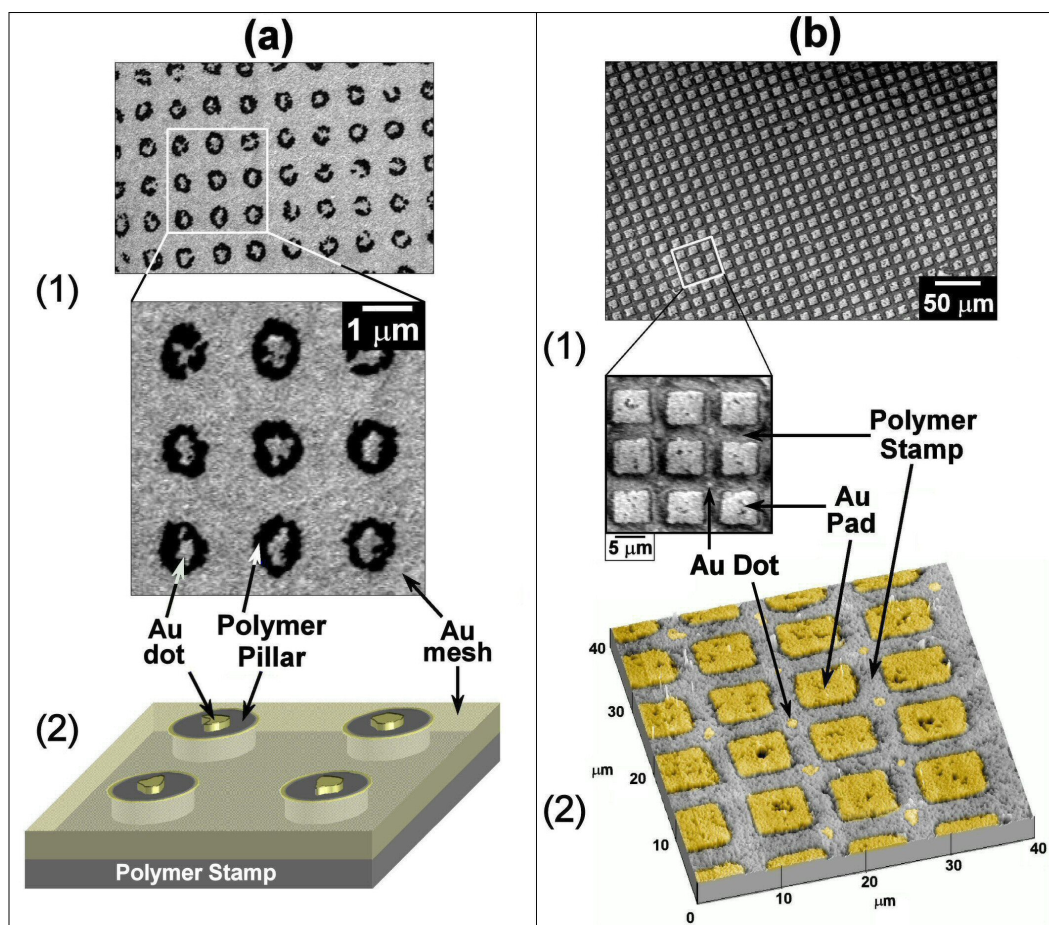

Figure 4.4 Patterns formed using polymer stamps with (a) cylindrical pillars and (b) square cross-hatches (a1) SEM images of a gold structure array consisting of 100 nm thick Au film encompassing pillars of a PS stamp. The dark, ~1 μm (2 μm pitch) circular features correspond to the upright polymer pillars within the Au film. (a2) When etching is stopped prior to completion of part a, Au "dots" are formed and rest on top of the polystyrene pillars. The nonuniform Au dot structure is attributed to the defects in the defining stamp topology yielding nonsymmetric etching. (b1) SEM images of 6 μm square (9 μm pitch) Au pads (100 nm thick Au) embedded within a polystyrene stamp matrix. An AFM image of the embedded Au pads shows a nearly coplanar arrangement (9 nm RMS roughness) with the polystyrene matrix (b2). Au dots are found where the polymer edges intersect, when etching is incomplete (close-up, b1).

w*ire* 2). Here we show Au wires embedded in the grating structure of a polycarbonate compact disk. The grating structure of the CD used here had ~ 200 nm deep by ~ 500 nm wide recesses and ~ 1000 nm wide ridges. These recessed Au structures formed using this STOMP method are found by AFM to be nearly coplanar (± 10 nm) with the polymer stamp ridges. The width of the final embedded gold wires are 695 nm. The lateral dimension of wire 2 is larger than the recess width because the edges of the PC stamp

ridges are actually deformed inward by the forced compression of the Au into the recesses. This makes the outer edges of the recesses wider, resulting in a slight overhang of Au over the ridges following etching. The dimensions of the wires across the entire area of the printed structure are found to be uniform to within ± 11% of this size. Almost no variation of final feature size as a function of compressive load is observed, as the stamp ridges are flat and broad.

Using the same type of stamp but changing the duration of etching allows for the formation of binary structures, which consist of Au wires embedded *within* the recesses as well as resting *on top* of the stamp ridges. This occurs if the etching process is halted prior to the complete etching of Au from underneath the stamp ridges. Here we illustrate (Figure 4.3b) the simultaneous production of binary nanowire arrays, wherein ~127 nm wires are found on the raised features of the stamp (wire 1) and ~750 nm wires (*wire* 2) are found in the recessed features of the rectangular polymer stamp.

The same general principles of structure formation (i.e., Au is compressed into the recesses of the stamp, and etching occurs preferentially under the stamp ridges first) apply for other stamp geometries that also possess flat ridges with square sidewalls. For example, when a stamp with cylindrical posts is employed, complete etching forms a Au film with interstitial polymer pillars. Incomplete etching results in the formation of nanodots centered on top of the polymer pillars, and the rest of the Au film is in the recessed portions of the polymer stamp (Figure 4.4a). The observed formation of these types of structures further supports the mechanism mentioned above, that Au etching is initiated at the strained portions of the film while under compression, prompting accelerated etching along the periphery of the stamp ridge contact where the tensile

stresses are at a maximum.[61] When a crosshatched stamp with well separated square recesses is used, embedded square Au pads are formed with complete etching. When incomplete etching is carried out, Au dots are observed in the center of the intersections of the stamp ridges as well as the square pads in the recesses (Figure 4.4b).

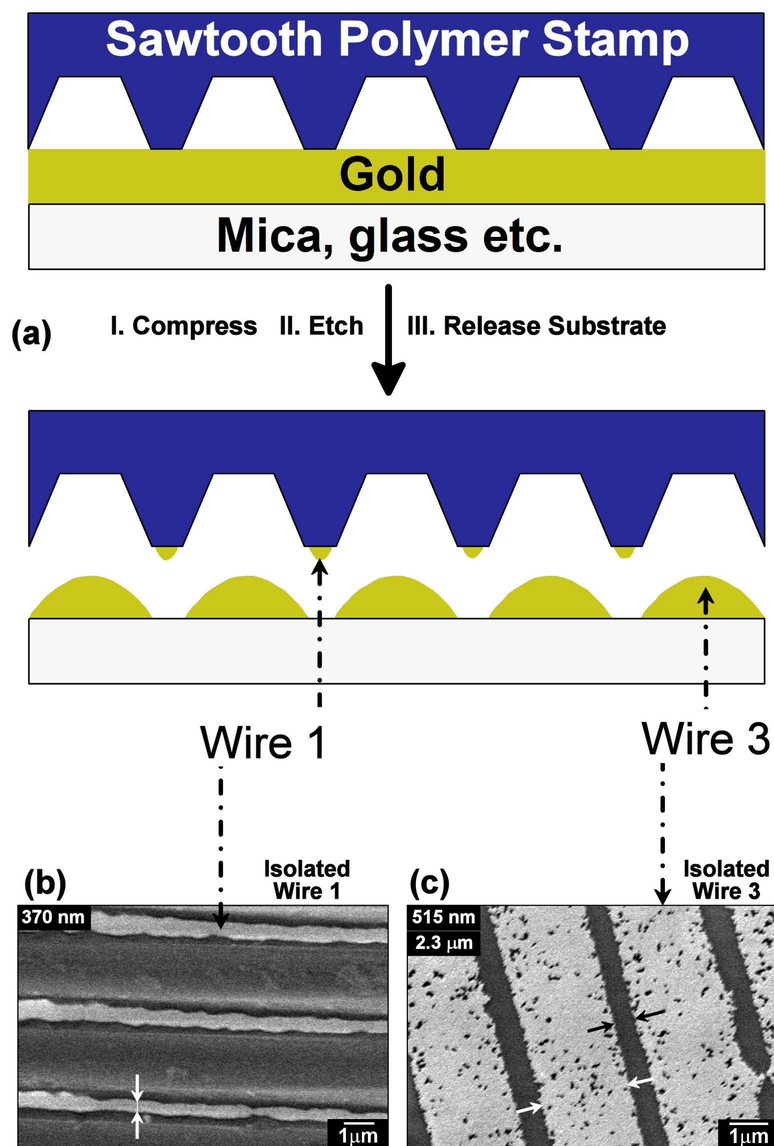

Figure 4.5 (a) Schematic illustrating the STOMP process using a polymer stamp possessing a saw-tooth profile. Upon separation of the stamp from the surface, two types of structures are formed (*wires 1 and 3*). *Wire 1* resides on the raised stamp feature while *wire 3* remains on the substrate. (b) SEM image of Au wires (*wire 1;* 370 - 600 nm) resting on the ridges of a saw-tooth polystyrene stamp with a 3 μm pitch after STOMP processing and (c) *wire 3* complements remaining on the mica substrate. Etch pits are typically present in *wire 3* as etching occurs through the channels formed by the Au/stamp interface.

4.3.3 Patterning with Saw-Tooth Stamp Structures

Switching to stamps with a saw-tooth structure offers an additional means of controlling the structures that can be fabricated. The saw-tooth stamp ridges are parabolic in shape with sloped sidewalls. To investigate the patterning of Au structures using a saw-tooth stamp, we fabricated a polystyrene stamp with 1.3 micron high ridges (3 micrometer pitch) with a radius of curvature of 500 nm. When the curved edges of the stamp are compressed against the Au film under the same load conditions used for patterning with flat ridged stamps, the increased load per unit contact area for the saw-tooth stamps makes the contact pressure greater than the yield stress of the polymer, which partially flattens out the polymer ridges and protects the Au under the raised stamp features from etching. The protected portion of the Au film is subsequently transferred to the ridges of the contacting polymer stamp. The residual Au lying between stamp ridges remains on the substrate surface forming a patterned Au film on the support (Figure 4.5). Thus, with this type of stamp geometry, two distinct patterned products on opposing substrates may be formed simultaneously. The sloped sidewalls act to limit mechanical binding of the metal film effectively eliminating embedded product formation. Moreover, the volume of the channels formed at the Au/polymer interface with the saw - tooth stamps used here are at least 10 times greater than those in the planar cases described, whose channels were relatively small and partially filled with Au when compressed again the metal film. Thus, in this case, etching can more readily occur within the channels formed by the polymer/Au interface, as these channels are sufficiently large to afford transport of the etchant.

Using this stamp geometry, unlike stamps with planar features, the structures formed are dependent on the load applied in STOMP processing. The compressive load could be readily used to tune the dimensions of the structures transferred to the polymer stamp. If the parabolic stamp ridge/Au film contacts were perfectly elastic, one would expect the contact radius to be proportional to the applied load to the one-half power (based on the contact mechanics model of a cylinder against a flat plane) and the resulting feature widths produced would then follow a similar load dependence.[61] However, even though the channels in this stamp are fairly large, a geometric etch rate anisotropy induced by a free volume constraint on the etchant diffusion is often observed,

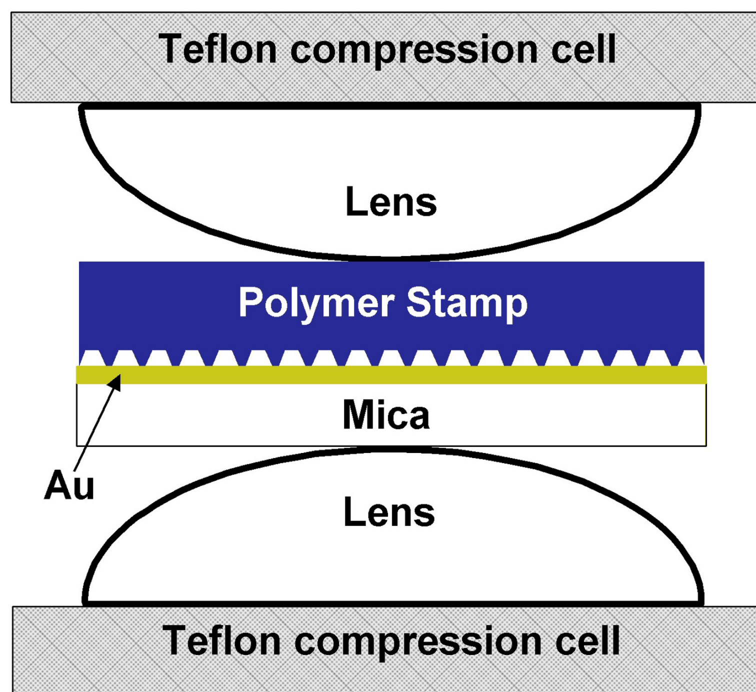

Figure 4.6 Schematic of the nonlinear compression configuration used, which employs two plano-convex lenses as the compression plates. This arrangement provides a well-defined point of contact with a load that varies radially, decreasing outward from the center of contact, permitting a means of investigating load dependence on the dimensions of STOMP fabricated gold structures in a single experiment.

whereby the etching was more complete at the edges of the stamp/Au contact than in the center of the stamp/Au contact. This results in a spatial variation by as much as 25% in the dimensions of the structures formed by this STOMP procedure due to etching alone. Thus under uniform compression, there is an inherent convolution of the applied load and the etching time which determines the size of the resulting structures. In light of this coupling between the etch rate and compressive load on the product feature size, we investigated the influence of pressure on the wire width by compressing the polymer stamp against the Au film between curved press plates made from plano-convex lenses (Figure 4.6). This compression geometry results in a radial pressure gradient at the stamp/Au contact allowing us to probe the load dependence on the structures formed using a single set of experimental conditions.[58,70] Here we again employed a saw-tooth stamp made of polystyrene with the same dimensions as described above. The resulting pressure distribution[61,70] is found to modulate the dimensions of the nanowires produced such that, under the highest pressures (245 MPa), found in the center of the stamp/Au interface contact, wider wires are formed (900 nm wide), while much thinner wires are found (180 nm wide) at the edges of the contact where the pressures are less (43 MPa) (Figure 4.7). Further details on the radial pressure profile for the lens compression cell geometry can be found in Appendix 4.1.

Following patterning, 200 nm PS beads (which have greater affinity for the stamp surface than the Au surface) were added to the fabricated structure and are found to reside within the recesses of the stamp, further illustrating that the Au wires transferred to the stamp appear on the ridges. In the example illustrated here, AFM images of the stamp ridges prior to compression possessed a radius of curvature of ~ 500 nm. Thus,

STOMP provides the ability to both magnify and reduce final structure size via control of the compression load, and it is easy to envision the capability for forming very narrow wires simply by using a molded stamp with sharper ridge features.

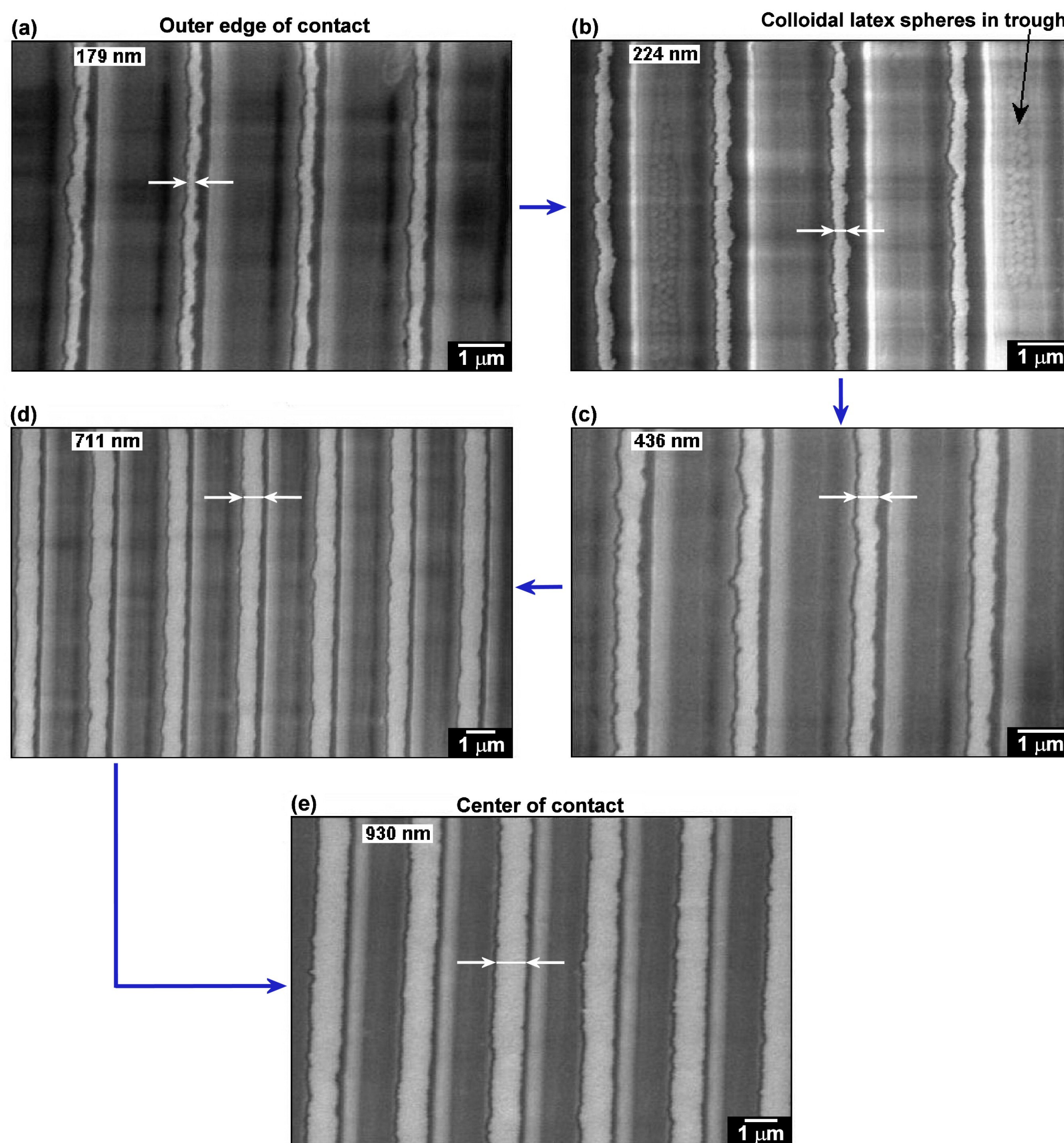

Figure 4.7 SEM images of a polystyrene stamp with gold wires on the ridges made by STOMP processing using opposing convex lenses (as in Figure 4. 6). White arrows highlight the Au feature widths, and their dimensions are given in the upper left-hand corner of each image. Gold wires are arranged along the ridge of the polystyrene saw-tooth grating. The 200 nm colloidal latex particles in part b were solution deposited into the grating troughs to demonstrate the location of the Au wires. When using the opposing convex lenses to exert pressure on the stamp-gold-substrate sandwich, the saw-tooth stamp yields a wire width that varies radially, with (a) the thinnest wires (180 nm) located at the edge of the stamp/film contact where the pressure is lowest and (e) the widest wires (900 nm), located at the center of the contact where the pressure is highest. The separation from the center of contact to the outer edge shown here was ~ 0.5 mm.

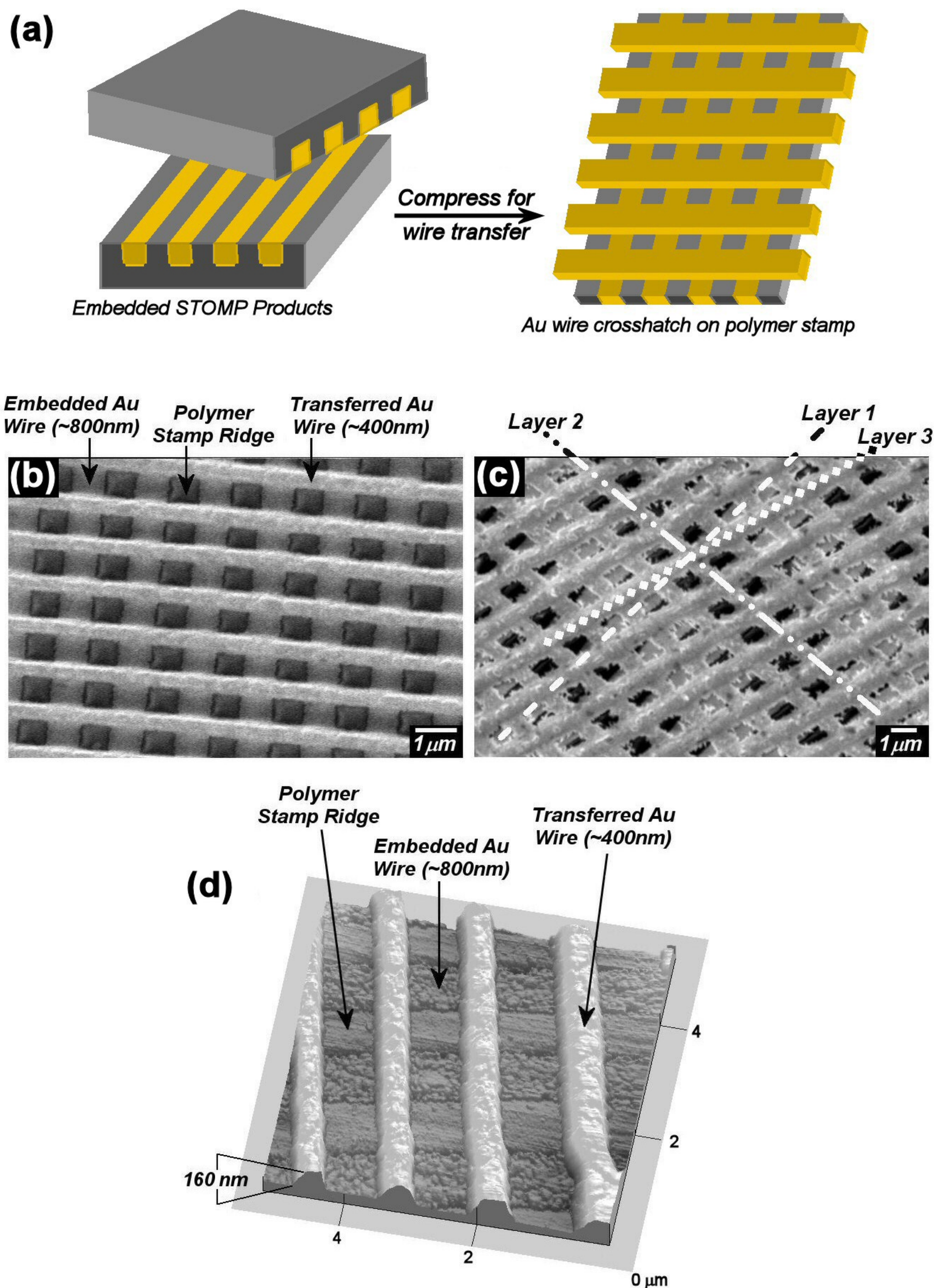

Figure 4.8 (a) Schematic illustrating cold-welding transfer of embedded Au wires. SEM images of (b) an Au wire bilayer with bottom and top wire widths equal to 800 nm and 400 nm, respectively and (c) a trilayer crosshatch of Au wires are shown. Both multilayered architectures are created by bringing two polycarbonate stamps, possessing inlaid nanowire arrays (as in Figure 4. 3c), into compressive contact. Cold welding enables transfer of the embedded wires from one stamp surface to another. (d) AFM image of the bilayer crosshatch in (a) showing the nearly coplanar arrangement of embedded Au wire (~ 800 nm wide) with the raised stamp features (400 nm wide).

4.3.4 Formation of Multilayered Structures

Multilayered 3-D architectures, such as crosshatches, can also be achieved with STOMP by compressing two stamps with embedded wire products together (Figure 4.8). Transfer is predominantly observed to occur from the surface with the thinner wires to the surface with the thicker wires. This transfer process is driven by the higher cohesive energy of the Au-Au contacts (via cold welding) to that of the adhesion of the Au to the polymer stamp, as observed in nanotransfer printing.[23,26,28,29] No reagent, other than water for rinsing, is necessary to create these multilayered structures. The embedded Au wires (*wire* 1) can also be transferred to another substrate such as poly(dimethylsiloxane) where adhesion to the secondary surface exceeds that of the original stamp. In this fashion, structures can be fabricated and then placed onto another surface affording additional design modality.

4.4 Summary

A method for the ***s***ynthesis and ***t***ransfer ***o***f ***m***aterials to and from ***p***olymers (STOMP) has been developed. Features fabricated by STOMP are found to be strongly dependent on the structure of the polymer stamp and its mechanical properties, the compression of the metal film, and the respective interfacial forces between the stamp, film, and substrate. The structures produced are robust, with sufficient mechanical integrity to enable repeated transfer steps to easily build multilayered architectures. Complex nanostructures such as binary nanowire arrays, as well as wires with varying dimensions depending on pressure, have also been demonstrated. The ability of a single

procedure to yield such a wide range of structures by simply changing stamp shape, compression geometry, and/or etching time makes the STOMP process attractive for the benchtop fabrication of many potential devices. This ability to fabricate structures using even simple compact disks as stamps make this a method that can be employed by any researcher without the need for complex fabrication facilities.

Appendix 4.1 – Radial Pressure Distribution for the Stamp-Au Contact

The Hertz contact mechanics model was used to estimate the relative radial pressure distribution, eq. 3.7 in Chapter 3, produced by the glass lens when used to compress the polymer stamp against the gold film.[70] The radius of curvature of the lens was measured to be ~ 37 mm, and the measured contact diameter under compression was 1.32 mm. The respective Poisson ratio (ν) and Young's modulus (E) of the polystyrene stamp and silica lens were (ν_{PS} = 0.33, E_{PS} = 3.3 GPa)[73] and (ν_{silica} = 0.17, E_{silica} = 73 GPa).[76] Here we did not take into account the Au film or plastic effects such as strain hardening. The ridge contact width was assumed to vary radially in line with the macroscopic load distribution (Figure A4.1) as well as with empirical wire width measurements. Although the actual pressures at the ridges are likely to deviate from the calculated values due to asperity flattening and plastic processes within the stamp and Au film, the values do illustrate the relative load differences between the center and edge of the contact, which produced the nearly 4-fold difference in wire dimension.

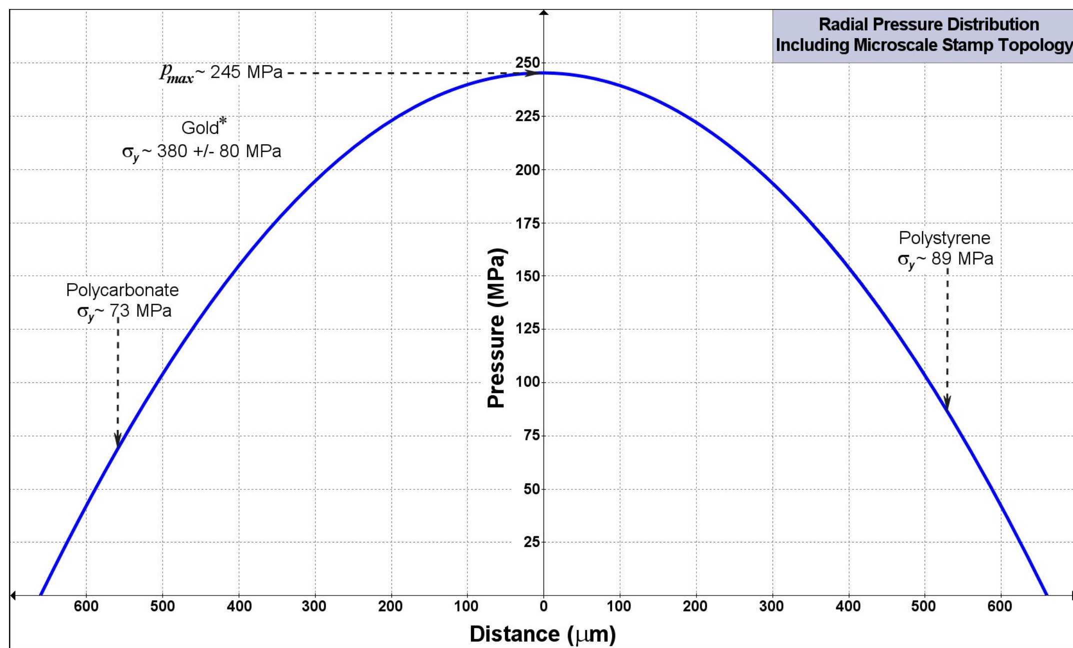

Figure A4.1 (a) Estimated radial pressure distribution (relative to the lens contact center) for the lens compression cell configuration. The maximum Hertz pressure is estimated to be 245 MPa at the center of the contact. For reference, the yield modulus (σ_y) of gold, polystyrene and polycarbonate are noted at their respective positions on the pressure vs. distance plot.

Chapter 4 References

(1) Xia, Y. N.; Rogers, J. A.; Paul, K. E.; Whitesides, G. M. *Chem. Rev.* **1999**, *99*, 1823.

(2) Zhao, X. M.; Xia, Y. N.; Whitesides, G. M. *J. Mater. Chem.* **1997**, *7*, 1069.

(3) Goetting, L. B.; Deng, T.; Whitesides, G. M. *Langmuir* **1999**, *15*, 1182.

(4) Michel, B.; Bernard, A.; Bietsch, A.; Delamarche, E.; Geissler, M.; Juncker, D.; Kind, H.; Renault, J. P.; Rothuizen, H.; Schmid, H.; Schmidt-Winkel, P.; Stutz, R.; Wolf, H. *IBM J. Res. Dev.* **2001**, *45*, 697.

(5) Ng, W. K.; Wu, L.; Moran, P. M. *Appl. Phys. Lett.* **2002**, *81*, 3097.

(6) Zhong, Z. Y.; Gates, B.; Xia, Y. N.; Qin, D. *Langmuir* **2000**, *16*, 10369.

(7) Kumar, A.; Whitesides, G. M. *Appl. Phys. Lett.* **1993**, *63*, 2002.

(8) Schmid, H.; Michel, B. *Macromolecules* **2000**, *33*, 3042.

(9) St. John, P. M.; Craighead, H. G. *Appl. Phys. Lett.* **1996**, *68*, 1022.

(10) Moran, C. E.; Radloff, C.; Halas, N. J. *Adv Mater* **2003**, *15*, 804.

(11) Chou, S. Y.; Krauss, P. R.; Renstrom, P. J. *Appl. Phys. Lett.* **1995**, *67*, 3114.

(12) Chou, S. Y.; Krauss, P. R.; Renstrom, P. J. *J. Vac. Sci. Technol., B* **1996**, *14*, 4129.

(13) Chou, S. Y.; Krauss, P. R.; Renstrom, P. J. *Science* **1996**, *272*, 85.

(14) Krauss, P. R.; Chou, S. Y. *Appl. Phys. Lett.* **1997**, *71*, 3174.

(15) Wu, W.; Cui, B.; Sun, X. Y.; Zhang, W.; Zhuang, L.; Kong, L. S.; Chou, S. Y. *J. Vac. Sci. Technol., B* **1998**, *16*, 3825.

(16) Li, M. T.; Chen, L.; Chou, S. Y. *Appl. Phys. Lett.* **2001**, *78*, 3322.

(17) Austin, M. D.; Chou, S. Y. *Appl. Phys. Lett.* **2002**, *81*, 4431.

(18) Cao, H.; Yu, Z. N.; Wang, J.; Tegenfeldt, J. O.; Austin, R. H.; Chen, E.; Wu, W.; Chou, S. Y. *Appl. Phys. Lett.* **2002**, *81*, 174.

(19) Austin, M.; Chou, S. Y. *J. Vac. Sci. Technol., B* **2002**, *20*, 665.

(20) Kim, Y. S.; Park, J.; Lee, H. H. *Appl. Phys. Lett.* **2002**, *81*, 1011.

(21) Huang, X. D.; Bao, L. R.; Cheng, X.; Guo, L. J.; Pang, S. W.; Yee, A. F. *J. Vac. Sci. Technol., B* **2002**, *20*, 2872.

(22) Chou, S. Y.; Keimel, C.; Gu, J. *Nature* **2002**, *417*, 835.

(23) Kim, C.; Shtein, M.; Forrest, S. R. *Appl. Phys. Lett.* **2002**, *80*, 4051.

(24) Cavallini, M.; Biscarini, F. *Nano Lett.* **2003**, *3*, 1269.

(25) Melosh, N. A.; Boukai, A.; Diana, F.; Gerardot, B.; Badolato, A.; Petroff, P. M.; Heath, J. R. *Science* **2003**, *300*, 112.

(26) Loo, Y. L.; Willett, R. L.; Baldwin, K. W.; Rogers, J. A. *J. Am. Chem. Soc.* **2002**, *124*, 7654.

(27) Matsui, S.; Igaku, Y.; Ishigaki, H.; Fujita, J.; Ishida, M.; Ochiai, Y.; Namatsu, H.; Komuro, M. *J. Vac. Sci. Technol., B* **2003**, *21*, 688.

(28) Loo, Y. L.; Willett, R. L.; Baldwin, K. W.; Rogers, J. A. *Appl. Phys. Lett.* **2002**, *81*, 562.

(29) Schaper, C. D. *Nano Lett.* **2003**, *3*, 1305.

(30) Kim, E.; Xia, Y. N.; Whitesides, G. M. *J. Am. Chem. Soc.* **1996**, *118*, 5722.

(31) Kim, E.; Xia, Y. N.; Whitesides, G. M. *Nature* **1995**, *376*, 581.

(32) Xia, Y. N.; Kim, E.; Whitesides, G. M. *Chem. Mater.* **1996**, *8*, 1558.

(33) Pisignano, D.; Sariconi, E.; Mazzeo, M.; Gigli, G.; Cingolani, R. *Adv Mater* **2002**, *14*, 1565.

(34) Odom, T. W.; Love, J. C.; Wolfe, D. B.; Paul, K. E.; Whitesides, G. M. *Langmuir* **2002**, *18*, 5314.

(35) Paul, K. E.; Prentiss, M.; Whitesides, G. M. *Adv Funct Mater* **2003**, *13*, 259.

(36) Rhee, K. W.; Shirey, L. M.; Isaacson, P. I.; Komegay, C. F.; Dressick, W. J.; Chen, M. S.; Brandow, S. L. *J. Vac. Sci. Technol., B* **2000**, *18*, 3569.

(37) Moran, P. M.; Lange, F. F. *Appl. Phys. Lett.* **1999**, *74*, 1332.

(38) Zhang, F. L.; Nyberg, T.; Inganas, O. *Nano Lett.* **2002**, *2*, 1373.

(39) Kenis, P. J. A.; Ismagilov, R. F.; Takayama, S.; Whitesides, G. M.; Li, S. L.; White, H. S. *Acc. Chem. Res.* **2000**, *33*, 841.

(40) Pisignano, D.; Gigli, G.; Visconti, P.; Zocco, A.; Perrone, A.; Cingolani, R. *J. Vac. Sci. Technol., B* **2002**, *20*, 2248.

(41) Wu, H. K.; Odom, T. W.; Chiu, D. T.; Whitesides, G. M. *J. Am. Chem. Soc.* **2003**, *125*, 554.

(42) Koide, Y.; Such, M. W.; Basu, R.; Evmenenko, G.; Cui, J.; Dutta, P.; Hersam, M. C.; Marks, T. J. *Langmuir* **2003**, *19*, 86.

(43) Zangmeister, R. A. P.; O'Brien, D. F.; Armstrong, N. R. *Adv Funct Mater* **2002**, *12*, 179.

(44) Csucs, G.; Kunzler, T.; Feldman, K.; Robin, F.; Spencer, N. D. *Langmuir* **2003**, *19*, 6104.

(45) Li, H. W.; Muir, B. V. O.; Fichet, G.; Huck, W. T. S. *Langmuir* **2003**, *19*, 1963.

(46) Martin, B. D.; Brandow, S. L.; Dressick, W. J.; Schull, T. L. *Langmuir* **2000**, *16*, 9944.

(47) Kim, C.; Forrest, S. R. *Adv Mater* **2003**, *15*, 541.

(48) Zaumseil, J.; Meitl, M. A.; Hsu, J. W. P.; Acharya, B. R.; Baldwin, K. W.; Loo, Y. L.; Rogers, J. A. *Nano Lett.* **2003**, *3*, 1223.

(49) Li, C. Z.; He, H. X.; Bogozi, A.; Bunch, J. S.; Tao, N. J. *Appl. Phys. Lett.* **2000**, *76*, 1333.

(50) Wind, S. J.; Appenzeller, J.; Martel, R.; Derycke, V.; Avouris, P. *J. Vac. Sci. Technol., B* **2002**, *20*, 2798.

(51) Schider, G.; Krenn, J. R.; Gotschy, W.; Lamprecht, B.; Ditlbacher, H.; Leitner, A.; Aussenegg, F. R. *J. Appl. Phys.* **2001**, *90*, 3825.

(52) Kreiter, M.; Mittler, S.; Knoll, W.; Sambles, J. R. *Phys. Rev. B: Condens. Matter* **2002**, *65*, art. no.

(53) Schmid, H.; Biebuyck, H.; Michel, B.; Martin, O. J. F. *Appl. Phys. Lett.* **1998**, *72*, 2379.

(54) Aoki, K.; Miyazaki, H. T.; Hirayama, H.; Inoshita, K.; Baba, T.; Shinya, N.; Aoyagi, Y. *Appl. Phys. Lett.* **2002**, *81*, 3122.

(55) Yu, H. Z. *Anal. Chem.* **2001**, *73*, 4743.

(56) Yu, H. Z.; Rowe, A. W.; Waugh, D. M. *Anal. Chem.* **2002**, *74*, 5742.

(57) Meijers, P. *Applied Science Research* **1968**, *18*, 353.

(58) Alblas, J. B.; Kuipers, M. *Acta Mechanica* **1970**, *9*, 292

(59) Alblas, J. B.; Kuipers, M. *Acta Mechanica* **1970**, *9*, 1.

(60) Alblas, J. B.; Kuipers, M. *Acta Mechanica* **1970**, *8*, 133.

(61) Johnson, K. L. *Contact Mechanics*; Cambridge University Press: Cambridge, 1987.

(62) Gladwell, G. M. L. *J. Appl. Mech.-Trans. ASME* **1976**, *43*, 263.

(63) Keer, L. M.; Dundurs, J.; Tsai, K. C. *J. Appl. Mech.-Trans. ASME* **1972**, *39*, 1115.

(64) Goudeau, P.; Villain, P.; Tamura, N.; Padmore, H. A. *Appl. Phys. Lett.* **2003**, *83*, 51.

(65) de Gennes, P. G. *Rev. Mod. Phys.* **1985**, *57*, 827.

(66) Myers, D. *Surfaces, Interfaces, and Colloids*; Wiley VCH: New York, 1999.

(67) Kim, D. S.; Lee, K. C.; Kwon, T. H.; Lee, S. S. *J. Micromech. Microeng.* **2002**, *12*, 236.

(68) Zhao, B.; Moore, J. S.; Beebe, D. J. *Anal. Chem.* **2002**, *74*, 4259.

(69) Reyes, D. R.; Iossifidis, D.; Auroux, P. A.; Manz, A. *Anal. Chem.* **2002**, *74*, 2623.

(70) Hertz, H. *J. Reine Angew. Math.* **1881**, *92*, 156.

(71) Vermaak, J. S.; Kuhlmann-Wilsdorf, D. *J. Phys. Chem.* **1968**, *72*, 4150.

(72) Christenson, H. K. *J. Phys. Chem.* **1993**, *97*, 12034.

(73) *Polymer Handbook*; 3rd ed.; Brandrup, J.; Immergut, E. H., Eds.; Wiley-Interscience: New York, 1989.

(74) Kim, S.; Christenson, H. K.; Curry, J. E. *J. Phys. Chem., Part B* **2003**, *107*, 3774.

(75) Ruths, M.; Granick, S. *Langmuir* **1998**, *14*, 1804.

(76) Batteas, J. D.; Quan, X. H.; Weldon, M. K. *Tribol. Lett.* **1999**, *7*, 121.

Chapter 5.

Assembly of Ultra-Thin Polymer-Metal Multilayer Arrays

5.1 Introduction

Since the seminal work of Cory, Keddie and Jones, a significant effort has been put forth to understand the physics of ultra-thin polymer films.[1,2] Numerous studies have expounded upon the thermophysical properties (e.g. glass transition temperature (T_g) and expansivity) of these films, confirming that as film thickness (*h*) approaches scales on the order of the macromolecule's radius of gyration R_g, the film's physical behavior diverges from that of the bulk.[3-11] This dimensional dependence is paramount to existing and future polymer technologies considering the fundamental performance capabilities of these materials (e.g. wetting/dewetting, friction, adhesion and fracture) will continue to be tested as they serve critical functions in coatings, lubricants[12] and in emerging technologies such as nanoimprint lithography[13] and data storage.[14]

In this chapter we illustrate that the unique thermo-physical properties of ultra-thin polymer films provides another element of tailorability that can be used deterministically for the direct pattern transfer of self-aligned micro to nanoscale heterostructures on ceramic surfaces. This soft lithography fabrication technique is the first report to beneficially exploit the diverging physical behavior of confined polymer films for the fabrication of multilayered polymer-metal-polymer (PMP) heterostructures. The technique is termed thermal synthesis and transfer of materials to and from polymers (T-STOMP). While we have previously described a chemical STOMP process,[15] Chapter 4,

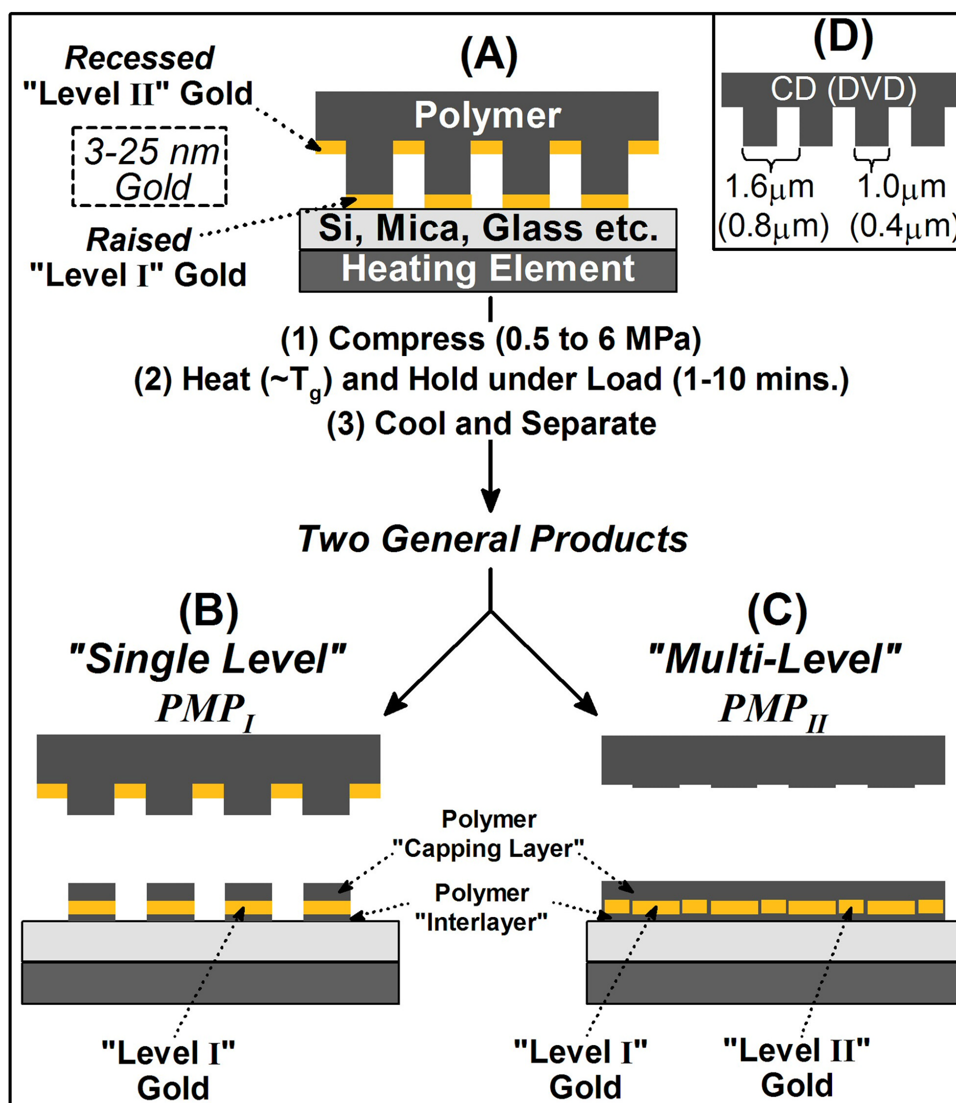

Figure 5.1 Schematic of T-STOMP processing with a bi-level, planar polymer stamp coated with a thin Au film. The coated polymer stamp is brought into compressive contact with a substrate (e.g. mica, glass, silicon, ITO) and subsequently heated (-30°C<T_g <10°C). Depending on the applied load, duration of heating and the dwell temperature, two general tri-layer products can be formed on the substrate. In both instances the tri-layer structure is comprised of a polymer inter-layer, Au film layer and a polymer capping layer. b) Depicts the PMP_I product, where only the Au and polymer from the "raised" portion of the polymer stamp is transferred to the substrate (termed a "single level" transfer). c) Depicts the PMP_{II} product, where Au and polymer from both the "raised" and "recessed" stamp features is transferred to the substrate (termed a "multi-level" transfer). d) Depicts the repeat grating structure of commercial CD and DVD stamps, which possess a recess depth ~ 150 - 200nm. The DVD specifications are noted in parentheses.

the T-STOMP approach detailed here enables direct fabrication of multilayer architectures in a rapid, parallel fashion without employing advanced lithographic tooling or "wet" chemistry for pattern development. Numerous multilayer architectures are available with

T-STOMP, and the potential exists for the fabricated structures and/or substrate to be processed further with conventional and advanced lithographic techniques (e.g. etching, UV-visible photolithography, e-beam and X-ray lithography).

5.2 T-STOMP General Fabrication Technique

T-STOMP processing, Figure 5.1, consists of two steps: (1) a thermoplastic polymer stamp is coated with a thin film material (e.g. gold; typically less than 25 nm) to be transferred to the substrate; and (2) the coated polymer stamp is compressed against a substrate, briefly heated, and subsequently separated from the substrate after cooling. From a single polymer stamp this process enables fabrication of two distinct nanostructured PMP products, Figure 5.1b-c, through transfer of both the thin film and a portion of the outermost surface of the polymer stamp to the substrate. The resulting architecture of the PMP structures depends on both the initial stamp geometry (i.e. relating to the number of topologically unique raised and recessed stamp features), as well as, processing parameters (e.g. applied load, soak temperature and processing time). The polymer stamp depicted in Figure 5.1 possesses a "bi-level" architecture, where each stamp level is defined by the relative stamp feature height. In this manner, the final pattern of the fabricated multilayer arrays can be delineated according to initial stamp geometry, and thereby falls into two general categories: (1) material is transferred *only* from the raised stamp features (termed a "single level" transfer), corresponding to PMP_I products (Figure 5.1b); and (2) material is transferred from *both* the raised and recessed stamp features (termed a "multi-level" transfer), corresponding to PMP_{II} products (Figure 5.1c). In general, structures fabricated with polycarbonate stamps on mica, oxidized

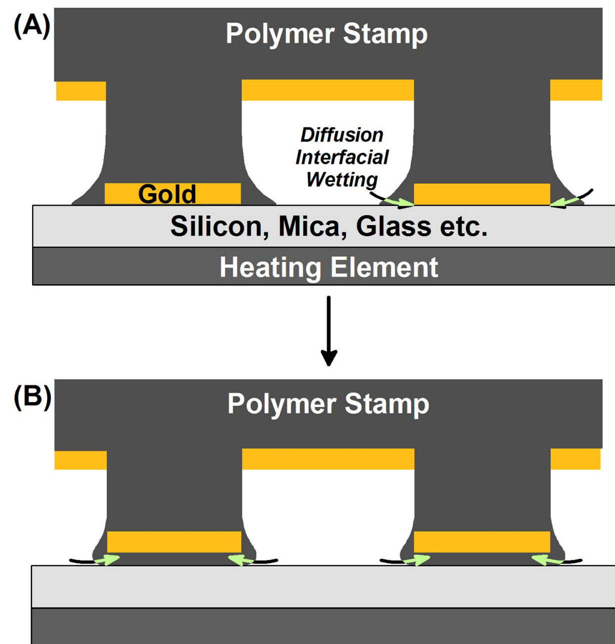

Figure 5.2 Schematic depicting the diffusion path of polymer stamp materials into the gold film-substrate interface during T-STOMP processing. Preferentially wetting of the gold film by an ultra-thin "precursor" polymer film leads to formation of the polymer inter-layer that separates the gold film from the substrate surface in the fabricated multi-layer polymer-metal structure.

silicon wafers and indium tin oxide substrates are comprised of a tri-layer architecture with: (1) an ultra-thin polymer inter-layer that has diffused and intercalated into the metal-substrate interface, (2) a metal film layer (e.g. gold) and (3) a polymer capping layer that coats the metal film.

5.3 What Enables Pattern Transfer?

Generally, PMP multilayer fabrication is enabled by at least two phenomena acting in concert: (1) the synthesis of the polymer inter-layer and (2) the formation of a polymer-polymer "interface" proximate to the capping layer - bulk stamp zone. In a rudimentary way, the spontaneous organization of the inter-layer can be thought of in terms of wetting dynamics where the high surface energy (γ) of the substrate ($\gamma_{mica} \sim 144$ mN/m[16]) and metal film ($\gamma_{gold} \sim 1800$ mN/m at 145°C)[17] causes the spreading of the

polymer macromolecules during heating (Figure 5.2). This ultra-thin polymer inter-layer is an integral component of this transfer process as it acts to bind the metal film to the substrate and, therefore, must be sufficiently robust to withstand the tensile forces exerted during stamp-substrate separation.[18] Secondly, retention of the multilayer structures by the substrate is qualitatively a consequence of cohesive failure at the capping layer – stamp “interface”. In light of the fact that the capping layer and stamp are compositionally the same polymeric material, it is surprising that adhesive failure would preferentially occur at this interface rather than at the substrate - inter-layer interface. There are several possible explanations for this behavior, with the most intriguing centered on the developing description of polymer thin films.[19] One proposal suggests that confined polymer films possess a three layer architecture[20] comprised of “dead”, “bulk” and “liquid-like” layers.[1,2,5,10] Conceptually, this model is attractive and could account for the observed behavior, if it is assumed that layer discreteness yields anisotropic adhesive interactions between the layers. The more pressing question of which specific properties are accountable for this anisotropy is difficult to ascertain at this point, however, a number of effects are likely to be acting cooperatively (e.g. thermal expansion mismatch, dewetting and entanglement variations between each layer).

5.4 Exemplary Examples of T-STOMP Products

5.4.1 Imaging and Characterization

Atomic force microscopy (AFM) images were acquired in contact mode using a Veeco MultiMode SPM and Si_3N_4 cantilevers with nominal tip radii of 10 - 30 nm and nominal spring constants of ~0.1 N/m (Veeco/TM Microscopes, Sunnyvale, CA).

Scanning electron microscopy (SEM) images were obtained with an Amray 1800 (KLA Tencor, San Jose, CA). To minimize charging, the typical SEM imaging conditions used an electron beam current at the sample of ~110 μA with an acceleration voltage of 3.1 kV. Optical micrographs were obtained in reflected light mode with a Unitron MEC 5049 (Unitron Inc., Bohemia, NY) inverted metallurgical microscope adapted with an Olympus digital camera.

5.4.2 Polymer Stamp Preparation

5.4.2.1 CD and DVD Stamps

CD stamps were prepared by scoring and removing the reflective metallic layer. DVD stamps were prepared by scoring the outer edge of the DVD and separating the two laminated discs. The CD and DVD recording media is then removed via sonication in methanol (~15 s) followed by a rinse in ultrapure water and then dried under a stream of nitrogen. The CD and DVD stamps were then cut to the desired size (typically ~ (20 × 20) mm^2 squares).

5.4.2.2 Compression molding Lexan® polycarbonate stamps

Compression molded micro-structured stamps were fabricated from $^{1}/_{16}$" thermoplastic Lexan® sheets (A. L. Hyde Co., Grenloch, NJ). The thermoplastic sheet was cut into (50 x 66) mm^2 rectangles and then placed on a patterned silicon master and compression molded at 185°C for 15 minutes under an applied load of ~ 680 lbs (~ 3018 N) or pressure of (0.92 MPa). The system is then allowed to cool (under load) at a rate of

~ 3 – 4 °C/min. Upon reaching ambient temperature the applied load is slowly removed and the micro-molded Lexan® PC stamp is separated from the patterned silicon wafer and cut to yield 6 stamps approximately (25 × 22) mm^2.

5.4.3 T-STOMP Film Preparation and Patterning Procedure

The prepared CD, DVD and Lexan® polycarbonate stamps were then coated with a thin film of gold via sputter coating (BAL-TEC MED 020, Liechtenstein, Germany). The prepared gold films typically ranged in thickness from 3 nm to 25 nm, with a deposition rate between 0.9 and 1.4 Å/s. The Au target (99.99% purity) was obtained from Techno Trade International (Manchester, NH). Freshly cleaved muscovite mica (Structure Probe Inc., West Chester, PA) was used as the receiving substrate for multi-layer fabrication.

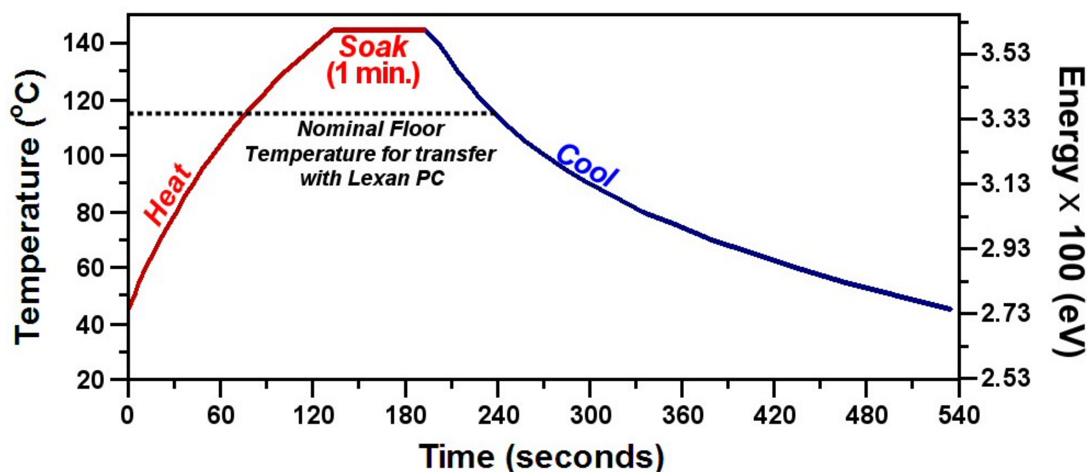

Figure 5.3 Graph of a typical temperature program used during T-STOMP processing. Heating from 45°C to a process (soak) temperature of 145°C typically requires ~130 seconds, with a typical overshoot of 0.6°C and a recovery time of 5 seconds. The temperature is then held constant (+/- 0.2°C) for 1-10 minutes and then cooled to 45°C before separation. The "floor" temperature indicated by the dashed line at 115°C is presently the minimum temperature at which we have observed appreciable PMP transfer to mica. Therefore, the time within heating and cooling segments that are equal to or above this temperature effectively add to the stated processing (soak) times.

The gold coated stamps were then compressed against the mica substrate and subsequently heated in a custom fabricated pneumatic press, fitted with a heating-cooling platen and a programmable temperature controller. A typical two segment temperature program used during T-STOMP processing is given in Figure 5.3. The non-linear, zero-feedback heating ramp represents the maximum heating capacity of the apparatus (~ 46° C/min). Presently, compressive loads corresponding to contact pressures between 0.5 MPa to 6.0 MPa are required to facilitate pattern transfer. We have found the optimal pressure for single level transfer falls on the low end of this range (0.5 – 1.5 MPa) at 145°C, which is roughly common to all the stamps used here. For Lexan® polycarbonate stamps, the preferred soak temperature is within the range of 130°C to 145°C, with the soak times ranging from 1 to 10 minutes. For shorter soak times, the high end of this temperature range (140 - 145°C) yields PMP structures with the highest fidelity. With respect to preferentially fabricating the two T-STOMP products, we have found that for a given soak temperature, longer dwell times and higher pressures favor the "multi-level" PMP_{II} product.

5.4.4 Fabrication of Multi-layer Microstructures

We have tested the T-STOMP technique using a number of polycarbonate (PC) stamps. Figure 5.4 illustrates the products of a "single level" transfer to a mica substrate employing a compression molded polycarbonate stamp (Lexan®, M_w ~ 27 kg/mol, PDI ~ 2.4; nominal unperturbed R_g ~ 8 nm[21,22]). Lexan® stamps possessed a minimum feature width ~ 5 μm and a 500 nm recess depth. Here the PC stamp was coated with a 10 nm Au film and processed at 145°C for 1 minute under an applied pressure of 0.9 MPa.

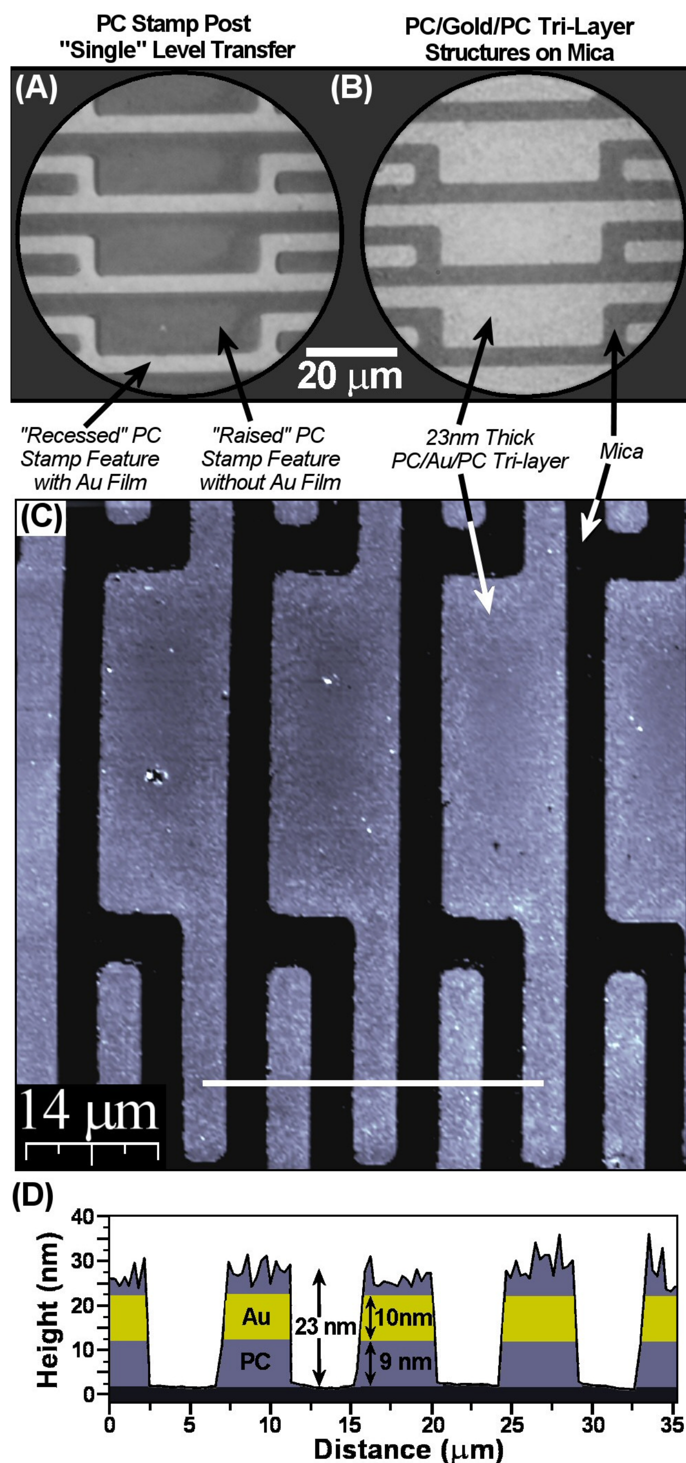

Figure 5.4 PMP_I tri-layer (PC/Au/PC) microstructures fabricated on mica using a compression molded Lexan® PC stamp coated with 10 nm of Au. Fabrication was conducted at 145°C for 1 minute under an applied pressure of 0.85 MPa. a) Optical micrograph of the PC stamp post "single level" transfer. Here the recessed stamp features continue to possess the Au film, while the Au film that resided on the raised stamp features is noticeably absent. b) Optical micrograph of the "single level" PMP_I structures on mica. c-d) AFM topography micrograph of the tri-layer structures possessing a total height of 23 ± 3.4 nm. Etching of the Au layer (which also removes the PC capping layer) reveals an inter-layer thickness of 9 ± 2 nm. From this we estimate the capping layer thickness to be ~ 4 nm.

Due to the wide range of sub-T_g processing temperatures employed in this work, it is worthy to note that the processing times stated throughout this chapter only account for the time spent at the soak temperature, and therefore does not include the time required to heat and cool the sample. Typically it takes ~ 2 minutes for the aluminum heating platen to heat from 45°C to 145°C and approximately 2 minutes to cool from 145°C to 100°C. More details on the pneumatic heating press specifications are provided in Appendix 5.1.

An optical image of the bi-level PC stamp post processing, Figure 5.4a, illustrates that the Au film has been transferred solely from the *raised* stamp feature to the mica substrate. The resulting PMP_I microstructures, as given in the optical (Figure 5.4b) and AFM topography (Figure 5.4c-d) images, demonstrate that uniform pattern transfer for micron scale structures can be achieved with processing times less than 10 minutes. The fabrication of these large microstructures is of both fundamental and practical significance as it offers a novel, accessible method to assess the confined polymers diffusion kinetics during inter-layer formation, which is expected to be the rate limiting step governing the processing throughput of this technique.

Topography measurements (Figure 5.4d) reveal a total height (*h*) of the PMP_I tri-layer to be 23 ± 3.4 nm. Subsequent etching of the Au film layer (*h* = 10 nm, RMS roughness ~ 1.1 nm), which also removes the PC capping layer, exposes the PC inter-layer and reveals an inter-layer thickness of *h* ~ 9 nm ± 2 nm. Taking the difference between these two measurements therefore provides an estimate of the mean capping layer thickness (*h* ~ 4 nm). Notably, the inter-layer and capping layer thicknesses are comparable to the "dead" layer persistence lengths (~ 4 nm - 13 nm) extracted from recent thin film polycarbonate studies.[11] Although this work is continuing, comparison of

preliminary data for the PC and PS systems on mica, indicate that the total thickness of the PMP multi-layer architectures depend on the identity of the polymer and its physical properties (e.g. surface energy). Provided this result stands the test of future inquiry, a tunable multi-layer thickness would be advantageous, especially in applications that look to exploit the nanoscale gap, defined by the thickness of the polymer inter-layer, separating the metal film layer from the substrate.

A general and unexpected observation is the ability to fabricate PMP structures at temperatures well below a polymer's bulk T_g. For example, pattern transfer has been achieved at temperatures as low as 115 °C for polycarbonate, which is ~ 34 °C below its T_g ~149 °C. Similar results are found with Au coated polystyrene stamps (polydisperse M_w ~ 235 kg/mol, Scientific Polymer Products Inc., NY), where pattern transfer to mica occurs at a temperature as low as ~ 80 °C (~20 °C below the bulk T_g of 100 °C). In both instances and common to this technique, the metal film acts as a physical barrier obstructing penetration of the polymer into the Au-mica interface, and thereby requires a considerable amount of polymer diffusion in order to form the inter-layer (Figure 5.2). These results lend credence to the presence of a mobile "liquid" like layer (e.g. a precursor film[23,24]) that spreads even at sub-T_g processing temperatures. Our findings are generally consistent with thin-film phenomenology, and further imply that the unique dynamics of the interfacial polymer chains are accompanied with a discernable change in the polymer's interfacial (adhesive and cohesive) properties. In fact, it has been suggested, from recent modeling of unentangled polycarbonate on a nickel surface, that interfacial polymer segregation could compromise cohesion between the adsorbed ("dead") and adjacent bulk-like macromolecules.[25]

5.4.5 Nanofabrication with CDs and DVDs

5.4.5.1 Single Level Transfer for PMP_I Fabrication

Commercially available polycarbonate compact discs (CDs) and digital video discs (DVDs), possessing a rectangular grating structure (Figure 5.1d) with a recess depth ~ 150 nm – 200 nm also been exploited for use in T-STOMP fabrication. The "single level" transfer products of Figure 5.5 were fabricated on mica with a Au coated (15 nm) CD stamp. Topographic imaging (Figure 5.5a) measures the PMP_I tri-layer height to be ~ 27 nm (excluding the prominent, ~ 85 nm, polymer edge feature). A serrated structure is evident in the SEM image (Figure 5.5b) and corresponds to the ledge in the topography profile (Figure 5.5c). The ledge is thought to arise from incomplete spreading, dewetting and/or fracture of the capping layer from the gold film during fabrication. Assuming that the ledge nominally corresponds to the top of the gold film surface, than the measured thickness of the capping layer is ~ 8 nm and the inferred thickness of the polymer inter-layer is h ~ 4 nm. In this manner the estimated thickness of the inter-layer serves as an *upper limit*, considering that a finite capping layer (perhaps on the order of the Au film RMS roughness ~ 1.2 nm), may indeed exist on the ledge. Presently the disagreement between the inter-layer heights measured for the structures of Figure 5.4 and Figure 5.5 are not understood, but there are several factors that could influence inter-layer thickness including differences in stamp composition (e.g. the presence of glass fillers in the CD stamps and differences in polymer molecular weight). We are currently investigating the effect processing parameters (e.g. temperature, soak time, and pressure) and polymer physical properties (e.g. M_w, surface energy and dopants) have on pattern fidelity, surface morphology and tri-layer thickness.

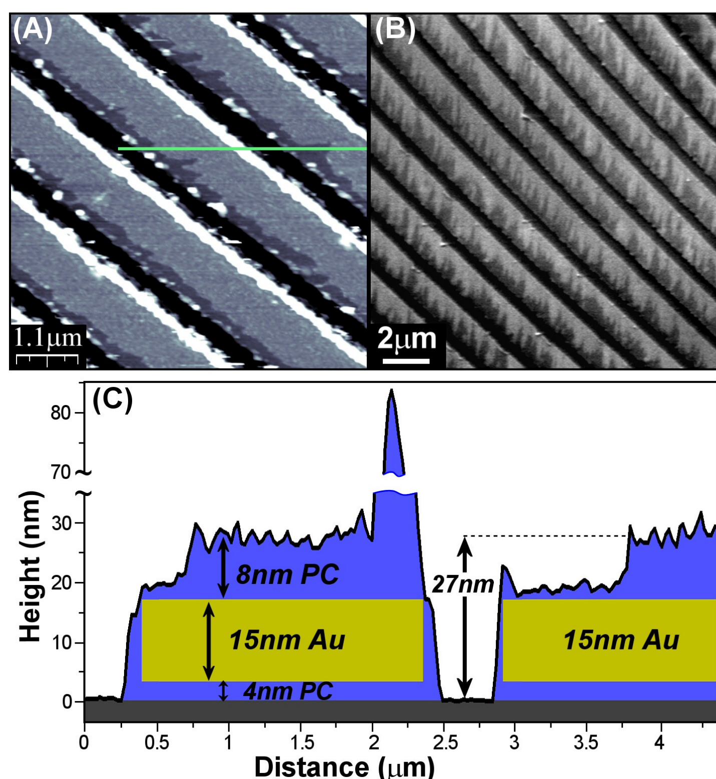

Figure 5.5 PMP_I tri-layer (PC/Au/PC) microstructures fabricated on mica using a bi-level polycarbonate compact disc (CD) stamp coated with 15 nm of Au. Fabrication was conducted at 145°C for 10 minutes under an applied pressure of 1.3 MPa. a) AFM topography and b) SEM micrograph of the multilayered structures on mica. c) The tri-layer structures possess a total height of ~ 27 nm as illustrated in the AFM topography profile. Incomplete spreading, dewetting or fracture of the capping layer leads to the serrated pattern in SEM image and a ledge in the topography. The capping layer thickness is estimated from this ledge to be h ~ 8 nm, which provides an upper limit for the thickness of the of the polymer interlayer (h ~ 4.2 nm) considering that a finite capping layer may exist on "dewetted" areas as depicted in the profile.

With CDs and DVDs, the high fidelity structures are generally limited to small domains (< 2 mm^2) within the patterned region (1 – 2.5 cm^2). Some of the defective structures are noteworthy as they result in PMP_I structures possessing lateral dimensions smaller than the defining stamp features. Incomplete multilayer formation with this characteristic is observed quite frequently and appears as an edge effect were local pressure gradients and/or poor contact parallelism lead to the formation of locally asymmetric stamp-surface contacts. This effect is clearly illustrated in the AFM (Figure 5.6a-c) and SEM (Figure 5.6d) images of the PMP_I structures fabricated on mica with gold

coated CD stamps. Completed wires should possess a line width of ~ 1 μm, such as in Figure 5.6a, corresponding to the raised stamp feature width. As shown in Figure 5.6b-d, edge transfer effects yield wires with a range of widths or equally a varying degree of completion. Currently, the smallest feature widths generated with this edge effect are ~100 nm (Figure 5.6d), corresponding to a width reduction of ~ 10 times relative to the stamp relief dimension. Although this effect is unintentional, it does, however, give insight into the potential resolution T-STOMP can achieve with the appropriate polymer stamp.

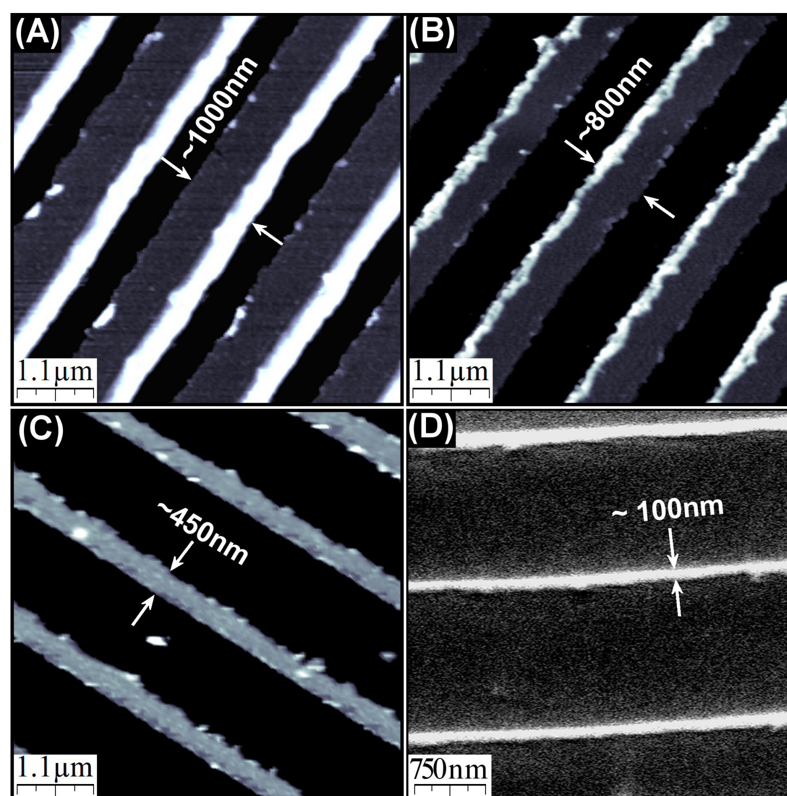

Figure 5.6 Various PMP_I tri-layer (PC/Au/PC) microstructures fabricated on mica using Au coated CD stamps. AFM topography images (a-c) and SEM micrograph (d) illustrate an edge transfer effect where incomplete multi-layer formation can yield structures with a line width that is smaller than full width of the raised CD stamp feature (~ 1 μm). Structures in (a) are consistent with the stamps raised feature width, while the (b-d) features are of varied completeness. The smallest line width of ~100 nm illustrates the resolution capabilities of T-STOMP.

5.4.5.2 Multi-Level Transfer for PMP_{II} Fabrication

The second main multilayered product corresponds to the "multi-level" PMP_{II} array, depicted in Figure 5.1c, where materials are simultaneously transferred from both stamp levels, i.e. from *both* "level I" (raised) and "level II" (recessed). The low and high resolution topography images of Figure 5.7a-b show a mixed array comprised of the "level I" and "level II" structures fabricated on mica with a bi-level DVD stamp (Figure 1d) coated with a 15 nm Au film. Specifically, "single level" PMP_{I} structures, where transfer occurs only from the raised stamp features, are the exclusive product present in the lower right corner of the images. However, PMP_{II} structures, where transfer occurs from both the raised and recessed stamp features, predominate in upper left corner. Comparatively, the "level I" and "level II" structures possess mean heights of 24 nm and 45 nm respectively. This height variation is found to arise from a thickness variation in the capping layer, as the inter-layer thickness (h ~ 5 nm) appears equivalent for both structures. Here the mean capping layer thickness for the "level II" structures ($h_{cap}^{recessed}$~ 25 nm) is appreciably larger than the thickness of the "level I" structure (h_{cap}^{raised}~ 5 nm). This distinct topology is most often found near the boundary of the two product regimes, (e.g. Figure 5.7). However, at the center of the PMP_{II} array (Figure 5.8) the transition between the two surface structures is more subtle and is taken to be representative of the equilibrated PMP_{II} architecture, *vide infra*.

Inspection of the DVD stamps post "single level" transfer (Figure 5.7d) reveals that although the "raised" and "recessed" features are clearly represented, there are noticeable changes attributed to T-STOMP processing. Most evident is the inelastic deformation of the stamp, where the relative feature height is found to decline from ~150

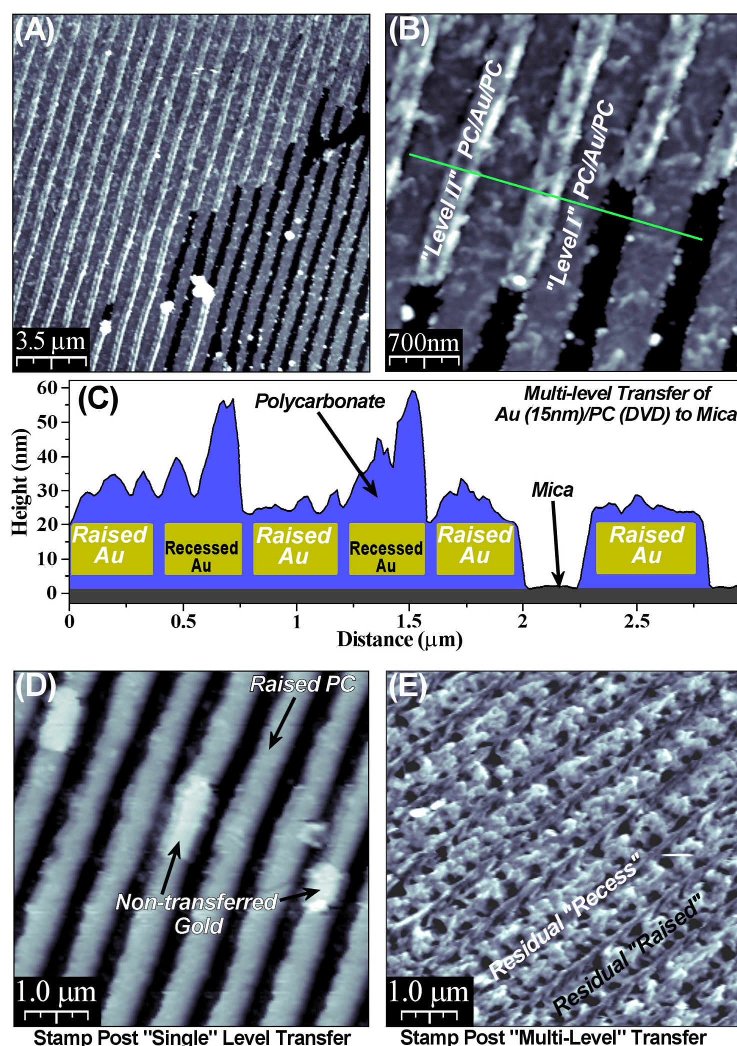

Figure 5.7 AFM topography images of PMP_{II} "multi-level" structures fabricated on mica using a DVD stamp coated with 15 nm of Au. Fabrication was conducted at 140°C for 2 minutes under an apparent applied pressure of ~ 3 MPa. (a-b) Low and high resolution topography images of the tri-layer structures transferred from the "raised" and "recessed" stamp features (as labeled in Fig. 7b). c) AFM profile of the PMP_{II} structures where the "raised" and "recessed" structures possess a mean height of ~ 23 and 45 nm respectively. An inter-layer thickness h ~ 5 nm was measured for both the "raised" and "recessed" tri-layer structures. The capping layer thickness is noticeably larger for the "recessed" structures ($h_{cap}^{recessed}$ ~ 25 nm) than the "raised" structures (h_{cap}^{raised} ~ 4 nm ~ RMS roughness). d) DVD stamp post "single" level transfer with the "raised" and "recessed" features clearly represented. A decrease in the "raised" feature height from ~150 nm to ~ 90 nm is observed. Portions of the Au film that have not been transferred to mica and are retained by raised stamp features are also noted. e) DVD stamp post "multi-level" transfer. The stamp is devoid of its initial grating structure and is nearly planarized with an RMS roughness of 13 nm.

nm to ~ 90 nm. Also readily observed in this topography image are portions of the Au film that were not transferred to the substrate (Figure 5.7d). In contrast, AFM imaging of the DVD stamp post "multi-level" transfer (Figure 5.7e) reveals a topology that is

markedly different than its "single level" counterpart. Multi-level transfer results in a stamp that is essentially devoid of its initial grating structure and is nearly planarized, with an RMS roughness of only ~ 13 nm. Strikingly, a complex "residual" morphology is observed on the stamp post transfer, which gives access to initial stamp feature position, and may also provide information about the processes active during "multi-level" transfer. The details of the plastic yield mechanics and rheology associated with PMP_{II} structure fabrication are critical to the advancement of this technique and require future investigation.

The plane projection of stamp levels to the substrate is one of the most attractive aspects of the PMP_{II} arrays, as it enables generation of the small gap that separates the "level I" and "level II" structures. Previous work by Rogers et al. also illustrated the utility of a compliant polymer stamps step-edge (phase edge) by beneficially employing it in near-field phase shift lithography.[26] In the presented application, the fabricated multi-level heterostructures possess a "level I" and "level II" separation distance comparable to the former work. SEM imaging within the center region of a PMP_{II} array reveals a separation of a ~100 nm (Figure 5.8a). Sample charging during image acquisition precludes a more detailed examination of this interface with SEM. From the AFM images, Figure 5.8b, the estimated structure gap of ~ 65 nm is consistent with the nominal SEM measurements. As previously mentioned, the topology of PMP_{II} structures vary from the center (Figure 5.8) to the periphery (Figure 5.7). At the center, AFM imaging shows an array with a prominent polymer edge feature that is similar to that found in the PMP_{I} arrays of Figures 5.5 and 5.6. In general, these large structures are more frequently observed in the products from DVD and CD stamps, while less frequently with Lexan®

stamps. As noted above, the root of this effect has yet to be explored, but may be attributed in part, to the recording media's composition (e.g. glass fillers).

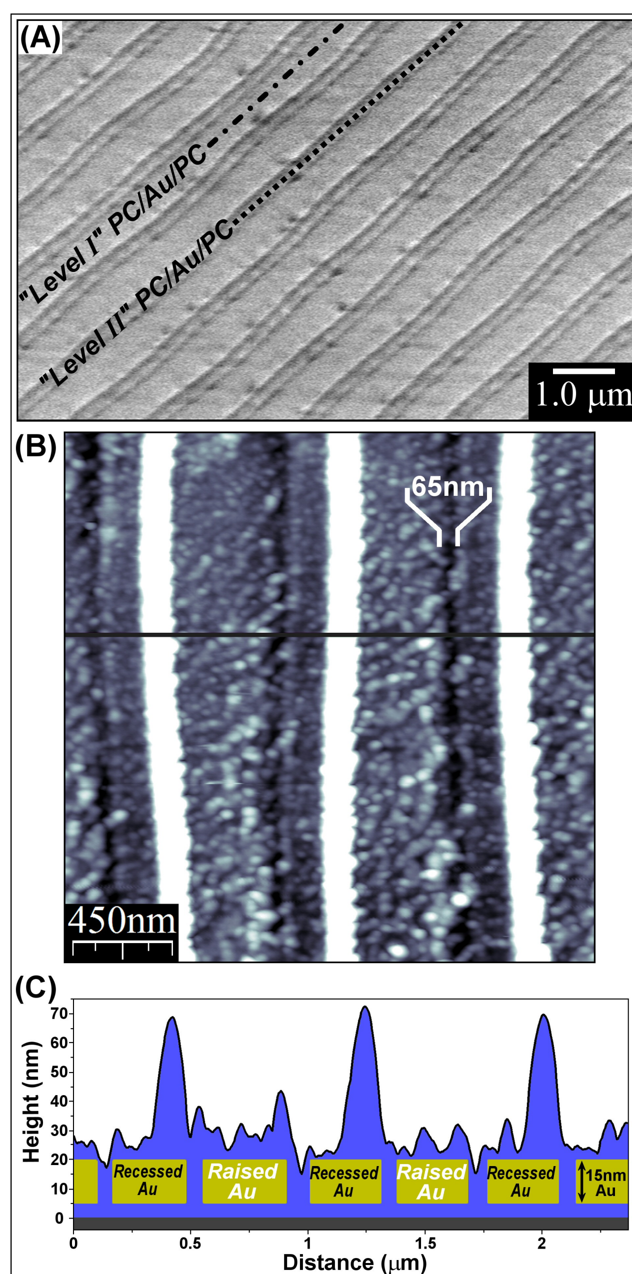

Figure 5.8 Images at the center of a PMP_{II} array fabricated on mica using a PC stamp (DVD) coated with 15 nm of Au. a) SEM imaging estimates a "level I"-"level II" separation distance of ~ 100 nm. b) From an AFM topographic image the gap is found to be ~ 65 nm. The RMS roughness is statistically equivalent to the peripheral structures given in Figure 5.7. c) Topography profile of the tri-layer illustrating the relative position of the "level I"-"level II" structures.

5.5 Summary and Conclusion

In conclusion, a new nanolithography technique (T-STOMP) is presented enabling a multiplicity of multilayer, polymer-metal-polymer (PMP) heterostructures to be fabricated on ceramic substrates with inexpensive, metal coated thermoplastic stamps. T-STOMP processing is straightforward to implement and is capable of fabricating ultra-thin, PMP architectures spanning the micron to nanoscale regime. Dense arrays with sub-100 nm feature spacing and nanoscale (< 11 nm) substrate metal-film gaps (defined by a polymer inter-layer) were demonstrated. The polymer coated nanowires are insulated from other nanowires and the surface. Special tooling is not required with this technique nor does it require advanced material formulations, as readily available CD, DVD and Lexan® polycarbonate stamps have been used to demonstrate this technique. Optimization of T-STOMPs procedure and material combinations is needed in order to progress towards more uniform, low defect density arrays required for device applications. Several applications can be envisioned for this technique for the fabrication of novel sensing arrays, as well as potentially a single step fabrication approach for OLED device components. The integration of optical dyes into the thermoplastic stamp for the transfer and generation of molecularly doped[27] PMP structures are currently underway.

Appendix 5.1 – Pneumatic Press Specifications

Specifications for the custom pneumatic press used for the thermal synthesis and transfer of materials to and from polymers (T-STOMP) are provided in Table 5.1. A picture of the press is also provided in Figure A5.1.

Table A5.1 Specifications for Heated Pneumatic Press

Property	**Value**
Maximum compressive load	8,200 N
Wafer diameter capacity	100 mm
PID controlled programmable temperature segments	16
Heating Platen Power	1000 watts
Maximum operating temperature *(20 minutes)*	185°C
Maximum Heating Rate with Coolant flow >10 GPH	46°C/min
Soak temperature overshoot during initial ramp	0.4 - 1.2°C
Critical cooling rate with coolant flow >10 GPH (21°C Water Coolant) *Platen Cooled from 145°C to 90°C; 90°C is a typical bulk polymer* T_g	28°C/min
Strike Plate Insulating Capacity (*Contacting 100°C Platen*)	0.7°C/min
Strike Plate Temp. Rise during Stamp Fabrication *Processing Parameters: 185°C for 8 mins.,* $^{1}/_{16}$*" thick PC stamp; ¼" Al Chuck*	50°C

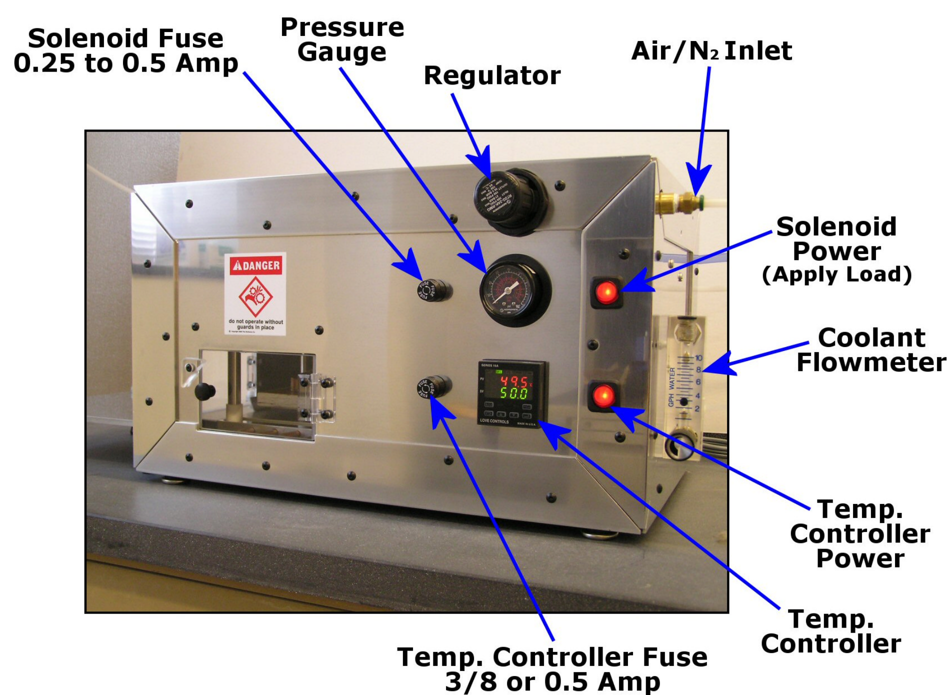

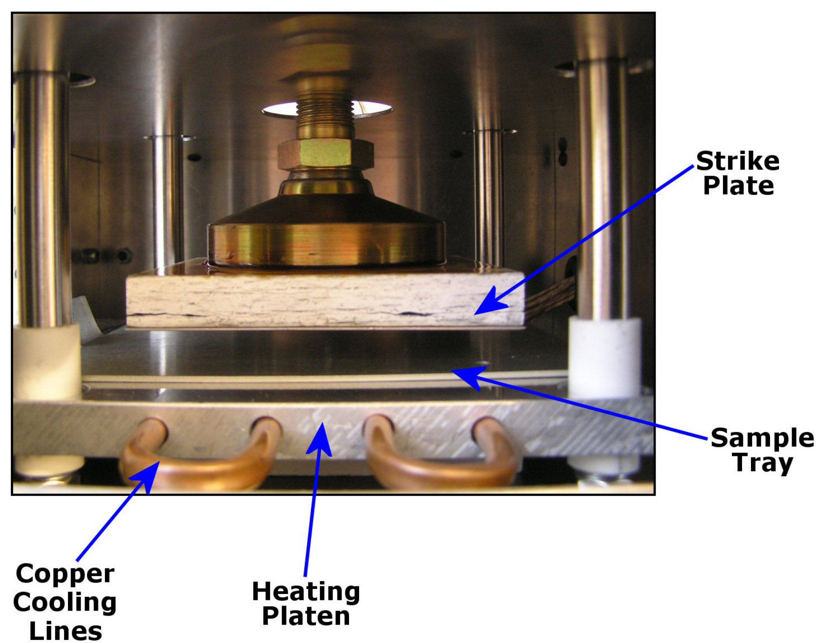

Figure A5.1 The custom pneumatic press used for the thermal synthesis and transfer of materials to and from polymers (T-STOMP).

Chapter 5 References

(1) Keddie, J. L.; Jones, R. A. L.; Cory, R. A. *Europhys. Lett.* **1994**, *27*, 59.

(2) Keddie, J. L.; Jones, R. A. L.; Cory, R. A. *Faraday Discuss.* **1994**, 219.

(3) Forrest, J. A.; Dalnoki-Veress, K.; Stevens, J. R.; Dutcher, J. R. *Phys. Rev. Lett.* **1996**, *77*, 2002–2005.

(4) Tseng, K. C.; Turro, N. J.; Durning, C. J. *Phys. Rev. E: Stat. Phys., Plasmas, Fluids, Relat. Interdiscip. Top.* **2000**, *61*, 1800.

(5) Fukao, K.; Miyamoto, Y. *Phys. Rev. E: Stat. Phys., Plasmas, Fluids, Relat. Interdiscip. Top.* **2000**, *61*, 1743.

(6) Forrest, J. A.; Dalnoki-Veressb, K. *Adv. Colloid Interface Sci.* **2001**, *94*, 167.

(7) Ellison, C. J.; Torkelson, J. M. *Nat. Mater.* **2003**, *2*, 695.

(8) Sharp, J. S.; Teichroeb, J. H.; Forrest, J. A. *Eur. Phys. J. E* **2004**, *15*, 473.

(9) Soles, C. L.; Douglas, J. F.; Jones, R. L.; Wu, W. *Macromolecules* **2004**, *37*, 2901.

(10) Kawana, S.; Jones, R. A. L. *Phys. Rev. E* **2001**, *63*, 021501.

(11) Soles, C. L.; Douglas, J. F.; Wu, W. L.; Peng, H.; Gidley, D. W. *Macromolecules* **2004**, *37*, 2890.

(12) *Springer Handbook of Nanotechnology*; 1 ed.; Bhushan, B., Ed.; Springer: Berlin, 2004, pp 1222.

(13) Chou, S. Y.; Krauss, P. R.; Renstrom, P. J. *Appl. Phys. Lett.* **1995**, *67*, 3114.

(14) Durig, U.; Cross, G.; Despont, M.; Drechsler, U.; Haberle, W.; Lutwyche, M. I.; Rothuizen, H.; Stutz, R.; Widmer, R.; Vettiger, P.; Binnig, G. K.; King, W. P.; Goodson, K. E. *Tribol. Lett.* **2000**, *9*, 25.

(15) Helt, J. M.; Drain, C. M.; Batteas, J. D. *J. Am. Chem. Soc.* **2004**, *126*, 628.

(16) Christenson, H. K. *J. Phys. Chem.* **1993**, *97*, 12034.

(17) Vermaak, J. S.; Kuhlmann-Wilsdorf, D. *J. Phys. Chem.* **1968**, *72*, 4150.

(18) Burkstrand, J. M. *J. Appl. Phys.* **1981**, *52*, 4795.

(19) *Eur. Phys. J. E* **2002**, *8*, 101.

(20) DeMaggio, G. B.; Frieze, W. E.; Gidley, D. W.; Zhu, M.; Hristov, H. A.; Yee, A. F. *Phys. Rev. Lett.* **1997**, *78*, 1524.

(21) Li, D.; Han, B.; Huo, Q.; Wang, J.; Dong, B. *Macromolecules* **2001**, *34*, 4874.

(22) Maeda, N.; Norisuye, T. *Polymer* **1993**, *34*, 3475.

(23) de Gennes, P. G. *Rev. Mod. Phys.* **1985**, *57*, 827.

(24) Glick, D.; Thiansathaporn, P.; Superfine, R. *Appl. Phys. Lett.* **1997**, *71*, 3513.

(25) Abrams, C. F.; Site, L. D.; Kremer, K. *Physical Review E (Statistical, Nonlinear, and Soft Matter Physics)* **2003**, *67*, 021807.

(26) Rogers, J. A.; Paul, K. E.; Jackman, R. J.; Whitesides, G. M. *Appl. Phys. Lett.* **1997**, *70*, 2658.

(27) Ioannidis, A.; Facci, J. S.; Abkowitz, M. A. *J. Appl. Phys.* **1998**, *84*, 1439.